



**University of Crete
Physics Department**



Photochemical doping of mechanically exfoliated monolayer WS_2

Demeridou Ioanna

Thesis

For the degree of Master of Science

Supervisor: Prof. Costas Fotakis

Co-supervisor: Dr. Emmanuel Stratakis

Heraklion

February 2016

Contents

Acknowledgement.....	5
Abstract	7
I. Introduction.....	9
I.1.1 Introduction to 2D Transition Metal Dichalcogenides (TMDs).....	10
I.1.2 Crystal structure of tungsten disulfide	11
I.1.3 Electronic band structure.....	13
I.1.4 Optical and vibrational properties	16
I.1.5 Spin, orbit and valley interactions.....	19
I.1.6 Excitonic effects	21
I.2 Micro-Raman Spectroscopy and micro-PL Spectroscopy	22
I.2.1 Mechanism of Raman and Rayleigh scattering.....	22
I.2.2 Theory of Raman scattering	25
I.2.3 Raman spectroscopy of WS_2	27
I.2.4 Introduction to photoluminescence (PL).....	31
I.2.5 Micro-Photoluminescence spectroscopy of monolayer WS_2	34
I.2.6 Identification of biexcitons in single-layer WS_2	40
I.3 Chemical doping of monolayer WS_2	44
I.4 Experimental methods	46
I.4.1 Preparation of single-layered and multilayered WS_2 nanosheets by micromechanical exfoliation.....	46
I.4.2 Experimental set up of Raman spectrometer.....	48
I.4.3 Experimental set up of photoluminescence spectrometer	49
I.4.4 Experimental setup for photochemical doping Tungsten disulfide(WS_2) in chlorine (Cl_2) and nitrogen (NH_3) environment.....	51
II. Experimental results and discussion	54
II.1 Sample characterization.....	54
II.2 Photochemical doping of mechanically exfoliated monolayer WS_2 with Cl_2 and NH_3	57
II.3 Results before and after photochemical doping with Cl_2	58
II.4 Results before and after photochemical doping with NH_3	64
II.5 Micro-PL temperature dependence before and after photochemical doping with Cl_2 and NH_3	69

II.6 Identification of biexcitons in monolayer WS_2 after photochemical doping with Cl_2	79
III. Conclusion and future plans	87
References	89

Acknowledgement

Firstly, I would like to express my sincere gratitude to my principal supervisor, Professor Costas Fotakis, for giving me the opportunity to work in the “Ultrafast Laser Micro and Nano-Processing” (ULMNP) laboratory, Savvas Georgiou, of IESL-FORTH.

Furthermore, my special thanks and gratitude to my second supervisor Dr. Emmanuel Stratakis for his guidance and support during this year. I have not only gained a great deal of knowledge, but also he gave me the groundings to be able to deal with the research activities. It was a very rewarding and challenging experience and I am very grateful for his support. His willingness to invest his time so generously has been very much appreciated.

Professor George Kioseoglou has been a great mentor and an excellent advisor. He was always available to discuss my thesis and he gave me precious advises to continue my study. Our discussions and his guidance were valuable during my studies. I would like to express my sincere appreciation and gratitude.

I would also like to express my thanks to Professor Nikos Pelekanos for the concession of the laboratory area in the Microelectronics Research Group (MRG) and the excellent collaboration we had during this year. I would also like to thank Professor Demetrios Anglos for his significant advices, knowledge and time.

The help of my colleagues was crucial and honestly appreciated. Thus, first of all, I would like to express my gratitude to Dr. Savvas Germanis, for working together and having a nice cooperation during the experiments. Also, many thanks to Ioannis Paradisanos, who was always there to answer my questions and for giving me useful guidance on my study (both in the lab and the data analysis). Both of them gave me suggestions, comments and remarks on the project and a valuable help when it was needed. I would also like to thank Yannis Labrakis, Kyraki Savva and Marina Stivaktaki for their help and support.

On a more personal level, I must thank Andreas Lemonis, Kostas Triantopoulos, Elisa Papadopoulou and Christiana Alexandridi for always being present and relieved me from the tough times.

Moreover, a special thanks goes to my parents and brother for encouraging me and always believing in me. Their love and support have been a wonderful motivation for me. I felt their support with all possible ways.

Finally, a great thanks to my friends Christina, Sophia, Maria, Georgia and Charis for their great support through these years.

Abstract

Transition metal dichalcogenides (TMDs) bonded by weak Van der Waals forces between layers, can be mechanically exfoliated to a single layer. These ultrathin materials belong to the family of two dimensional (2D) materials. By reducing the thickness, 2D materials exhibit spectacular optical and charge transport properties. As a result, the exciton-related phenomena, are prominent in TMDs monolayers compared to their bulk counterparts. With tunable bandgaps, 2D TMDs present both fundamental and practical interest. Micro-Raman and micro-Photoluminescence spectroscopy were used to characterize the layered TMD films.

The purpose of this thesis is the study of a new photochemical doping technique. A mechanically exfoliated monolayer tungsten disulfide (WS_2), is radiated by a pulsed UV laser in rich chlorine and nitrogen environment in order to further understand the excitonic properties, with different carrier' densities and as a result, to tune the band gap of the crystal. Both micro-PL and micro-Raman spectra of the doped monolayer WS_2 are affected by this photochemical doping.

These remarkable mechanical and optical properties open up many opportunities in the field of optoelectronics. The manipulation of the electrical and optical properties of two dimensional TMDs, is particularly important for developing optoelectronics devices for chemical and biochemical sensing applications. Finally, there is a wide range of applications for energy storage and high performance electronics.

I. Introduction

Layered compounds involving transition metal dichalcogenides (TMDs) are promising candidates for exploring atomically thin structures [1]. TMDs are the most studied layered compounds that have been isolated in monolayer (1L) form from bulk crystals by mechanical exfoliation [2].

Monolayer structure consists of three atomic layers. All the TMDs have a strong intra-layer metal-chalcogen bond while, the layers are weakly held together by Van der Waals forces. Bulk crystals are semiconductors with indirect band gap. As the number of layers decreases and reaches a monolayer limit, the semiconductor has a direct bandgap at the K and $-K$ points of the Brillouin zone [3].

In this thesis, we present a new photochemical doping technique of monolayer WS_2 . This technique is based on radiation of monolayer crystals presence of carrier gas (dopants) with pulsed laser. If this technique is a success method to investigate the doping in a crystal, we can tune the bandgap of monolayer WS_2 and explore the electronic properties of a photochemical doped semiconductor. It is known that a chemical doped crystal has a large variety of applications, such as high performance electronics based on chemically doped 1L WS_2 , high performance sensors and energy storage.

For this purpose, we will study the photoluminescence and Raman spectra before and after photochemical doping.

I.1.1 Introduction to 2D Transition Metal Dichalcogenides (TMDs)

Dimensionality is one of the most fundamental material's parameters, which defines the atomic structure and the properties to a significant degree of the material. The same chemical element or compound can exhibit different properties in very low dimensions. The isolation and electrical characterization of graphene has led to the exploration of other 2D materials [4]. The most interesting feature about these materials is the change in properties compared with their bulk counterparts. Single layers of transition metal dichalcogenides have attracted notable attention. Despite the similarity in the chemical formula MX_2 , where typically M is a transition metal and X is a chalcogen, different types of single layer TMDs act as insulators to semiconductors and semimetals to metals. There are many layered materials with strong in-plane chemical bonds and weak coupling between layers. The family of layered Van der Waals materials with weak Van der Waals forces between layers, make them suitable for exfoliation [5]. Materials like MoS_2 , WS_2 , $MoSe_2$, WSe_2 have been widely studied for applications. The band gaps of these materials can be tuned by stacking confinement and under the impact of strong electric fields.

In this chapter, we will introduce WS_2 , since it is one of the most common TMDs, it constitutes a high quantum yield two-dimensional (2D) system in monolayer form and can be easily exfoliated from a 3D crystal. Single layer WS_2 , is a semiconductor with direct optical gap at $2.1eV$ and has a huge implication when studying photoluminescence. Chemical and thermal stability makes WS_2 a suitable component for flexible 2D electronics and a basic material for transistors and other electronic and optoelectronic devices. Two-dimensional crystals show different structural, electronic and optical properties from their parent three-dimensional materials. Specifically, in their monolayer form, remarkable changes appear in their electronic band structure, like wide spin-orbit splitting and enhanced photoluminescence. Most of these properties are nonexistent for two-layer stacks of the same 2D crystal. For example, the spin-orbit splitting of a single-layer WS_2 is $0,38eV$ in the valence band, while the bilayer of the same material is an indirect band gap semiconductor without observable spin-orbit splitting.

I.1.2 Crystal structure of tungsten disulfide

The transition metal atoms are sandwiched between two layers of chalcogen atoms. One transition metal atom is coordinated by six chalcogen atoms to form either octahedral or trigonal prismatic polyhedrons. The bulk layered TMD is constituted of strong intralayer covalent M-X bonds and weak interlayer Van der Waals forces [5]. There is a variety of stacking polytypes of bulk Mo and W. The most common three are the 1T, 2H and 3R phases [6] (T: Trigonal, H: Hexagonal, R: Rhombohedral). As we can see in Fig.1, the 1T phase has a tetragonal symmetry with octahedral coordination, the 2H phase has a hexagonal symmetry with trigonal prismatic coordination and 3R phase has a rhombohedral symmetry with trigonal prismatic coordination. The 2H phase is the most stable phase of WS_2 . As the number of layers decreased to one, there is no variety of stacking different layers, just 1H and 1T. The coordination of metal atoms is trigonal prismatic in the 1H phase and octahedral in the 1T phase, as we can see in Fig. 2 (a) and (b). The 1H phase is the most common phase for WS_2 monolayer. The number one (1) indicates the number of layers in a unit cell (ex. 1H has one unit cell). The structure of WS_2 consist of an atomic plane of W, which is sandwiched between the two atomic planes of S in a trigonal prismatic arrangement S-W-S [7]. The layer thickness is $0.6 - 0.7nm$ [8].

Fig.2 (a) and (b) show two kinds of structure of the monolayer of TMDs, trigonal prismatic and octahedral coordination. The trigonal prismatic structure forms AbA stacking with a top view formation which is very similar to honeycomb structure of graphene, while octahedral coordination reveals AbC stacking. In nature, WS_2 forms a stable layered structure, bonded by Van der Waals forces, which are weak enough to peel off, thus monolayer can be isolated [8].

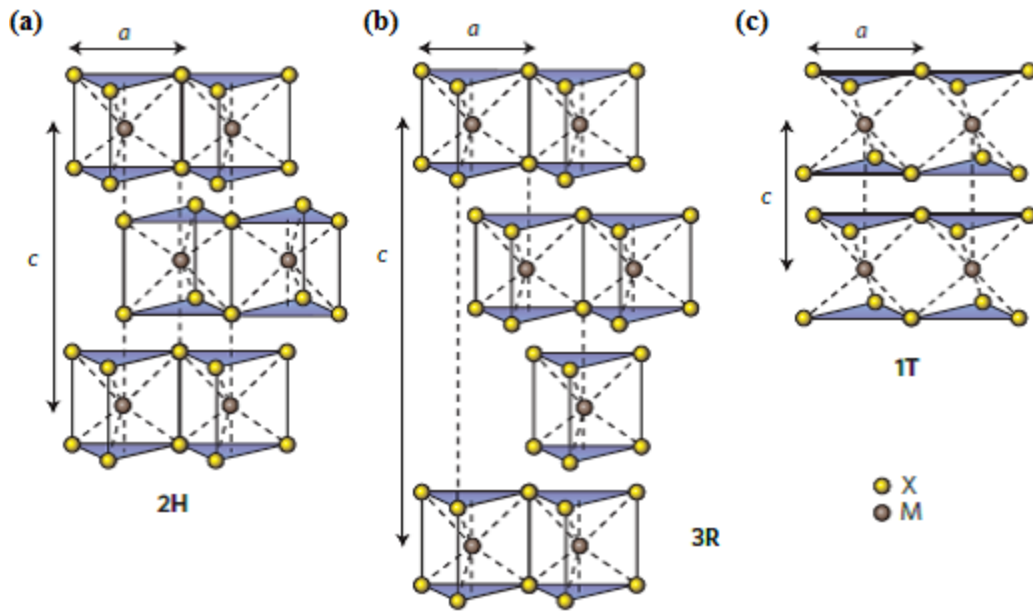


Figure 1: The structure of the (a) 2H , (b) 3R and (c) 1T phases of tungsten disulfide. The metal atoms (M) are grey and the chalcogen atoms (X) are yellow. [6]

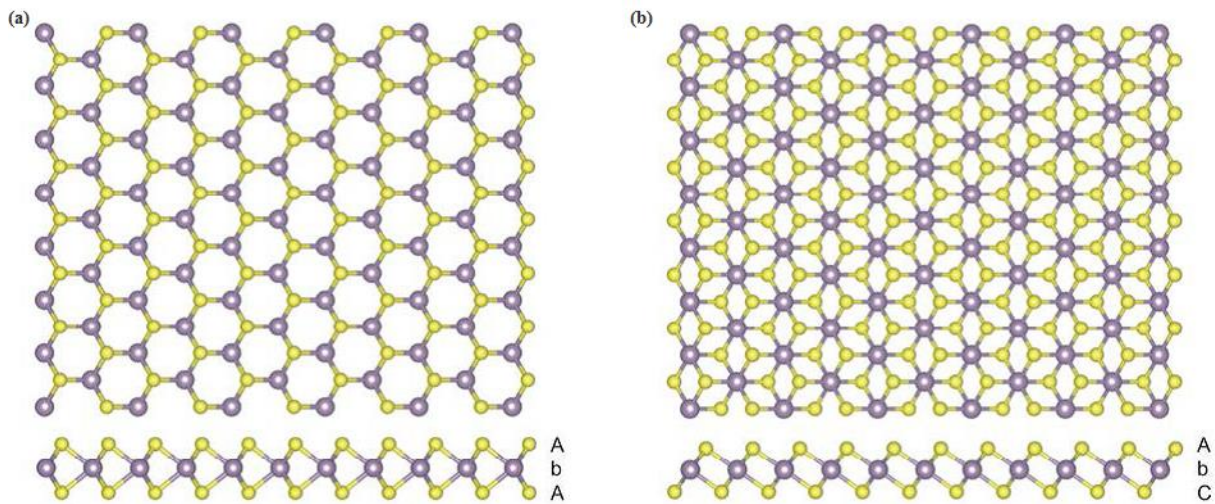


Figure 2: C-axis view of single-layer TMD with (a) trigonal prismatic (1H) and (b) octahedral coordination (1T). Purple spheres are the metal atoms and yellow spheres are the chalcogen. The labels AbA and AbC represent the stacking sequence where the upper- and lower- case letters chalcogen and metal elements, respectively [8].

I.1.3 Electronic band structure

The layered metal dichalcogenides present remarkable electronic properties ranging from metals to semiconductors to insulators. Tungsten disulfide is a semiconductor which has attracted a lot of interest. The electronic band structure properties of tungsten disulfide depend on the number of layers due to quantum effects and changes in symmetry. As the thickness of semiconductor is reduced to a single layer, the band gap energy is increased. In particular, bulk WS_2 is an indirect gap semiconductor with a bandgap in the near-infrared frequency range ($E \sim 1.3 eV$). Contrariwise, monolayer WS_2 is a direct bandgap semiconductor with an optical gap in the visible frequency range ($E \sim 2.1 eV$), as shown in Fig. 3(a) and (b). A direct gap exists at the K points of the Brillouin zone between the spin-orbit split valence band and the double degenerate conduction band. An indirect band gap starts from the minimum at a midpoint between Γ and K of the local conduction band and complete the formation at the Γ point of the valence band maximum [8]. Decreasing the number of layers from bulk causes a blue shift until the bilayer limit. Afterwards, the indirect band gap changes to direct gap, in the monolayer limit. For WS_2 , the magnitude of the blue shift is $1.16 eV$, as we go from the bulk phase to the monolayer limit (from indirect band gap to direct) [9].

As we have mentioned before, the thickness of the monolayer reaches $6 \sim 7 \text{ \AA}$, which is fairly enough to build z-directional quantum confinement effects. The location of the Fermi level represents the electronic properties. Band structure of TMDs is mainly determined by d-orbitals of transition metal and chalcogen atoms. Firstly, octahedral structured transition metal centers (D_{3d}) of TMDs form degenerate band structure composed of d_{z^2, x^2-y^2} and $d_{xy, yz, zx}$ orbitals while trigonal prismatic coordination (D_{3h}) gives rise to the band structure consisting of d_{z^2} , $d_{x^2-y^2, xy}$ and $d_{xz, yz}$ orbitals. The gap between these orbitals is trigonal prismatic coordination [8].

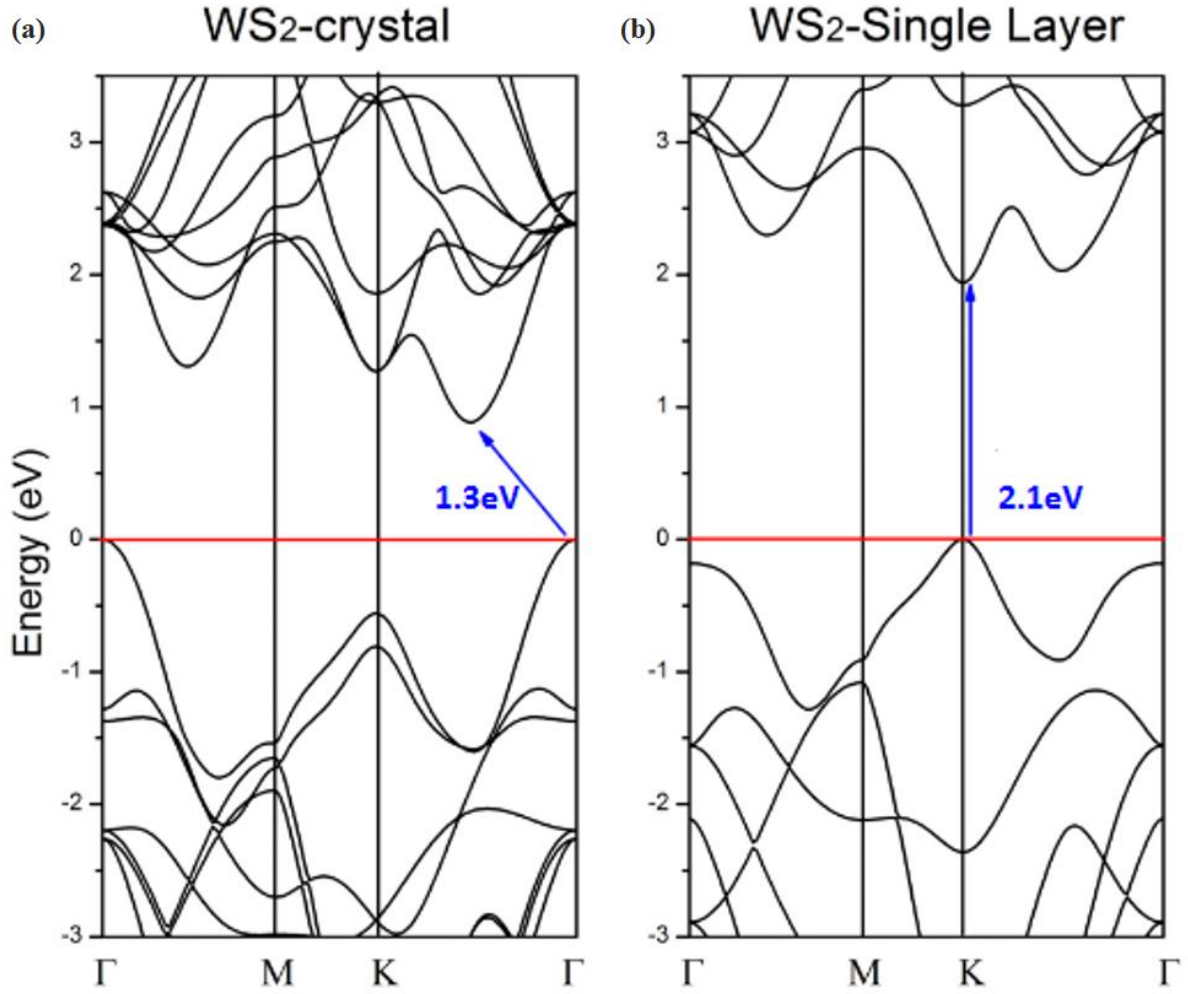


Figure 3: Band structure calculated from first-principle density function theory (DFT) for (a) bulk and (b) single-layer WS_2 . The blue arrows indicate the lowest energy transition (the $2H$ phase for bulk and the $1H$ phase for single-layer material) [10].

In monolayers, the conduction band minimum (CBM) and the valence band maximum (VBM) are both located at the corners of the first Brillouin zone. The six corners belong to two non-equivalent groups denoted by K and $-K$, respectively. Each group has three equivalent corners related to each other by reciprocal lattice vectors [11]. In the monolayer limit, direct bandgap appears at K point which is located at 6 corners of first Brillouin zone. Monolayer 2D TMD semiconductor becomes direct semiconductor while its bulk counterpart displays indirect semiconducting behavior. The reason for indirect to direct transition is explained by effective mass. The out-of-plane mass of electron and hole near the K point is much larger than the free electron mass m_0 . However, out-of-plane mass for holes near the Γ point is $\sim 0.4m_0$ and for electrons near the midpoint along Γ - K is $\sim 0.6m_0$. As the number of layers decrease, effective masses related to indirect transition are drastically increased while the effective masses at K

point are largely unchanged. As a result, in the monolayer limit, indirect bandgap becomes larger than direct bandgap and therefore 2D TMD semiconductor reveals direct band structure. The transition becomes the basis of significant increases in PL by ~ 1000 times compared to the bulk [12]. The electronic band structure influences the ability of the crystal to absorb or emit light.

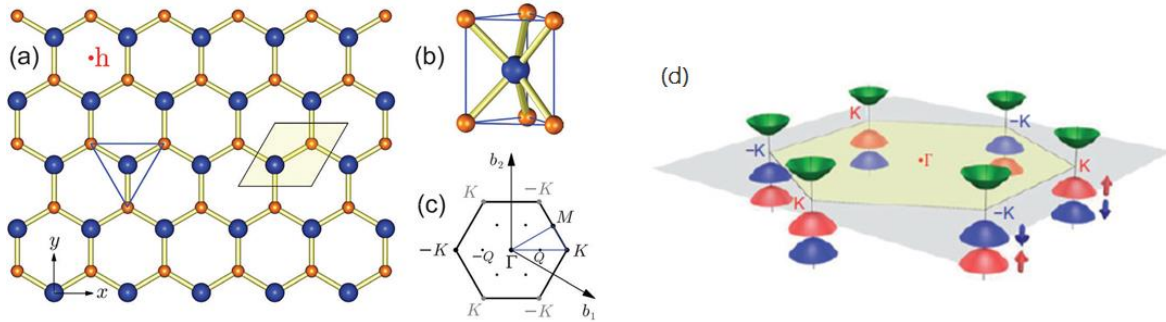


Figure 4: (a) Top view of monolayer WS_2 . The blue and orange spheres represent W and S atoms, respectively. The light yellow diamond region is the 2D unit cell. (b) Trigonal prismatic coordination geometry, correspond to the blue triangle in top view. (c) The first Brillouin zone from top view [11]. (d) 3D representation of first Brillouin zone of WS_2 showing six valleys and valence band splitting by spin-orbit coupling at the K points. The green surfaces illustrate the conduction band and its minimum. The red and blue surfaces exhibit split valence band [12].

I.1.4 Optical and vibrational properties

The electronic band structure of WS_2 affects the optical and vibrational properties. The increase of the band gap energy, as the number of layers decreased, can be observed in Raman, absorption and photoluminescence spectra. In direct band gap semiconductors, electrons in the valence bands can be easily excited to the conduction bands by incident photons, and the excess carriers can also recombine, passing the excess energies to photons as shown in Fig. 5 [13]. The former process can be probed by light absorption measurements and the latter process can be probed by photoluminescence (PL) measurements.

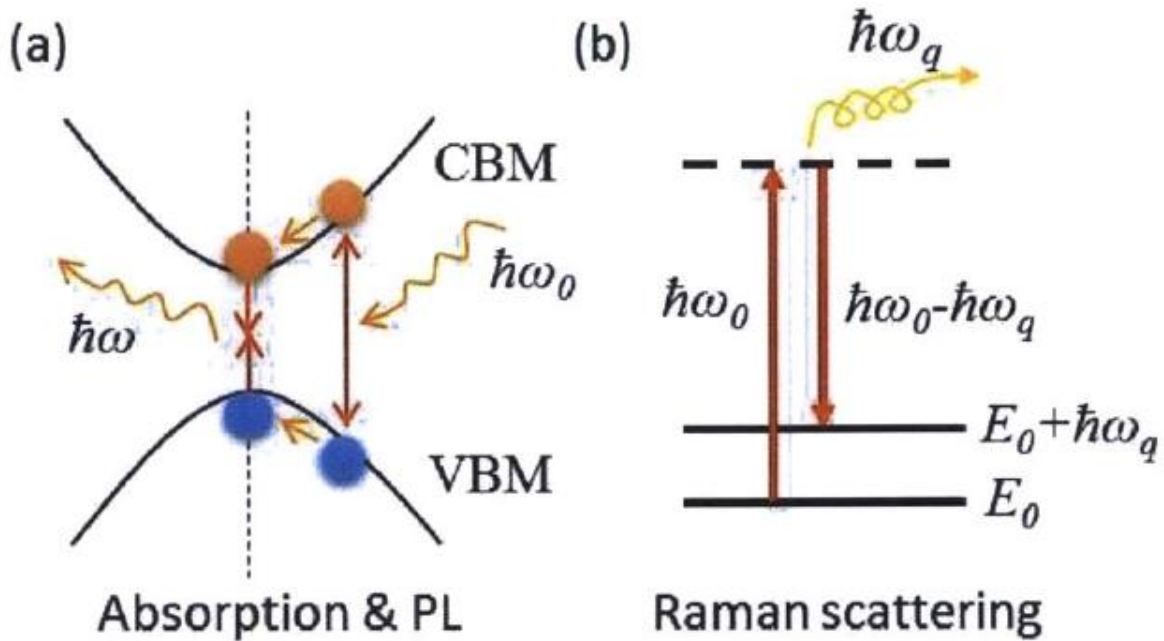


Figure 5: Schematics of (a) the light absorption ($\hbar\omega_0$) and the photoluminescence ($\hbar\omega$) process and (b) the Raman scattering process. Here $\hbar\omega_0$ is the energy of the incident light, $\hbar\omega$ is the energy of the emitted light in the PL process and $\hbar\omega_q$ is the energy of the emitted phonon in the Raman scattering process. VBM is the valence band maximum and CBM is the conduction band minimum. E_0 is the ground energy state [13].

In lattice vibrations, phonons are involved in the optical transitions. The generated photon can have a lower energy than the incident photon, and the energy difference is related to a specific phonon mode. The inelastic light scattering is called Raman scattering [13]. For the Raman spectrum of WS_2 , as it transits from bulk to monolayer the position of its main Raman peaks changes. The main Raman peaks are the in-plane E_{2g}^1 and the out-of-plane A_{1g} mode. As the layer thickness decreases, the A_{1g} mode decreases in frequency whereas the E_{2g}^1 mode increases [14]. Thus, the layer number can be determined using Raman spectroscopy. The

shift in the Raman peaks appears due to two reasons. Firstly, the influence of neighboring layers on the effective restoring forces in atoms and secondly due to long-range Coulomb interactions increasing the dielectric screening [15].

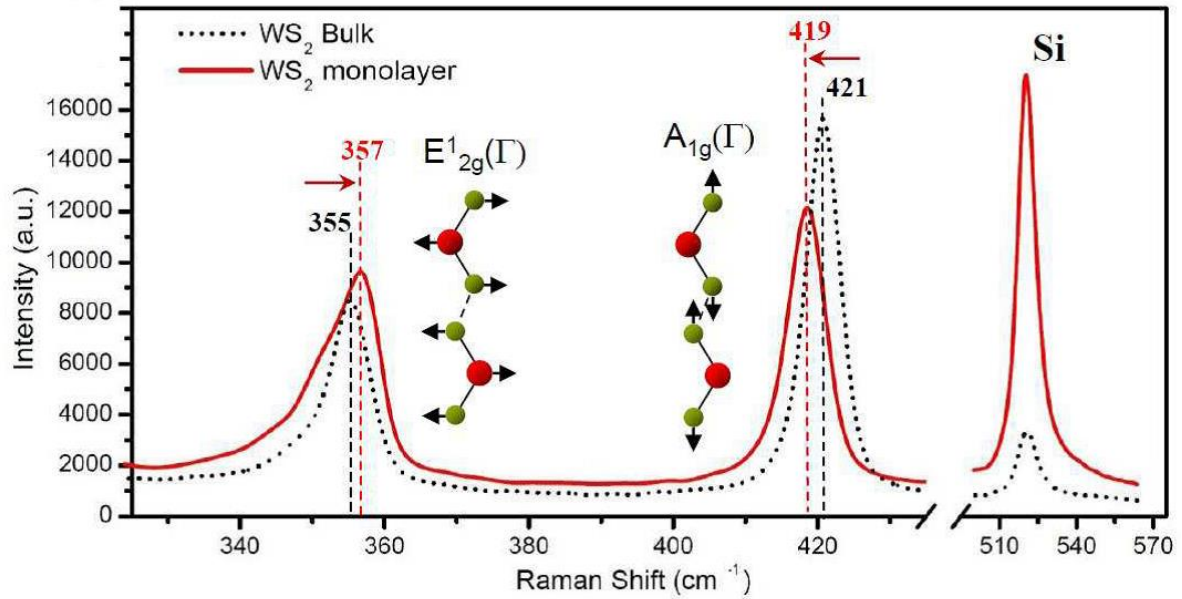


Figure 6: Raman spectra for WS₂ bulk (dotted) and for a monolayer (solid line) at room temperature ($T=300K$) [16].

In 2D TMDs, light-generated electrons and holes tend to attract each other due to the strong Coulomb interaction between them. This can be modeled by the exciton, which is the combination of the quasiparticle state of an electron and a hole [13]. The monolayer of this crystal has promising optoelectronic applications and can be probed by a variety of spectroscopic tools. For example, photoluminescence in bulk 2H-WS₂ is very weak, as it is a phonon-assisted process and it is known to have negligible quantum yield. A bright PL is detected in monolayer WS₂, which is expected as a semiconductor with direct-gap. The transition from indirect to direct band gap is attributed to the absence of weak interlayer coupling in the monolayer. Two peaks (A and B) are observed in the absorption spectra corresponding to transitions between splitted valence bands and the conduction band. The energy splitting between A and B arises from the combined effect of interlayer and spin-orbit coupling (SOC) in the bulk crystal, contrariwise in a single layer energy splitting comes only from SOC, because of the absence of interlayer coupling. Bound energy levels situated in the band gap region. Strong spatial confinement and reduced screening effect are the reasons why two dimensional materials enhance this excitonic effect [17]. The properties of two dimensional materials significantly depend on the layer number, which is important for applications. At a

photoluminescence spectrum the position and intensity of the peaks are changing with the number of layers. A monolayer of WS_2 gives a very strong PL emission, which is weakened with increasing the number of layers. PL emission is very sensitive to temperature, defects and doping so it is not accurate to identify the number of layers with this method. However, Raman spectroscopy is a nondestructive, accurate and reliable method for the characterization of a single-layer WS_2 .

Optical experimental studies have reported peaks at $\sim 2.05\text{eV}$ and $\sim 2.4\text{eV}$ which were originated from the transition in the K-point of the Brillouin zone at $T=78\text{K}$. Two separate exciton bands, the A and B excitons, can be produced due to valence band splitting. Valence band (VB) splits at the K-point, due to spin-orbit coupling (SOC) in the monolayer and also the interlayer interaction energy in multi-layers. Absorption spectra are in accordance with PL measurements about the position of the A and B exciton transitions. [1].

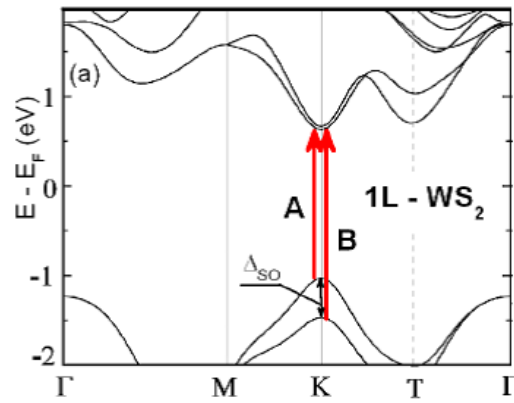


Figure 7: Band structure of single layer WS_2 crystal, calculated by density functional theory. The red arrows indicates the direct band gap and the transition of A and B excitons. Δ_{SO} represents the energy of the split valence band maximum due to spin-orbit coupling [1].

I.1.5 Spin, orbit and valley interactions

Materials that have strong spin splitting can push the system out of equilibrium due to various effects or due to symmetry breaking, allowing spin-polarized carrier populations to be maintained. A set of conditions gives rise to both strong spin-orbit induced electronic band structure splitting and spin-valley coupling. Monolayer WS_2 lack inversion symmetry, unlike bilayer WS_2 , bulk WS_2 and graphene which are centrosymmetric. A monolayer of dichalcogenides has a honeycomb lattice structure in which the inversion symmetry is naturally broken due to two different types of atoms (transition metal and chalcogen), as illustrated in Fig. 8 [1].

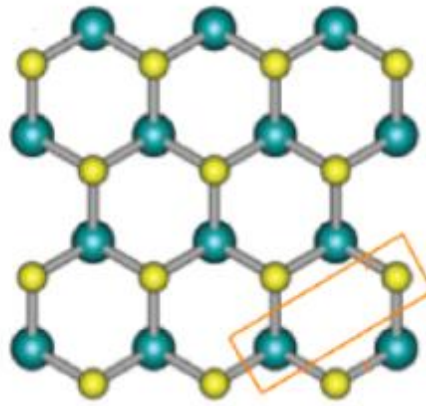


Figure 8: The breaking inversion symmetry can be observed from a top view of a hexagonal lattice in monolayer dichalcogenides. Green and yellow spheres denote the metal (W) and chalcogen atoms (S), respectively [18],[1].

In many non-centrosymmetric semiconductors non-equivalent energy exists in the band structure, so they called valleys in their Brillouin zone [6]. The lack of inversion symmetry, the confinement of in plane motion of electrons and the high mass of the elements in the MX_2 materials, has as a result a very strong spin-orbit coupling with the valence band splitting ranging between $0.15eV$ and $0.45eV$. For monolayer WS_2 , the valence band splitting is $0.40eV$. This is in contrast to graphene, which has very weak spin-orbit interaction due to the low mass of carbon. The lack of inversion symmetry along with the strong spin-orbit leads to the coupling of spin and valley physics. The bandgap of monolayer WS_2 is located at the $K(K^-)$ valley in the Brillouin zone and the inversion symmetry is broken. The bottom of the conduction band (CB) and the top of the valence band (VB) around the K valley are both constructed from metal d orbitals. The spin-orbit coupling splits the valence band. As a result of time-reversal symmetry, spin splitting has the opposite sign at the K and K^- valleys. If the electron spin at

the top of valence band is pointing up at the K valley, then the electron spin at the K^- valley must be pointing down. There is a valley-selective interband optical selection rule around the K (K^-) in monolayer WS_2 , due to the inversion symmetry. The interband transition near of the K (K^-) point, is coupled exclusive to right (left) handed circularly polarized light σ_+ (σ_-) as sketched in Fig. 9. At PL measurements, two peaks are shown, coming from the band edge. The A exciton, and a weaker peak at a higher energy, which can be attributed to the emission from the spin-split valence band. The energy difference between the two PL peaks implies spin splitting in the valence band due to the spin orbit coupling at the K valley [19].

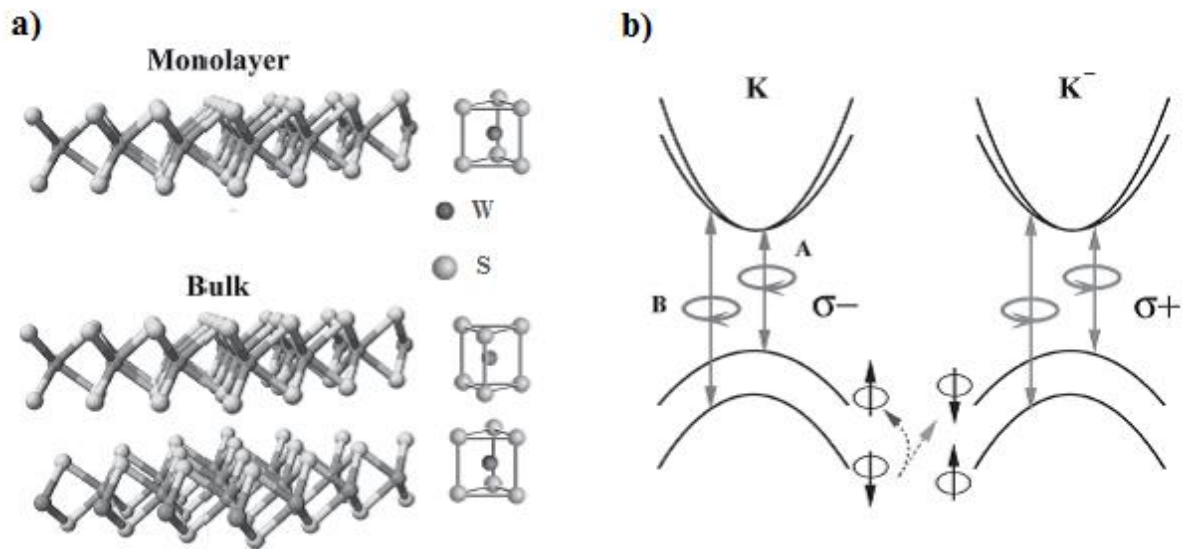


Figure 9: a) Schematics of the WS_2 structure. The unit cell of bulk crystals and even-layer film includes two sub-cells stacking at 2H packing order. b) The valley selective optical selection rules. Curvatures at the K and K^- valleys include interband circular dichroism: left-handed circularly polarization at the K valley and right-handed at the K^- . The spin orbit coupling includes spin splitting of the valence band at the K and K^- valleys [19].

I.1.6 Excitonic effects

Excitonic effects are dominant in a monolayer of TMDs. During the photon absorption, a valence band electron is excited to the conduction band leaving behind a vacancy (hole) in the valence band. The attractive Coulomb interaction between the negatively charged electron and positively charged hole bind them into a hydrogen-like state, called as exciton (X). The electron-hole pair can also capture an extra electron or hole to form a charged exciton (X^\pm), which also referred as trion [1]. The binding energy of a neutral exciton is defined as its lower energy compared to the free electron-hole pair, while the trion binding energy is the difference between X^\pm energy and the unbound state of the neutral exciton, plus a free electron or hole. In the PL spectra this corresponds to the separation between neutral exciton emission energy (X) and the charged exciton emission energy (X^\pm). In monolayer dichalcogenides, the binding energy is four times larger than that of the binding energy at a bulk crystal. In monolayer, the excitons are strongly confined in the plane and experience reduced screening due to the change in the dielectric environment outside of the layer [1]. A binding exciton energy in monolayer WS_2 is $\sim 400\text{meV}$ [20], which is at least six times larger than in bulk [21]. The trion binding energy which depends upon the Fermi level has been determined to be $20 - 40\text{ meV}$ in WS_2 [22].

The spin-orbit coupling into the valence band give rise to two distinct exciton feature the A and B in schematic absorption spectrum [1]. The neutral exciton shows a large binding energy, E_A . The exciton feature exhibit a fine structure, which can be identified with formation of trions (X_{A^-} and X_{B^-}) with binding energies E_{A^-} and E_{B^-} [1]. It is worth to notice the A exciton we will call it as X exciton or neutral exciton.

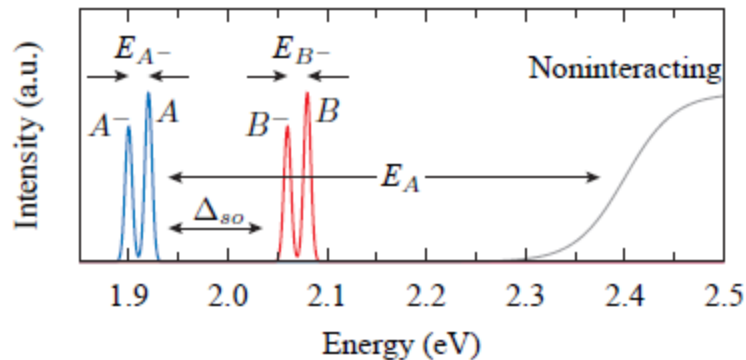


Figure 10: Absorption spectrum which shows the A (blue) and B (red) excitons that result from the sizable spin-orbit splitting [23].

I.2 Micro-Raman Spectroscopy and micro-PL Spectroscopy

This chapter describes the experimental techniques, spectroscopic methods where used in the preparation of this thesis. For optical characterization and study of Tungsten disulfide on SiO_2/Si are principally used Raman and photoluminescence spectroscopy (micro-PL). Then we can describe those techniques. Raman spectroscopy can be considered as an alternative, reliable and non-destructive technique to identify the number of WS_2 layers. In this work, micro-Raman spectroscopy was used as an in situ tool in order to verify the monolayer character of the sample [1].

A monolayer of MX_2 group of materials is found to exhibit an enhanced PL compared to thicker crystals. Similarly, in our samples the PL emission from a monolayer region, previously confirmed by Raman measurements was stronger emission than the multi-layer region [1]. We note that we observe change in the emission PL maxima with changing the position of the laser spot on the sample. The laser spot size is $1\mu m$.

I.2.1 Mechanism of Raman and Rayleigh scattering

The interaction of light with solid can be described as reflection, transmission, absorption and scattering. In the case of scattering and more specifically, elastic scattering has changed only the direction with no energy loss [24]. Only a fraction of light is inelastically scattered and is first discovered by C. V. Raman. The observation of inelastic or Raman scattering has been studied to understand the vibrational and rotational states in solid and gas molecules.

The quantum picture of Raman scattering can be explained as follows: a band of vibrational states exists near the electron ground state. A beam of monochromatic light excites the electrons from the ground state to a virtual state. The electrons undergo relaxation process with emission of photon most electrons return to their ground state thus the photon has the same energy as the incoming one, which is the elastic scattering process or Rayleigh scattering. But there is a small number of electrons relax to the vibrational states and by the conservation of energy, the emitted photon has different energy to the original photon (inelastic or Raman scattering) [25]. In Raman spectroscopy, the scattered photons are collected and the intense Rayleigh signal is blocked by filter leaving only the photons from Raman scattering. Usually the Raman signal is weak and close to the energy of Rayleigh line. Laser beam is used as the

monochromatic light source and band-stop filter with a very narrow stopband (notch filter) is applied to block the Rayleigh line. In the Raman spectrum, lines that have slightly lower or higher energy comparing to the Rayleigh line are named as Stokes and anti-Stokes line, respectively. Raman spectroscopy has a wide range of applications such as identification of chemical bonds and symmetry in molecules and crystal orientation and lattice strain. It also has the advantage of being non-destructive [25].

Light scattering techniques is a very useful tool to probe the fundamental excitations in solids, such as phonons, plasmons. In a typical experiment, an incident monochromatic light with energy $h\nu_0$ impinges on a crystal [1]. The majority of the scattered photons will be scattered elastically, namely with the same frequency as the incident photons. This type of scattering is called Rayleigh scattering. Additionally, a small proportion of scattered photons can be have lower (Stokes) or higher (anti-Stokes) energy than the incoming photon. These photons will be scattered with a different frequency than the incident radiation leading to Raman scattering. An incident photon with energy $h\nu_0$ interacts with a molecule, which absorbs the energy of the photon and switches to an excited potential (virtual) state with an average life time of $10^{-14}sec$ [26]. Typical average lifetimes of electronic states are $10^{-8}sec$. The molecule instantaneously loses energy and switches to a lower energy level by emitting a photon. In Rayleigh scattering, the molecule returns to the energy level which stimulated. In this case, the energy of the incident photon is $h\nu_0$ (elastic scattering). In Stokes resonance scattering, the electron isn't switches in the basic vibrational state $u=0$ but in vibrational level $u=1$. The scattered photon has less energy than the incident photon $h\nu_0 - h\nu_1$. In Anti-Stokes resonance scattering, molecule absorbs the energy of the incident photon while it is in the excited vibrational state ($v=1$) and then switches from the potential state in the basic $u=0$, emitting a photon with energy $h\nu_0 + h\nu_1$. Vibrational modes of molecules function as quantum harmonic oscillators and permissible transitions in resonance scattering are $\Delta u = \pm 1$. Normally, the energy of the incident light varies from $1.2 - 3 eV$ and the vibrational energy $h\nu_1$ varies from 1 to $370meV$ [27].

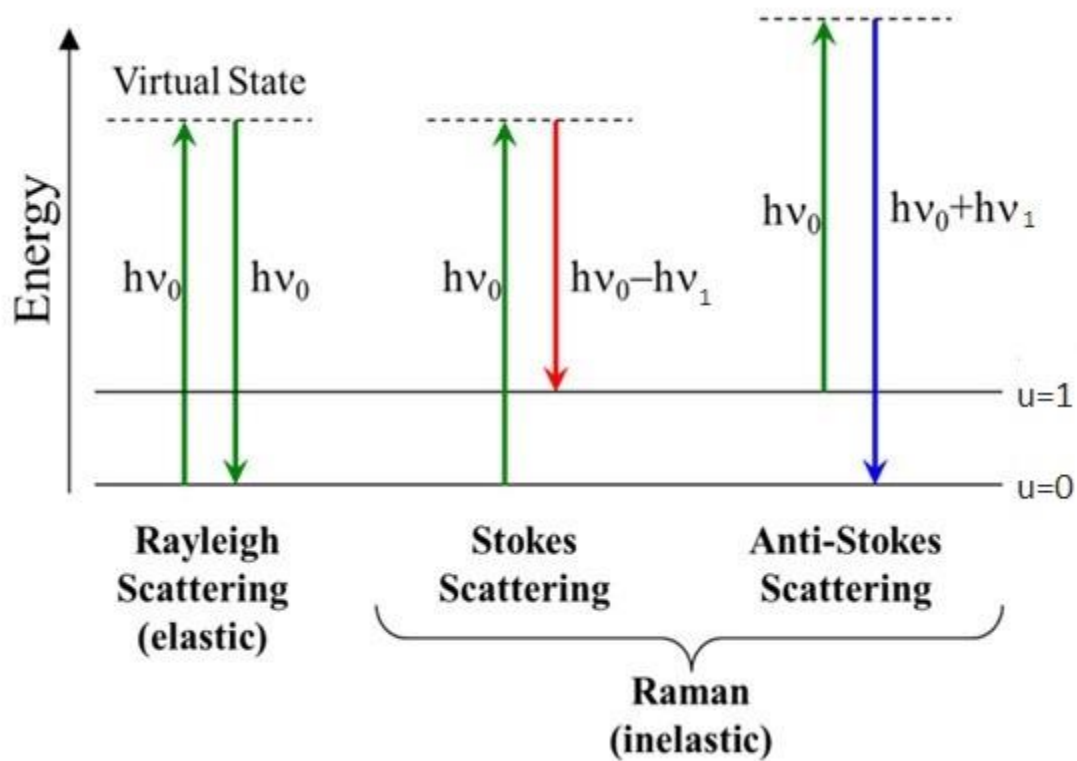


Figure 11: Quality chart description of Rayleigh and Raman scattering mechanisms [28].

It is worth to notice that in contrast to the photoluminescence process, in the Raman scattering process, the intermediate states are “virtual” states because they do not have to correspond to any optical excitation of the electronic levels of the system [1].

I.2.2 Theory of Raman scattering

Macroscopic description of Raman phenomenon is a good explanation and qualitative understanding of the experimental spectra. A stimulate radiation has an intensity of electric field E of the electromagnetic field and is described by the following formula:

$$E = E_0 \cos(2\pi\nu_L t) \quad (1)$$

Where ν_L is the excitation frequency, for example $\nu_L = 473nm$. E_0 is the amplitude of the electric field. The external electromagnetic field exerts time dependent and opposite directions forces to electrons and protons of the molecule. Thus the “center of gravity” of negative charge to be displaced on the equivalent of positive charges. An incident dipole moment has a vibrational frequency ν_L of external electromagnetic field. The induced dipole moment associated with E can be expressed by the following formula:

$$p_{ind} = a \cdot E \quad (2)$$

Where a is the polarizability of the molecule, the easy way to polarize electronic cloud under the influence of electromagnetic field. In general, polarizability is a 2nd order tensor. From equations (1) and (2):

$$p_{ind} = a \cdot E_0 \cos(2\pi\nu_L t) \quad (3)$$

From classical electromagnetism, it is known that the intensity of the light of a vibrating dipole is proportional to the forth power of vibrational frequency of a dipole, as well as proportional to the square of the maximum value of p_{ind} . In case of equation (3), we have $a^2 E_0^2$ ($I \sim \nu^4 a^2 E_0^2$). The polarizability in molecules is not constant but varies during certain vibration modes or rotation. The distribution of electronic cloud is not the same in two vibrational limit positions. In the case of a polyatomic molecule, for small shifts from the equilibrium positions of atoms, polarizability can develop in Taylor series as:

$$a = a_0 + \left(\frac{da}{dQ}\right)_0 + \dots \quad (4)$$

Where a_0 is the polarizability at the equilibrium position, Q is the normal coordinate of the vibration and $\left(\frac{da}{dQ}\right)_0$ is the change of polarizability relative to the Q in equilibrium position of

individuals that composing the molecule. Then we consider that terms larger than second class as Q in equation (4) have zero polarizability. This approach called harmonic approach. The Q varies harmonically with the time according to the relationship:

$$Q = Q_0 \cos(2\pi\nu_{nib}t) \quad (5)$$

where ν_{nib} is the vibration frequency of oscillation, from equations (4) and (5)

$$a = a_0 + \left(\frac{da}{dQ}\right)_0 Q_0 \cos(2\pi\nu_{nib}t) \quad (6)$$

By replacing equation (6) in (2) :

$$\begin{aligned} p_{ind} = & a_0 E_0 \cos(2\pi\nu_L t) \\ & + E_0 Q_0 \left(\frac{da}{dQ}\right)_0 \cos(2\pi\nu_{nib}t) \cos(2\pi\nu_{nib}t) \end{aligned} \quad (7)$$

and use the trigonometric identity

$$\cos A \cdot \cos B = [\cos(A + B) + \cos(A - B)]/2 \quad (8)$$

$$\begin{aligned} p_{ind} = & a_0 E_0 \cos(2\pi\nu_L t) + \frac{E_0 Q_0}{2} \left(\frac{da}{dQ}\right)_0 \cos[2\pi(\nu_L + \nu_{vib})t] \\ & + \frac{E_0 Q_0}{2} \left(\frac{da}{dQ}\right)_0 \cos[2\pi(\nu_L - \nu_{vib})t] \end{aligned} \quad (9)$$

As seen from the above equation p_{ind} and the intensity of scattered radiation consists of three components. The first component vibrating with ν_L frequency leads to Rayleigh scattering and the vibrating frequencies $\nu_S = \nu_L - \nu_{vib}$ and $\nu_{AS} = \nu_L + \nu_{vib}$ lead to Stokes and Anti-Stokes Raman scattering, respectively. It is worth noting that if $\left(\frac{da}{dQ}\right) = 0$, the amplitudes of Raman components of the induced dipole will be zero, so we have no radiation from Raman. As a general conclusion we can say that to observe a molecular vibration with Raman spectroscopy, there should be a change to the polarizability of the molecule during vibration. Therefore, while the classical theory provides right the appearance and position of Stokes and Anti-Stokes lines, lead to wrong results for the ratio of relative intensities, it fails to appreciate the value of $\frac{I_S}{I_{AS}}$. The ration $\frac{I_S}{I_{AS}}$ is certainly less than one and it is in contrast with the fact that

the Stokes lines are more potent than the Anti-Stokes lines [27]. The discrepancy eliminated in quantum theory of Raman effect.

$$\frac{I_S}{I_{AS}} = \left(\frac{\nu - \nu_{vib}}{\nu + \nu_{vib}}\right)^4 e^{h\nu_{vib}/kT} \approx e^{h\nu_{vib}/kT} \quad (10)$$

I.2.3 Raman spectroscopy of WS_2

Raman spectroscopy has become a very powerful tool for studying one and few layers of tungsten disulfide (WS_2). Raman spectroscopy can not only used to identify the number of layers, but also gives details about the electronic band structure, a determination of the structural distortion. Also, gives information about doping concentration, strain effect and phonon dispersion through resonant Raman scattering [29]. The vibrational spectra are sensitive to the thickness of the crystal, so with a small change at Raman modes can be used to differentiate between bulk, monolayer, bilayer and tri-layer crystals. Resonant Raman spectra are composed of both first- and second-order Raman excitations. At the Brillouin zone center, we have four Raman active modes, which are first-order phonon modes: A_{1g} , E_{1g} , E_{2g}^1 and E_{2g}^2 . In the back scattering configuration, the E_{1g} mode is forbidden and the E_{2g}^2 mode is observed in the very low frequency region. Also, E_{2g}^2 is a shared mode originating from the relative motion of the atoms in different layers, so is absent in a single-layer of a sample [30].

Raman spectra for bulk WS_2 include first order modes at the Brillouin zone center ($E_{2g}^1(\Gamma)$ and $A_{1g}(\Gamma)$) plus a zone-edge mode which has been identified as the longitudinal acoustic mode at the M point LA (M). Additional peaks correspond to multi-phonon combinations of these modes. For the mechanically exfoliated WS_2 , we give attention to the first order $E_{2g}^1(\Gamma)$ and $A_{1g}(\Gamma)$ optical modes. Figure 12 show a typical Raman spectra of monolayer WS_2 regions using 488nm excitation. The Raman spectrum is dominated by the first order modes: LA (M) at $176cm^{-1}$, $E_{2g}^1(\Gamma)$ at $356cm^{-1}$ and $A_{1g}(\Gamma)$ at $418cm^{-1}$. When a monolayer WS_2 is excited at 514.5nm, the Raman spectrum become very rich uncovering many second-order peaks that are stronger than those observed in the bulk material [29].

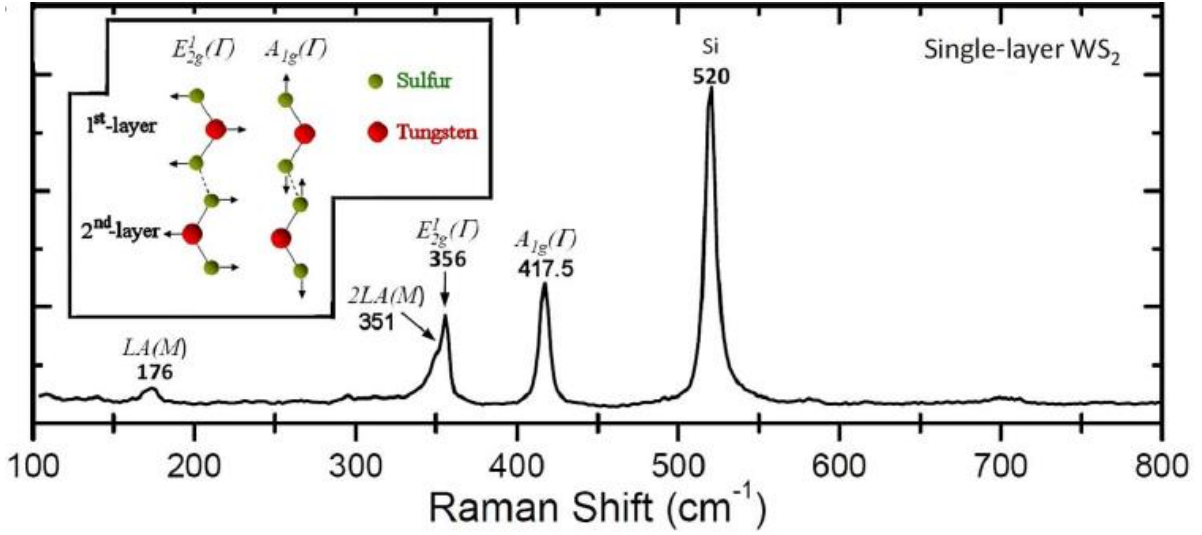


Figure 12: The atomic displacements for the in-plane phonon mode $E_{2g}^1(\Gamma)$ and the out-of-plane phonon mode $A_{1g}(\Gamma)$ [29].

Subsequently, we give attention to the Raman spectra as a function of thickness. The Raman spectra of a single-layer WS_2 are dominated by three first-order Raman modes: $E_{2g}^1(\Gamma)$, which is associated with the in-plane motion of the sulfur and tungsten atoms in opposite directions, $A_{1g}(\Gamma)$ which is associated with out-of-plane motion of the sulfur atoms and LA(M) [31]. The longitudinal acoustic phonons LA (M) are in-plane collective movements of the atoms in the lattice, similar to the sound waves. There are periodic expansions and compressions of the lattice that occur along the direction of propagation [29]. The momentum q of the phonon has a specific direction and magnitude, for this reason we use the symbol (M) to express this momentum. In the phonon dispersion they appear at the M-point of the Brillouin zone. In bulk WS_2 , the separation between $E_{2g}^1(\Gamma)$, $A_{1g}(\Gamma)$ is 65cm^{-1} and it decreases gradually with the number of layers reaching 58cm^{-1} for a single layer [32].

These spectra are normalized to the substrate Si peak. The A_{1g} mode arises from the out of plane motion of sulfur atoms, while the E_{2g}^1 results from the opposing in-plane motion between the sulfur and tungsten atoms [33].

Second-order Raman modes have been reported in monolayer WS_2 . Such resonant vibrational spectra can provide additional information concerning the electronic properties [29]. It has been suggested that the observation of a strong second-order Raman resonance involving the longitudinal acoustic phonons (2LA) in monolayer WS_2 is the signature of the monolayer nature of the sample. The intervalley scattering process involving the 2LA phonon was suggested to be the main source of valley depolarization. This enhanced feature on the low

energy side of the E_{2g}^1 Raman peak, has been identified as a second order mode involving two LA phonons from the M-point in the Brillouin zone. This LA phonon is similar to that seen in Raman scattering from folded acoustic phonons observed in superlattices. While our measurements is configured in a backscatter geometry, the WS_2 monolayer is on SiO_2/Si substrate and therefore some incident light is transmitted through WS_2 and is then reflected from the silicon substrate and returns in a Raman forward –scattering geometry. This produces a mixed forward and backward scattering result and may contribute to the broadened line shape of the 2LA(M) mode [34].

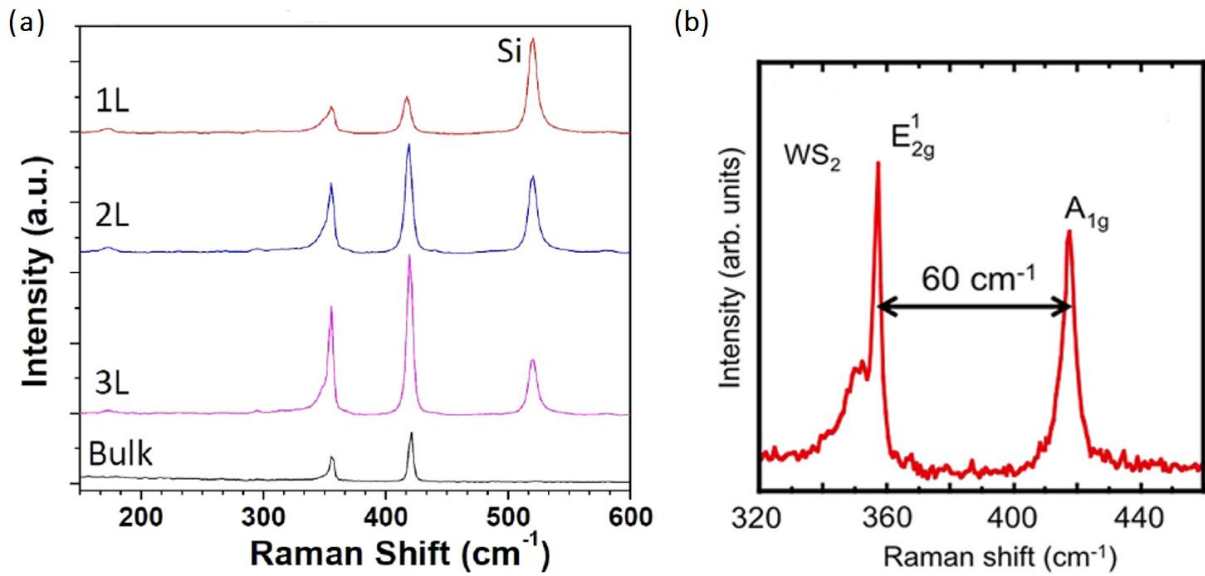


Figure 13: (a) Raman spectra collected from regions with different WS_2 thicknesses (1L, 2L, 3L and bulk) using $\lambda_{exc} = 488nm$ [29]. (b) Raman spectrum of the monolayer region 2H – WS_2 taken at 300K with an excitation energy at 488nm [35].

In Fig. 14 we can see that, as the number of layers increases the frequency separation between two main Raman modes, E_{2g}^1 and A_{1g} increases gradually. The A_{1g} mode blueshifts when increasing the number of WS_2 layers. This hardening of the A_{1g} mode is consistent with the increasing restoring force caused by van der Waals interactions established among layers [14]. The E_{2g}^1 phonon mode exhibit very subtle redshifts when increasing the number of layers [36]. The stiffening of the out of plane A_{1g} mode has been explained by the increasing interlayer interaction and rise in restoring forces on the atoms with the number of layers [14]. In contrast, the E_{2g}^1 mode softens. For this mode, the atoms move in plane and the influence of the interlayer interaction stiffening is thus expected to be smaller. The observed softening has been attributed to an enhanced dielectric screening providing by additional layers [15]. The most intense

features in the Raman spectrum correspond to the $E_{2g}^1(\Gamma)$ and $A_{1g}(\Gamma)$ modes and the intensity ratio $E_{2g}^1(\Gamma)/A_{1g}(\Gamma)$ does not show major changes with the number of layers [29].

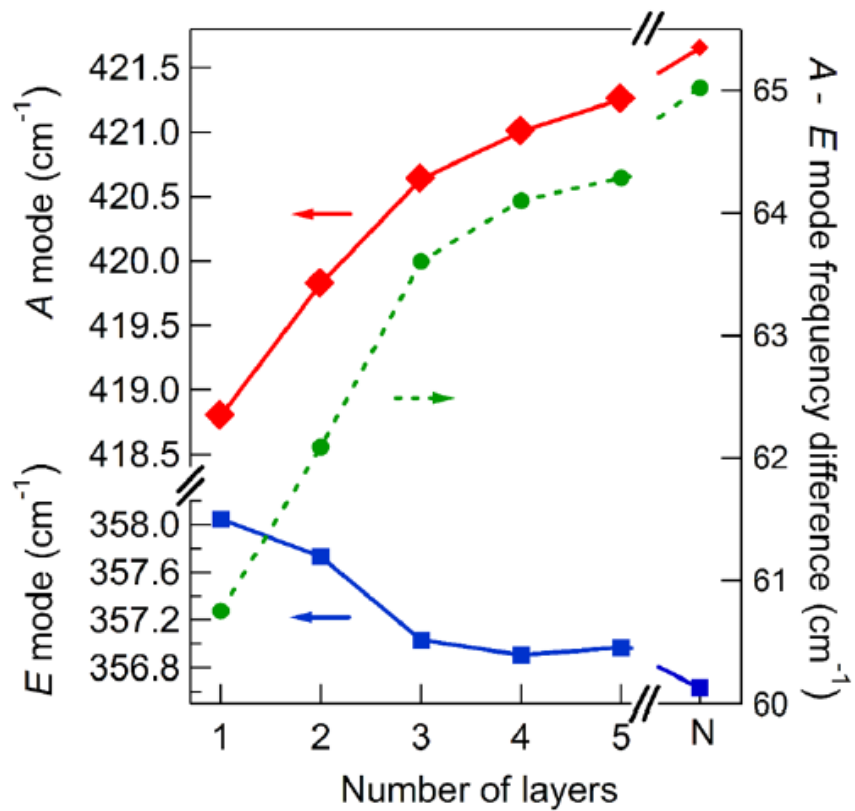


Figure 14: Evolution of the frequency of main E_{2g}^1 and A_{1g} modes with the number of layers. The dashed line shows the frequency separation between the E_{2g}^1 and A_{1g} mode [37].

Raman spectroscopy measurements of single-layer WS_2 have revealed unexpected trends of the vibrational properties when the number of layers changes.

I.2.4 Introduction to photoluminescence (PL)

Photoluminescence is a type of radiation due to the absorption of photons. It is the reverse effect of interband absorption of light. Luminescence is the phenomenon which explains the photon emission during the decay of an electron, from an excited state to a lower energy state. The difference of high and low energy is attributed to the energy of the emitted photon. The reproduction light after absorption of a photon with greater energy, is called photoluminescence. The phenomenon of photoluminescence presents greater complexity than the phenomenon of absorption. The shape and form of the spectrum of photoluminescence, influenced by the distribution of electrons and holes in the energy bands.

There are two pre-requisites for luminescence: the luminescent material must have a semiconductor structure with a non-zero band gap E_g and energy must be imparted to this material before luminescence can take place. The mechanism of photoluminescence in semiconductors is schematically illustrated in Figure 15 [38].

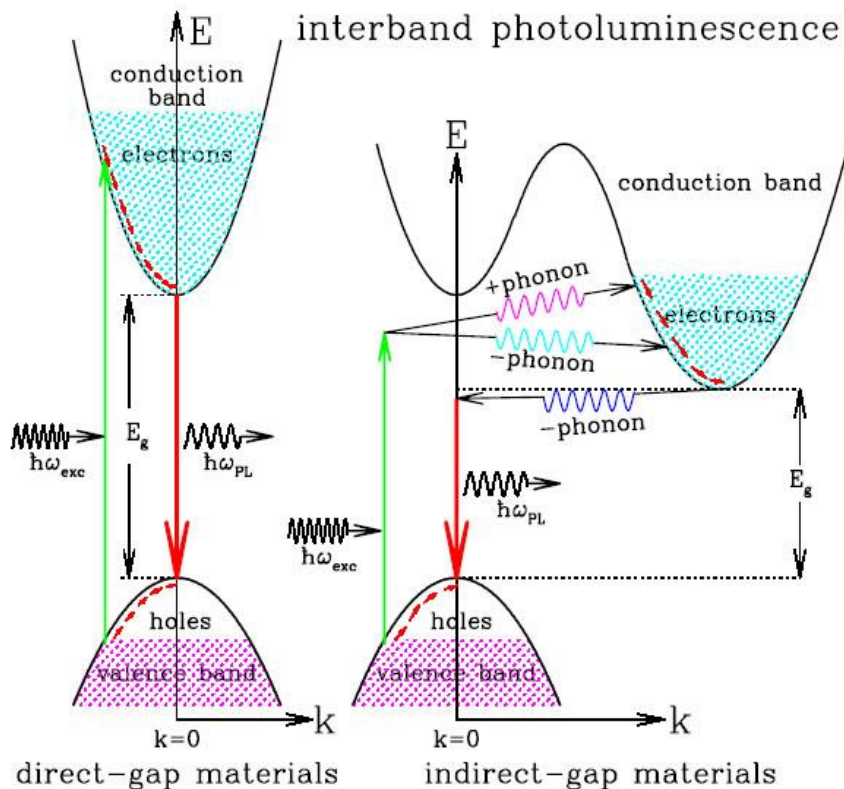


Figure 15: Schematic band diagrams for the luminescence processes in a direct gap material (left) and indirect gap material (right) [39].

In this figure, we can see the E-k diagrams for a direct band gap material (left) and an indirect band gap material (right), where E is the kinetic energy and k the wave vector (or momentum vector) of the electron or hole ($E = \frac{\hbar^2 k^2}{2m}$, where $\hbar = h/2\pi$ and m is the electron or hole effective mass). The direct and indirect materials are distinguished by their relative positions of the conduction band minimum and the valence band maximum in the Brillouin zone (the volume of k space containing all the values of k up to π/a where a is the unit lattice cell dimension [39]). In a direct gap material, both the conduction band minimum and the valence band maximum occur at the zone center where $k = 0$. In an indirect band gap material, however, the conduction band minimum does not occur at the zone center but rather at the zone edge or close to it. The shaded states at the bottom of the conduction band and the empty states at the top of the valence band respectively represent the electrons and holes created by the absorption of photons with energy $\hbar\omega_{exc} > E_g$. The cascade of transitions within the conduction and valence bands represents the rapid thermalization of the excited electrons and holes through phonon emission. Both the photon absorption and emission processes (the electron-hole recombination) can conserve momentum. Since that the momentum of the absorbed or emitted photon is negligible compared to the momentum of the electron. We therefore, represent photon absorption and emission processes by vertical arrows on E-k diagrams. To conserve momentum, the photon absorption process must involve either absorption (indicated by the “+” sign) or emission (indicated by the “-” sign) for a phonon.

A simple model for the photoluminescence in a semiconductor includes three stages: stimulation, relaxation and recombination. Incident photons pump electrons after the absorption from the valence band to conduction band, leaving behind a hole. The electron and hole relax at a lower energy within the structure of bands until they reach the end of the bands. The energy gap must be large enough for these processes, in order to achieve recombination.

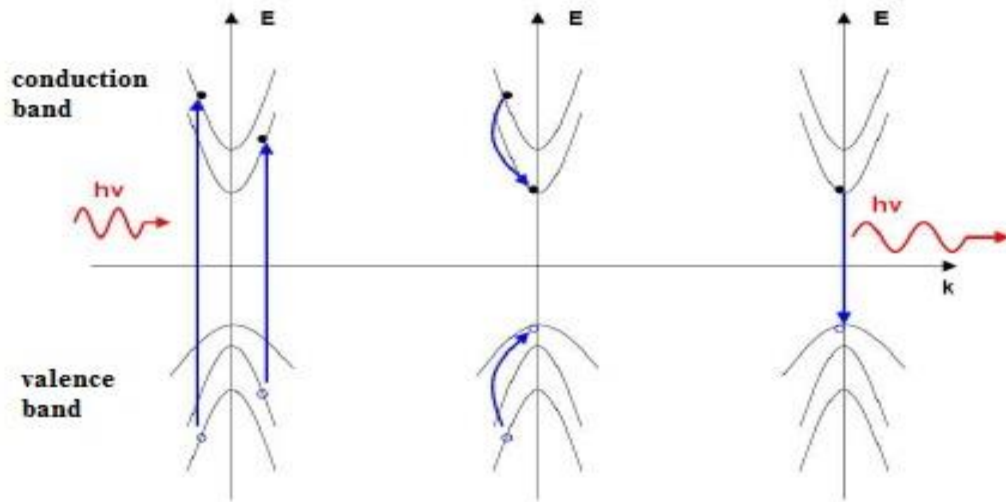


Figure 16: The three distinct stages of photoluminescence in a semiconductor.

In a solid material, the recombination energy is essentially equal to energy gap minus the formation energy of an exciton. The formation energy of exciton created by Coulomb interaction between electron and hole. An electron stimulated from the valence band to the conduction band by absorption of a photon, leaving behind a hole. The electron and the hole relax without emission until both of them reach at the end of the bands. Finally, we have emission of a photon after the recombination of electron and hole [38].

The spectrum of PL in semiconductors can give much information about their physical properties and the behavior of charged carriers (band gap energy, defect levels). Moreover, PL also has the advantage that is non-destructive to the materials. In the simplest set up, PL spectroscopy contains an excitation source (laser) and a collector to gather the radiation signal, usually containing an optical sensor mounted on a monochromator [25].

The temperature of the sample can affect the emission spectra due to the involvement of phonon and the quantization of lattice vibrations. The effect of temperature contributes significantly at cryogenics conditions. Cryostats have been developed to satisfy the needs of different temperatures ranges. The cryostat uses liquid cryogens such as liquid nitrogen or helium to flow over the sample stage, which pass no vibration to the sample [25].

I.2.5 Micro-Photoluminescence spectroscopy of monolayer WS_2

Transition metal dichalcogenides (TMD) include many outstanding optical characteristics such as a clear band gap with direct optical transition, spin-valley coupling, and stable exciton and trion (charged exciton) states. An exciton is a bound state formed by an excited electron and hole owing to the Coulomb attraction between these two quasiparticles. Such bound state plays an important role in the optical properties of low dimensional materials owing to their strong spatial confinement and reduced screening effect compared to bulk solids [40]. One of the major features of monolayer WS_2 is the large exciton binding energy of $\sim 400\text{meV}$ making exciton stable even at room temperature. According to the separation of electron and hole (binding energy), excitons are classified to two limiting cases: the Frenkel and Wannier excitons. The Frenkel excitons have large binding energy, larger than 100meV , that exists in insulators or organic crystals where the electron and hole pairs are confined in one unit cell. A greater direct energy gap of semiconductor has a greater exciton binding energy. Exciton emission play a key role in the PL spectra of WS_2 , especially at low cryogenic temperature (78K) where the PL is dominated by the emission of sharp neutral exciton. The n-type conductivity of WS_2 meaning the existence of an excess concentration of donor, which provides an electron and owes its nature to the gaps created by sulfur atoms.

Our samples are WS_2 monolayers directly exfoliated on SiO_2/Si substrates. The optical response, namely the strong PL of a single layer tungsten disulfide is generally attributed to the strong excitonic effect due to quantum confinement. The broken inversion symmetry in 2D materials lead to the spin-orbit splitting in valence band which shows two prominent spectral features [41]. The optical spectrum is characterized by the presence of two-low energy exciton peaks, known as A and B excitons, that arise from vertical transitions from a spin-orbit-split valence band to a doubly degenerate conduction band at the K point of the Brillouin zone [42]. The A exciton represents the transition from conduction band to the top of valence band at K point while B exciton is the transition from conduction band to the lower band edge due spin-orbit splitting. The separation of A and B excitons is approximately $0,4\text{eV}$. The physics of excitons in 2D semiconductors is known to be extremely rich once additional carriers are introduced into the system [43].

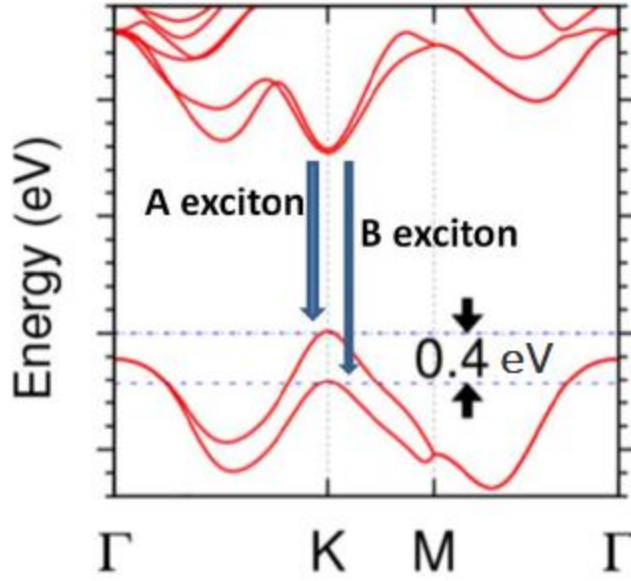


Figure 17: Schematic illustration of the A and B exciton transition in WS_2 monolayer.

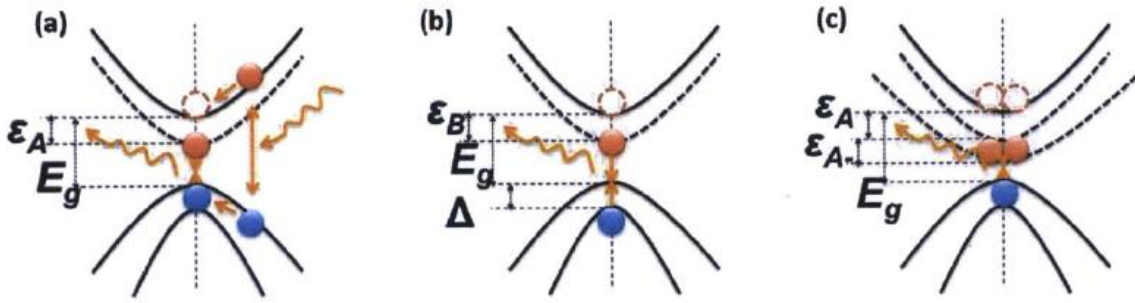


Figure 18: Schematics of the exciton-related transitions, including (a) the A exciton, (b) the B exciton and (c) the A^- trion, at the K point of Brillouin zone. E_g , Δ , ϵ_A , ϵ_B , ϵ_{A^-} denote the band gap, valence band splitting, binding energy of the A, B exciton and A^- trion, respectively [13].

The optical spectra which we will study in this thesis, consist of emission from both neutral (X) and charged exciton (X^\pm). More specifically the negatively charged trion (X^-). To avoid confusion, hereinafter we call the A exciton as neutral exciton (X) and A^- trion as charged exciton (X^-). The dissociation energy of the charged exciton, in exfoliated dichalcogenides semiconductors is greater, by an order of magnitude, than an ordinary semiconductor. Strong emission around $\sim 2.1\text{eV}$ which corresponds well with the predicted recombination of the neutral exciton across the direct gap of single layer WS_2 . A second emission line, on the low energy side of the neutral exciton emission represents the charged exciton ($\sim 2.04\text{eV}$). The neutral exciton is the ground state of a charged neutral system. The low energy line refers to emission from charged excitons (trions) which we presume to be negatively charged given the

n-type nature of the bulk crystal. The observation of X^- requires the presence of excess electrons in the conduction band. We must note that, these numbers of peaks are observed at 78K.

The line of the spectrum becomes much stronger as the excitation power is increased. This line has all the characteristics of a trion: with increasing excitation power, the intensity increases linearly. The binding energy varies linearly, while the ratio of the trion and neutral exciton emission intensity is not constant. The two peaks correspond to the emissions from the direct bandgap at K and K' valleys in the Brillouin zone, consistent with the absorption peaks in the reflectance spectrum. We can tune the ratio between the trion and exciton emission, by changing the intensity of the laser excitation, which demonstrates our ability to tune the density of 2D carriers with light [44].

The difference ΔE , between the emission energy of X and X^- , is the dissociation energy of the trion which is presented in Fig. 19 (a). The trion dissociation energy could be tuned over a small range by varying the power of the 532nm excitation. This dissociation energy grows linearly with the excitation power suggesting that the density of the carriers also grow linearly with the laser power. The difference in the energy can be expressed as the sum of the binding energy and Fermi energy ($E_{X^-} + E_F$). Here binding energy is defined as the dissociation energy in the limit of small doping ($E_F = 0$) where E_X is the energy needed to promote one electron from the trion to the bottom of the conduction band. Data is shown for two different monolayers (flake 1, flake 2). The Fermi energy increases with increasing power of illumination (photon flux) due to the photo-ionization of donors. The trion dissociation energy (Fermi energy) increases more rapidly with laser power in flake 2 suggesting a larger concentration of donors in this flake [44].

The increase of intensity is not the same for the neutral and the charged exciton. The Fig. 19 (b) illustrates this difference. The exciton/trion intensity ratio is plotted as a function of laser power. For both flakes the ratio of the integrated intensities decreases with the excitation power by a factor greater than 2. This is due to the increased probability of the creation of the trion by increasing the density of the photo-ionized carriers. The decrease of the intensity ratio is much faster for the second flake as we can see directly in the spectra in Fig 19 (b), where the trion intensity is rapidly becoming stronger by increasing the excitation power. The increased sensitivity to laser power is consistent with a larger density of donor impurities in flake 2 [25].

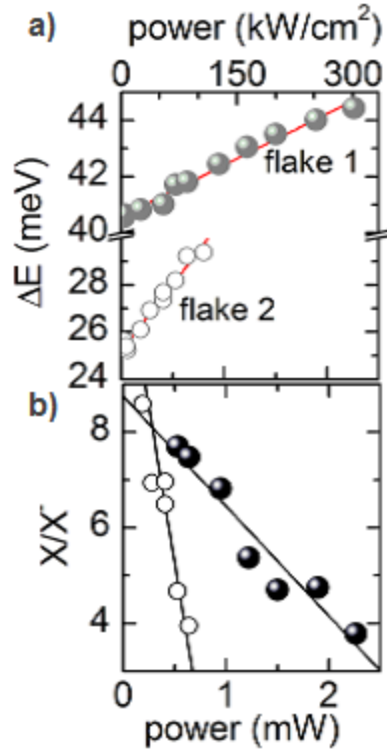


Figure 19: a) The difference ΔE , between the emission energy of X and X^- as a function of excitation power b) the ratio of integrated intensity of the charged and the neutral exciton as function of excitation power [44].

The PL of WS_2 has a strong dependence on temperature. For excitonic emissions, all have the trend to red shift with the increase of temperature. The intensity of charged and neutral exciton emissions sharply decreases with elevated temperature. Due to small binding energy and thermal motion, we have as a result a decrease of intensity in two peaks. There is an expression for the temperature dependence of a semiconductor bandgap. The formula we present here expresses the exciton emission energy as a function of temperature. We use a three parameter fit to the temperature dependence of semiconductor band gaps. This fitting improves upon the semi-empirical Varshni equation both numerically, since it gives better fits to the data, and theoretically, since the parameters of the fit may be related to an intrinsic interaction of semiconductors, namely the electron-phonon coupling. We aim simply to describe the data as well as possible with the minimum number of free parameters. The Varshni relation for the temperature dependence of semiconductor band gaps is:

$$E_g(T) = E_0 - aT^2/(T + b) \quad (11)$$

where E_0 is the ground state transition energy at zero temperature, a and b are fitting parameters characteristic of a given material. The theoretical basis of this much-used relation, is unfortunately rather weak, since b , which is supposed to be related to the Debye temperature, may in certain important cases be negative [45].

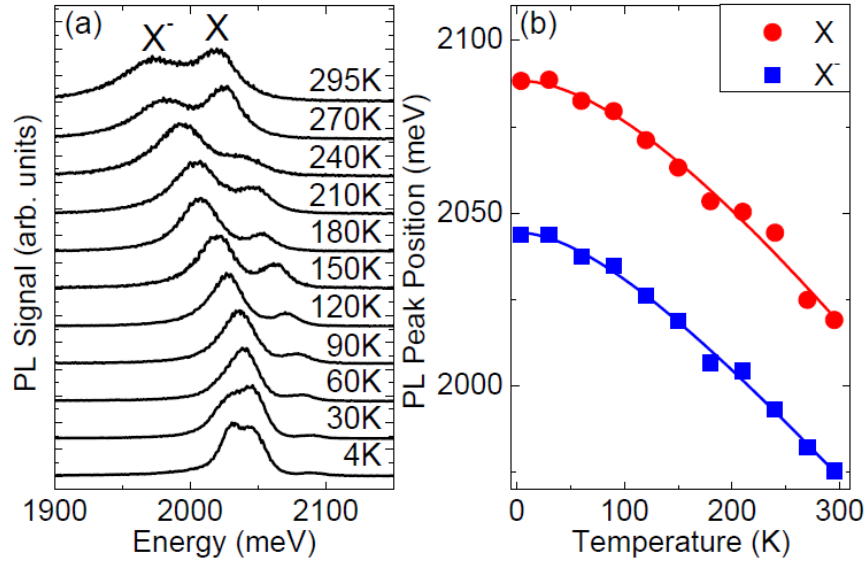


Figure 20: a) Typical normalized micro-PL spectra of single-layer WS₂ for different temperature. b) Exciton (red) and trion (blue) peak position versus temperature with fits. The solid lines represent the fits to the experimental data following Varshni equation [46].

The temperature dependence of the emission is presented in Fig 20 (a). Both exciton lines red shift as the temperature increases. The energy of the emission, obtained by fitting Gaussian, as a function of the temperature is presented in Fig 20 (b). The observed exciton states show fine features consistent with 2D excitons, such as temperature dependence line shape, peak energy of X^0 and X , which further supports the excitonic nature of this monolayer system. As the temperature rises, we see that the X^- intensity drop significantly, which we attribute to electrons escaping their bound trion state due to thermal fluctuations [47].

Above bandgap photoexcitation creates electrons and holes in the conduction bands and valence bands, respectively. If the screening is weak enough, the attractive Coulomb interaction between one electron and one hole creates a bound quasi particle known as neutral exciton (X^0) which has an energy structure similar to a neutral hydrogen atom. Excitons can further become charged by binding an additional electron (X^-) or hole to form charged three-body excitons analogous to H^- or H_2^+ , respectively. These exciton species are elementary quasi-particles describing the electronic response to optical excitation in solids and are integral to many optoelectronics applications [48].

We use mechanical exfoliation to obtain monolayer WS_2 on 290nm SiO_2 , on n^+ doped Si and atomic force microscopy to identify the layer thickness. Monolayer thickness of $\sim 0,7nm$ is identified.

The presence of A and B exciton has been attributed to spin-orbit coupling-induced valence band splitting in bulk. The highest energy emission at $2,1eV$ is the neutral exciton X^0 , and the lower energy peak is a trion.



Photoluminescence spectroscopy was used to characterize the optical band structure of WS_2 thin films. The thinnest sample exhibited the strongest photoluminescence while the intensity decreased with increasing film thickness.

As mentioned, intense light emission is another optical signature of WS_2 monolayers due to the nature of direct bandgap, and thus can be employed as another identifying tool for monolayers. PL mapping obviously yields more information regarding the uniformity of the monolayer region. As a result of large exciton binding energy, the PL emission at 78K and room temperature ($T=295K$) should be still of excitonic nature. However, the broad PL band may consist of both free exciton emission and defect bound exciton emission. Meanwhile, some defects may act as “PL kill centers” that offer various non-radiative channels causing the overall PL intensity drop. The central region of the monolayer shows a relatively much weaker PL intensity compared with its edge regions [49].

I.2.6 Identification of biexcitons in single-layer WS_2

In this chapter, we will study the presence of biexcitons in single-layer WS_2 through the discovery of a sharp new emission peak under laser excitations. At lower photon energies, we see additional emission features, which we label as $L_1/_{XX}$ to L_3 . Features L_1 to L_3 grow more slowly than exciton emission with increasing pump fluence. We assign L_1 to L_3 to emission from bound excitons at defect sites, in agreement with previous PL studies [50].

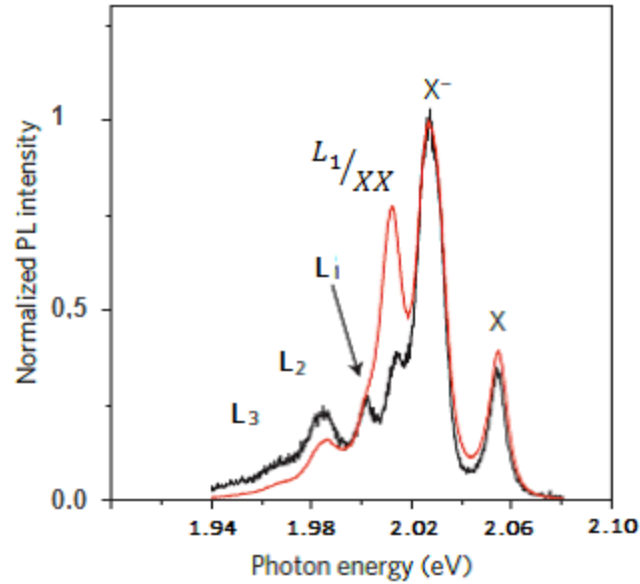


Figure 21: Normalized PL spectra with all the characteristic peaks we would expect to observe to a spectra of single-layer WS_2 . Different colors represent different fluences. Red line has higher fluence than black line [50].

The behavior of peak $L_1/_{XX}$ at 2.25eV (at low temperature) is different from that of the other low-energy features. This feature grows superlinearly with fluence. To minimize the influence of defect states we analyzed the emission intensity $I_{L_1/_{XX}}$ of the $L_1/_{XX}$ species as a function of the emission of intensity I_X of the neutral exciton. The $L_1/_{XX}$ data can be described by a power law relation of the form $L_1/_{XX} \propto I_X^b$, with $b=1.4$. The emission times of X , X^- , $L_1/_{XX}$ show no significant variation with fluence.

On the basis of the superlinear strength of emission from the $L_1/_{XX}$ species with respect to X emission, we identify this feature as arising from a biexciton (XX) state. Under the conditions of full thermal equilibrium (constant temperature as excitation fluences increased)

we would expect a quadratic relation between the density of biexcitons and excitons that is $I_{XX} \propto I_X^b$, with $b=2$.

Tobias Korn and his scientific group, at University of Regensburg in Germany, report a work on low-temperature PL of mechanically exfoliated single-layer WS_2 . To date, only a few works exist which report on the observation of excitons and trions in the low-temperature PL spectrum. We focus on the low-energy feature labeled as L_1/XX . Fig. 22 (a) shows the PL spectra at $T=4K$ for different excitation power. Whereas, at low powers, X^- and L_1/XX are spectrally well separated and of similar intensity, at higher excitation powers, the L_1/XX peak completely dominates the spectrum. A second low-energy peak L_2 with moderate intensity is around $1.98eV$. It may stem from defect-bound excitons, as its intensity decreases relative to the other peaks with increasing excitation density. To get a better insight into the nature of L_1/XX , we can observe Fig. 22 (b). The integrated PL intensity for L_1/XX , X^- and X for different excitation densities, is displayed in the double-logarithmic graph [46].

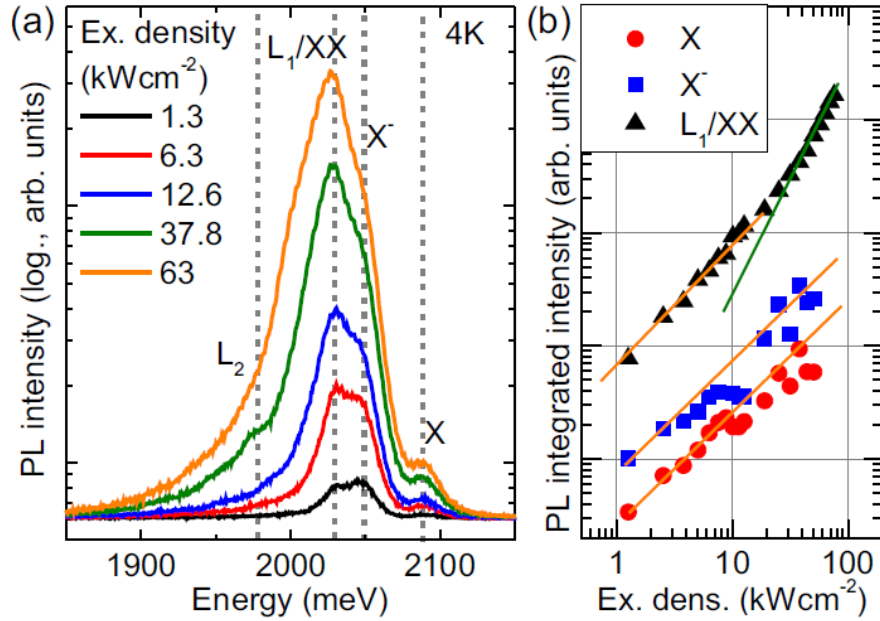


Figure 22: (a) PL spectra of single-layer WS_2 at $T = 4K$ for various excitation densities. (b) Double-logarithmic plot of integrated PL intensity of X (red circles), X^- (blue squares) and L_1/XX peak (black triangles) as a function of excitation density. The orange solid lines indicate a linear dependency, the green solid lines indicate a quadratic dependency [46].

The peaks X and X^- show a rather linear behavior indicated by the orange solid line, as expected for an excitonic feature. In contrast, the L_1/XX peak exhibits a linear dependence at

low excitation density, while for excitation densities larger than 25 kW/cm^2 the data is well described by a quadratic fit indicated by the green solid line in Fig. 22 (b). The different behavior for low and high excitation densities indicates that in fact, two different emission lines are responsible for the observed L_1/XX peak: at low excitation density, the main contribution to the PL at the L_1/XX peak position stems from defect-bound excitons (L_1). At high excitation density, the biexciton (XX) emission is dominant.

As shown in Fig. 23 the L_1/XX peak redshifts by about 10 meV in the investigated excitation density range. This indicates that the L_1 emission from defect-bound excitons at low excitation density is at a higher energy than the biexciton emission at high excitation density. Local heating induced by the laser as a source of the redshift for the L_1/XX , since neither X^- or X peaks show a slight blueshift [46].

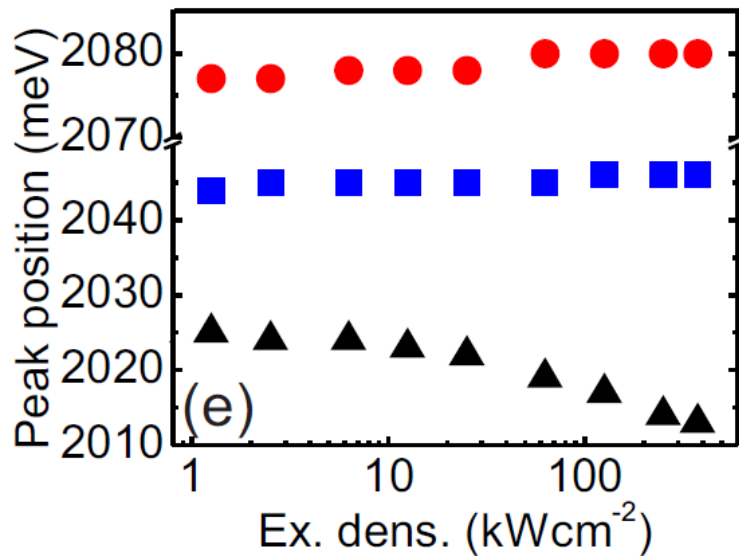


Figure 23: PL peak position for X , X^- and L_1/XX peaks as a function of excitation density [46].

To obtain deeper physical insight into the biexciton state, Fig. 24 (a) represents the four-particle states. Although, biexciton states are a part of transition metal dichalcogenides (TMDC). A monolayer of these materials has a distinctive character of the electron-hole interaction (e-h). Strongly inhomogeneous dielectric environment gives rise to a non-local screening effect for the e-h interaction potential. The screening is strong at a short range, but weak at a long range. The nature of biexciton state consists of two distinct excitons, each with a Bohr radius equal to that of a single exciton (1 nm), separated by a distance three times larger

(Fig. 24 (b)). Given the large separation between charges, the screening of the Coulomb interaction will be strongly influenced by external media, rather than the intrinsic screening of the WS_2 monolayer. We expect the biexciton states to be particularly sensitive to the nature of the surrounding media [50].

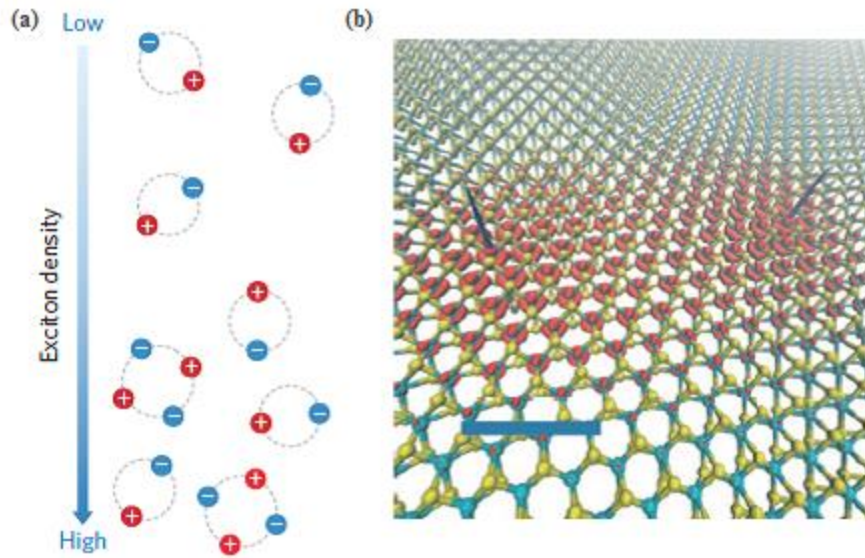


Figure 24: Real-space representation of biexcitons. (a) Biexcitons as four-body quasiparticles. With increasing exciton density biexcitons are formed from excitons. (b) Biexcitons onto the WS_2 plane. The red regions indicate distribution of the total charge of the two electrons in the biexciton when the two holes (blue peaks) are fixed at a typical separation of 3.3 nm (the scale bar is 1 nm) [50].

I.3 Chemical doping of monolayer WS_2

The transition metal dichalcogenides exhibit a wide range of electronic, optical, mechanical, chemical and thermal properties. A certain topic of doping is discussed in more detail here. The richness in the electronic properties of two dimensional transition metal dichalcogenides makes them an ideal platform for a multitude of applications. There is an ability to control the doping of semiconducting 2D layered materials to selectively form p- and n-type regions. After theoretical calculations a scientific group started their study by calculating the displacement threshold energy T_d (the minimum initial kinetic energy of the recoil atom) for sputtering an atom from the material. An initial velocity was assigned to the recoil atom (corresponding to the instantaneous momentum transfer from the electron to the atom during the impact). After proving that vacancies can be created in TMDs, under electron irradiation, they calculated the formation energy of substitutional defects on MoS_2 . They listed the formation energies with different potentials of the isolated atoms. So the candidate dopants, which can fill the vacancy of an S atom are the following: F, Cl, Br, N, P, As, I [51].

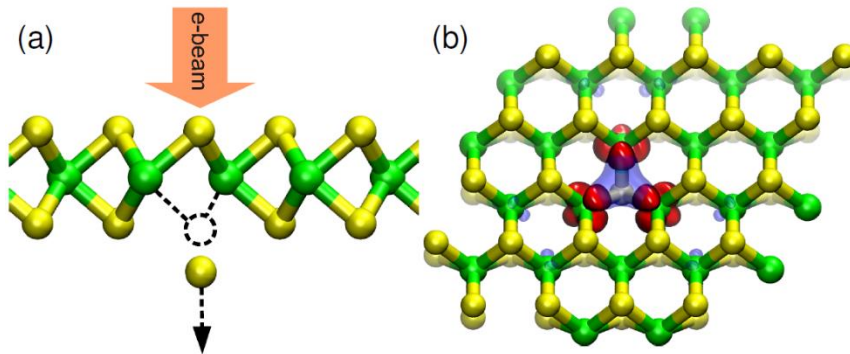


Figure 25: A simulation of atom sputtering from tungsten disulfide under electron irradiation [51].

In practice, the initial kinetic energy of the recoil atom was increased until it was high enough for the atom to be displaced from the lattice site without an immediate recombination with the resulting vacancy.

T_d was required for displacing a chalcogen atom from the bottom layer of the sheet. The vacancy formation energy can be defined as:

$$E_f = E_{vac} - (E_{bulk} - \mu_\chi) \quad (13)$$

where E_{bulk} and E_{vac} are the energies of the pristine and vacancy containing supercells, respectively. The chemical potential μ_χ of the chalcogen species is taken as the energy of an isolated atom to enable a straightforward comparison with the results of dynamical simulations.

The dependence of trion and exciton emission on chemical doping are investigated in single-layer WS_2 by micro-PL measurements, where different responses are observed. The total PL is strongly influenced when electron-withdrawing molecules adsorb on monolayer WS_2 . The electrical transport data suggest that the exfoliated monolayer WS_2 is naturally n-type semiconductor and clearly delineates that the electron concentration decreases when the electron-withdrawing dopant interacts with WS_2 [52]. Note that B exciton feature is not measured under $532nm$ ($2.33eV$) laser excitation, which we use for our micro-PL measurements, in this thesis. The PL spectra under successive doping shows that the X^- and X emission changes differently with doping. The X is influenced, while the X^- is nearly unchanged [52].

As known, in a typical micro-Raman spectra of monolayer WS_2 , the out of plane A_{1g} mode is susceptible to the changing effect and red shift with electron doping, but the in-plane E_{2g}^1 is not affected by the doping effect, which is due to the strong electron-phonon coupling with the out of plane mode. On the contrary, the E_{2g}^1 mode has been shown to be sensitive to strain and red shifted with the increase of both uniaxial and biaxial strain, while the A_{1g} mode remains unchanged [52]. Our experiments depend on photochemical doping with chlorine and nitrogen. In chapter II, we will discuss about the interaction between chlorine and nitrogen atoms with monolayer WS_2 .

I.4 Experimental methods

This chapter provides a description of some fabrication tools used in this work. Measurement and imaging used for evaluation of experimental work.

I.4.1 Preparation of single-layered and multilayered WS_2 nanosheets by micromechanical exfoliation

There are many methods to prepare nanosheets of WS_2 including mechanical exfoliation, chemical vapor deposition and sonication. Mechanical exfoliation is the most efficient way to produce nanosheets of transition metal dichalcogenides, because with this method we can produce the cleanest, highly crystalline and atomically thin nanosheets. The most common class of crystalline structures that can be exfoliated to stable single layers are the layered van der Waals solids. These structures are covalently or ionically connected with their neighbors within each layer, whereas the layers are held together via van der Waals forces along the third axis. The energies of van der Waals are weak ($40 - 100meV$), so the exfoliation can be take place. The first step, in this method, is to extract the crystal from the main part, by using adhesive scotch tape. A small piece of the bulk crystal WS_2 is being put on the sticky side of a piece of adhesive tape. This is followed by repeated folding and unfolding of the tape to produce thin flakes. The tape is then pressed onto a silicon substrate covered by a $290nm$ thick SiO_2 layer [7].

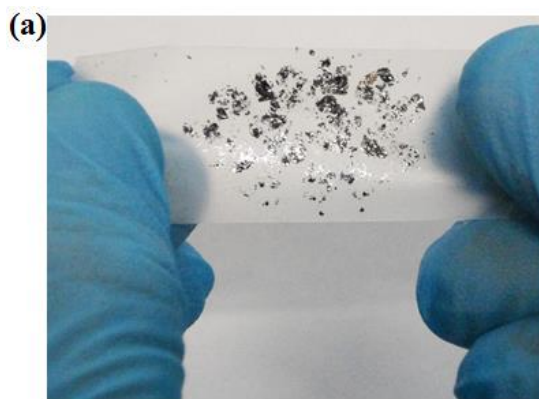


Figure 26: (a) WS_2 can be mechanically exfoliated using scotch tape to create monolayer samples, similarly to graphene [53]

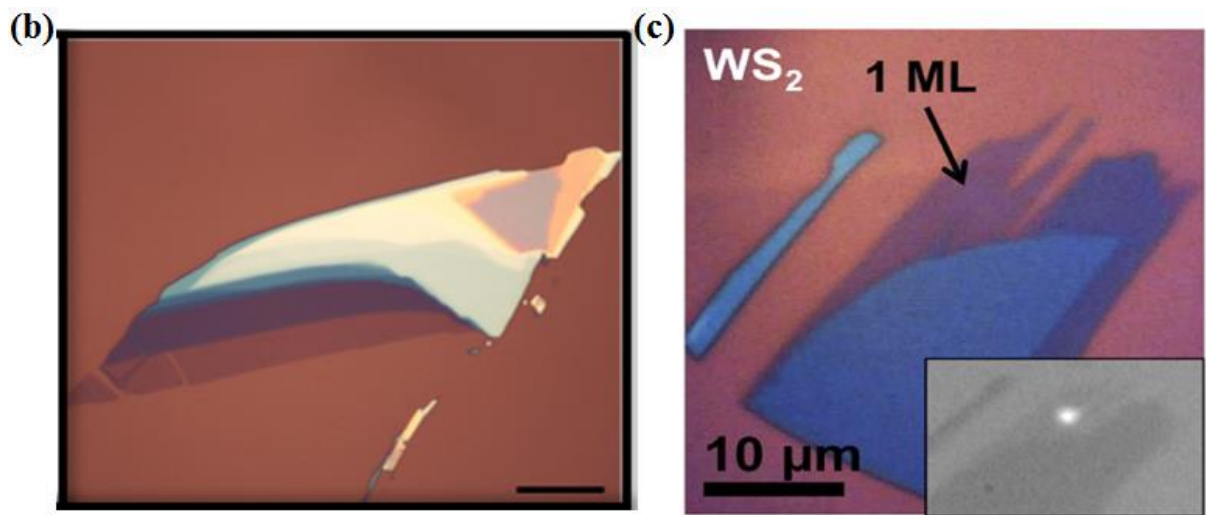


Figure 26: (b), (c) optical microscope images of representative WS_2 monolayer flakes [54].

The tape is then removed from the substrate, leaving behind some atomically thin WS_2 flakes. We can use optical microscope for optical identification of single-layer and multilayered WS_2 nanosheets that are randomly located on the substrate. A wide variety of thin and thick WS_2 flakes can be identified by the optical contrast between the material and the oxidized substrate. Single-layer can be isolated with this method and it appears with a light purple color on a 290nm SiO_2/Si substrate. This type of substrate provides a high optical visibility of single-layers. The size of the flakes is in the order of 1 to $10\mu m$ [7]. Nevertheless, this method is not appropriate for practical applications on a large scale because it is not possible to control the size and the thickness of the produced flakes. Raman spectroscopy is extensively used in the literature to identify monolayer sample regions [55].

I.4.2 Experimental set up of Raman spectrometer

In a typical setup, a laser beam is aligned to interact with the specimen and the scattered photons are collected to measure the shifts in energy caused by inelastic scattering. The Thermo Scientific, Nicolet Almega XR Micro Raman analysis system used in this work allows both microscope and macro imaging with microscope magnification up to 100x [56]. A diode-pumped solid-state laser (473nm), with maximum output of $50\mu W$ was focused on the objective lens on an optical microscope attached with the Raman spectrometer [57].

A typical Raman spectrometer is composed of: a laser a microscope and a spectrometer. A schematic overview of the setup is presented in Fig. 27.

The laser passes through a beam splitter and is focused on the sample with a microscope objective lens. Then, the back scattering light is guided to the analyser through a combination of optics elements, which register the spectrum of scattered light. As the laser enters the sample, elastic and inelastic scattering occurs. A filter cuts out the Rayleigh emission. A lens focuses the beam on a slit aperture which cuts out the rays coming from other layers of the sample. The beam is diffracted by a high resolution grating (2400 lines/mm), which analyses the signal. The CCD sensor converts the incoming photons into an electrical signal. The result from the software is a spectrum with a number of counts assigned to each resolvable energy [57].

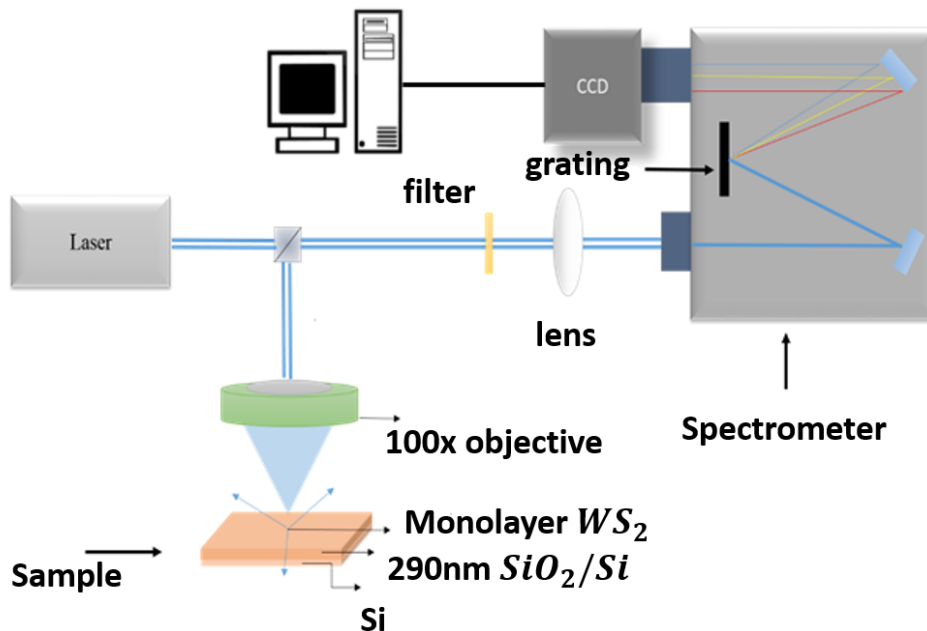


Figure 27: Schematic of the set up used for the Raman Micro-Spectroscopy measurements.

I.4.3 Experimental set up of photoluminescence spectrometer

The experimental setup includes:

- a) the optical path for the orientation of excitation beam and collection the emitted radiation of the samples.
- b) the measuring system for the collection and analysis of signal.
- c) the cryostat. For the measurements the sample is placed in an optical cryostat. It is mounted on motorized x-y translation stages.

The sample is illuminated by a diode pumped solid state laser (DPSS) emitting at $532nm$, Nd: Yag. It is a continuous wave laser which was used as an excitation source. The photon energy is $2.33eV$ and the average output power is $19.9mWatt$. The energy of the beam was controlled via a combination of a waveplate, a linear polarizer and a series of neutral density filters, while the polarization direction was controlled via a $\lambda/2$ waveplate. The sample is placed inside a cryostat which permits experiments at very low ($T = 79K$) and room temperature ($T = 295K$) as well as vacuum ($< 0.2Pa$ or $2 \times 10^{-6}bar$) conditions.

The reflected beam from the sample is passing through a lens with focal length of $40mm$. This lens collects and leads the emitted radiation at the entrance of the spectrometer. The analysis of the emitted radiation wavelength of the samples takes place in the grating spectrometer and recorded by a digital silicon CCD camera, which is connected to a computer. The micro-PL spectra have been recorded using the spectrometer. The signal analyzed by a $600\textit{grooves}/mm$ grating and detected with a nitrogen-cooled charged couple device camera CCD. Also, the signal was dispersed by a $0,75mm$ spectrograph. Excitation and collection was implemented using an external microscope quartz objective lens 40×0.65 giving a typical spot diameter of $\simeq 1\mu m$, which we can focus on the area of the sample where we want study.

The experimental setup of micro-PL system allows the detailed record of spectrums with maximum analysis via the spectrometer. This is achieved with the focusing of incident radiation on a very small region of the sample and the collection of emitted micro-PL from the corresponding region.

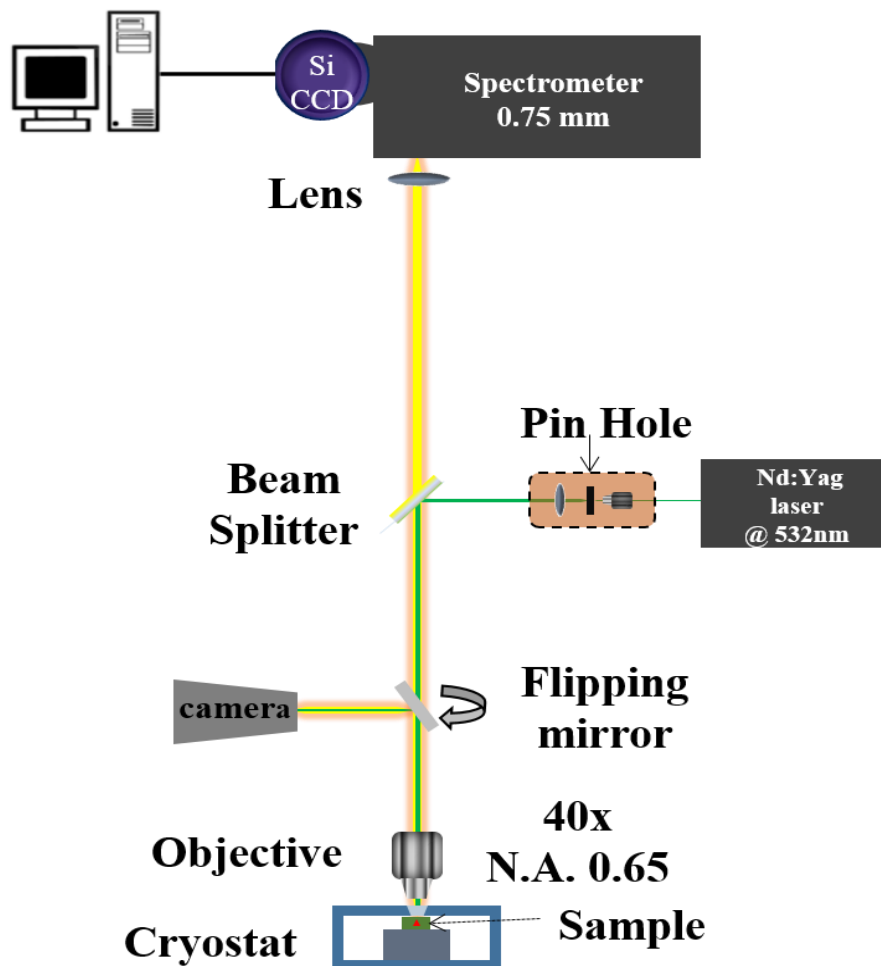


Figure 28: Illustration of the experimental setup for the study of micro-photoluminescence at monolayer WS_2 .

I.4.4 Experimental setup for photochemical doping Tungsten disulfide(WS_2) in chlorine (Cl_2) and nitrogen (NH_3) environment.

This section refers to the enrichment of monolayer tungsten disulfide on substrates SiO_2/Si with chlorine and nitrogen. The laser we use for our irradiations is the KrF excimer laser, 248nm. An excimer laser uses a combination of a noble gas (krypton Kr, argon Ar, or xenon Xe) and a reactive gas (fluorine F or chlorine Cl). Under the necessary electrical impulses and high pressure conditions, a pseudo molecule called “excimer” (excited dimer) is formed. This can exist only in an active state and enables laser irradiation in the ultraviolet range (UV).

In an excimer molecule, laser action can occur because it has a bonding excited state but not repulsive ground state. This is because noble gases such as krypton or xenon are inert gases and often do not form chemical compounds. However, in an excited state (which is affected by a high energy electron beam producing high energy pulses) they can temporarily form bonding molecules with themselves (dimers) or halogens such as fluorine F or chlorine Cl. The stimulated compound can give the excess energy of spontaneous or stimulated emission leading the molecule to a strong repulsive ground state, which rapidly (on the order of picoseconds) is separated into two non-bonding atoms. This process is called population inversion.

A fluoride-krypton (KrF) laser absorbs energy from the source causing the krypton gas to react with the fluorine gas generating the fluoride-krypton, a temporary composite, at an excited energy state.



This composite, with spontaneous or stimulated emission, can reduce its energy state to ground states. The ground state of this composite quickly separates into two non-bonding atoms.



The result is an excimer laser that radiates energy at 248nm, in the near ultraviolet range, which emits radiation. The energy of radiation is the difference between ground and excited state of KrF composite [58].

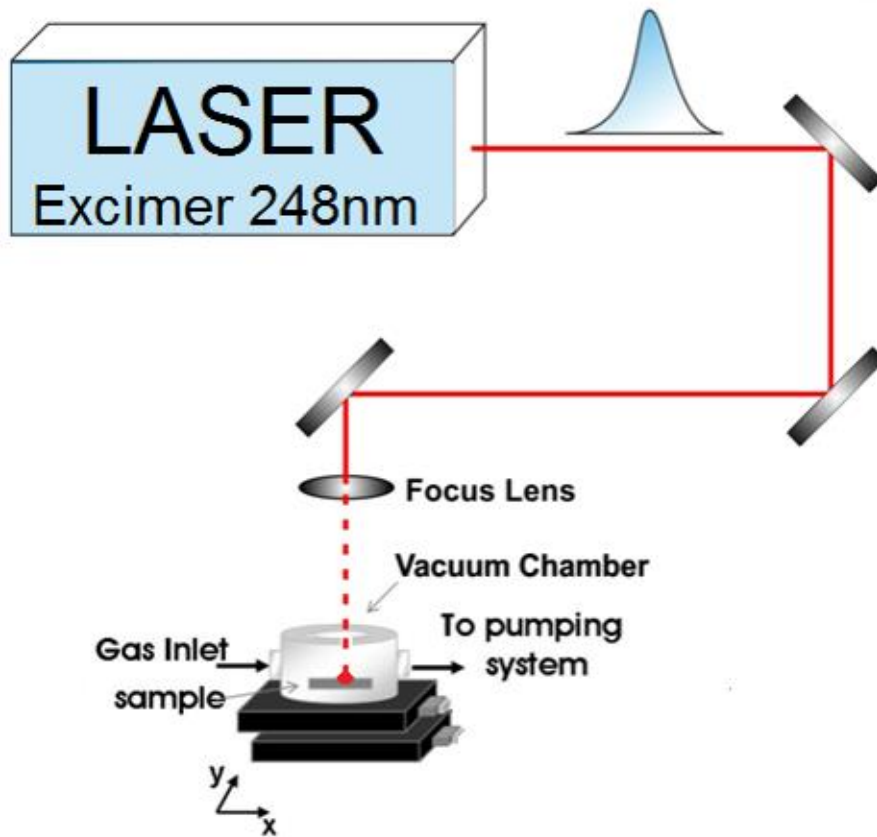


Figure 29: Experimental setup used for doping WS_2 in chlorine or nitrogen environment with KrF excimer laser.

As shown in figure 29, the laser beam impinges on a mirror and then incident on a second mirror. It passes through an iris until it reaches a lens with focal length 20cm, which focuses the laser beam on the sample. The sample is located in a quartz cell. The pulse has repetition rate 10Hz. Adjust the iris so the spot size of laser reaches the cell is about 7cm^2 [58]. We place the sample in the quartz cell and after seal it, we are waiting for low vacuum to be created ($1.3 \cdot 10^{-3}\text{mbar}$). The vacuum pump is connected with the cell and the controller. The controller has a panel which it helps us to see the conditions in the cell. The cell also, is connected with the manometer. The needle of manometer points the depletion and release of helium, before the radiation in quartz cell. The helium gas clean the cell before we radiate the sample with chlorine (Cl_2) or nitrogen (NH_3). The gas pressure of chlorine or nitrogen in the cell is about 150mbar . We irradiate the sample for 6 seconds, so the total number of pulses that the sample accepts is 60. We study the behavior of a representative number of monolayer tungsten disulfide under electron irradiation and calculate the threshold energy for atomic displacements in each system. After some tests, we conclude that the energy damage threshold

for crystal tungsten disulfide on SiO_2/Si is $76mJ$. If the energy overcomes this number, we will notice damage in the regions of crystal who are interested to study. Therefore, the energy ranges from 40 to $76mJ$. With these limits of energy, the fluence respectively range from $5.70^{mJ}/cm^2$ to $10.85^{mJ}/cm^2$.

The formula we use to calculate the fluence is:

$$fluence = \frac{energy}{diameter\ of\ the\ beam} \quad (16)$$

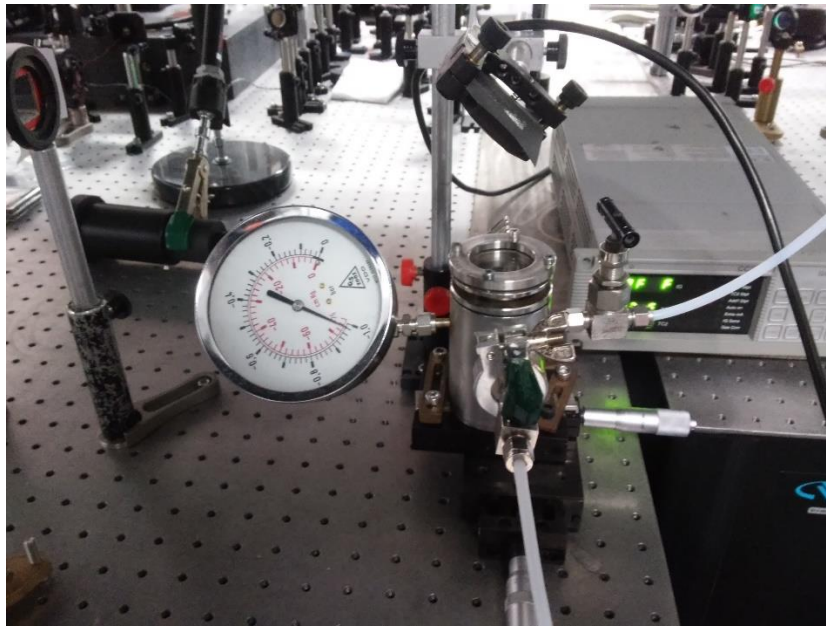


Figure 30: The quartz cell connected with vacuum pump, manometer and controller

II. Experimental results and discussion

This chapter is divided into two sections. The first section refers to doping of WS_2 monolayer which is mounted on SiO_2 substrate, with chlorine (Cl_2) and nitrogen (NH_3). The laser which is used for our irradiation is the KrF excimer laser, $248nm$. The procedure is as follows: the first step is the identification of monolayer region by micro-Raman spectroscopy. We define the pre-irradiated sample as pristine sample. The second step is the characterization of the region through micro-photoluminescence spectroscopy. The third step is the irradiation treatment in chlorine and nitrogen environment. Finally, Raman and micro-photoluminescence spectroscopic techniques are exploited to evaluate the effect of the chemical doping of the samples.

II.1 Sample characterization

Single layer regions with size $\sim 8\mu m$ are identified with an optical microscope and confirmed with micro-Raman (Thermo Scientific, Nicolet Almega XR) spectroscopy at room temperature (300K). Micro-Raman spectroscopy uses the $473nm$ excitation wavelength. In this procedure the laser intensity is kept in low values in order to avoid structural damage of the monolayer region. The energy difference between the two main vibrational modes (i.e. E_{2g}^1 and A_{1g}), is used as the fingerprint of the number of layers [14]. As mentioned in chapter I.2.4, E_{2g}^1 is the in-plane and A_{1g} the out-of-plane vibrational mode whose energy at the monolayer limit is $\sim 357cm^{-1}$ and $\sim 416cm^{-1}$, respectively. Figure 31 shows a typical optical image of flakes obtained by mechanical exfoliation on $290nm$ Silicon oxide. Typical Raman spectra of monolayer at $T=300K$ are shown in Fig. 32. All the Raman spectra presented here, are calibrated on the basis of Si Raman peak at $520cm^{-1}$. The $58cm^{-1}$ energy difference of these two vibrational modes unambiguously confirms the existence of a single-layer WS_2 . The lateral size of the monolayer in Fig. 31 is about $13\mu m$.

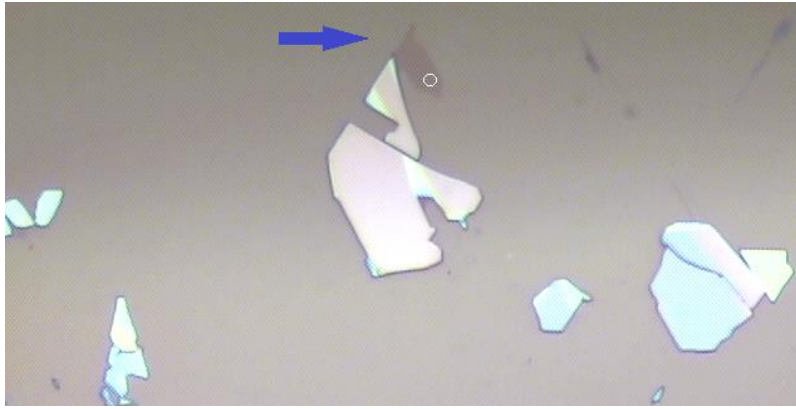


Figure 11: Confocal microscope image of a representative exfoliated WS_2 sample. Arrow indicates monolayer region and white circle indicates approximate optical probe size.

A typical resonant Raman spectrum taken at 300K is presented in Figure 32. Two strong features are observed. A single resonance peak at $415.38cm^{-1}$, which corresponds to the A_{1g} mode in a single-layer of tungsten disulfide, together with a more complicated feature observed around $350cm^{-1}$. It is composed of two features: a peak at $343.54cm^{-1}$ accompanied by a stronger peak $357.044cm^{-1}$ corresponding to the E_{2g}^1 mode in a single-layer WS_2 . The $58.336cm^{-1}$ energy difference between A_{1g} and E_{2g}^1 confirms the single-layer character of the sample. The presence of an additional peak in front of E_{2g}^1 mode has been reported for bulk crystals and very recently for single-layer WS_2 . This peak has been assigned to a second order Raman resonance involving longitudinal acoustic phonons (2LA). The separation between A_{1g} and 2LA is $71.84cm^{-1}$. However the separation between the 2LA and E_{2g}^1 modes is only $13.5cm^{-1}$. This feature involving two LA phonons from the M-point in the Brillouin zone. This LA phonon is similar to that seen in Raman scattering from folded acoustic phonons observed in superlattices. While our measurement is configured in backscattered geometry, the WS_2 monolayer is on SiO_2/Si substrate and therefore some incident light is transmitted through the WS_2 and then is reflected from the silicon substrate and returned in a Raman forward-scattering geometry. This produces a mixed forward and backward scattering result and may contribute to the broadened line shape of the 2LA(M) mode [34].

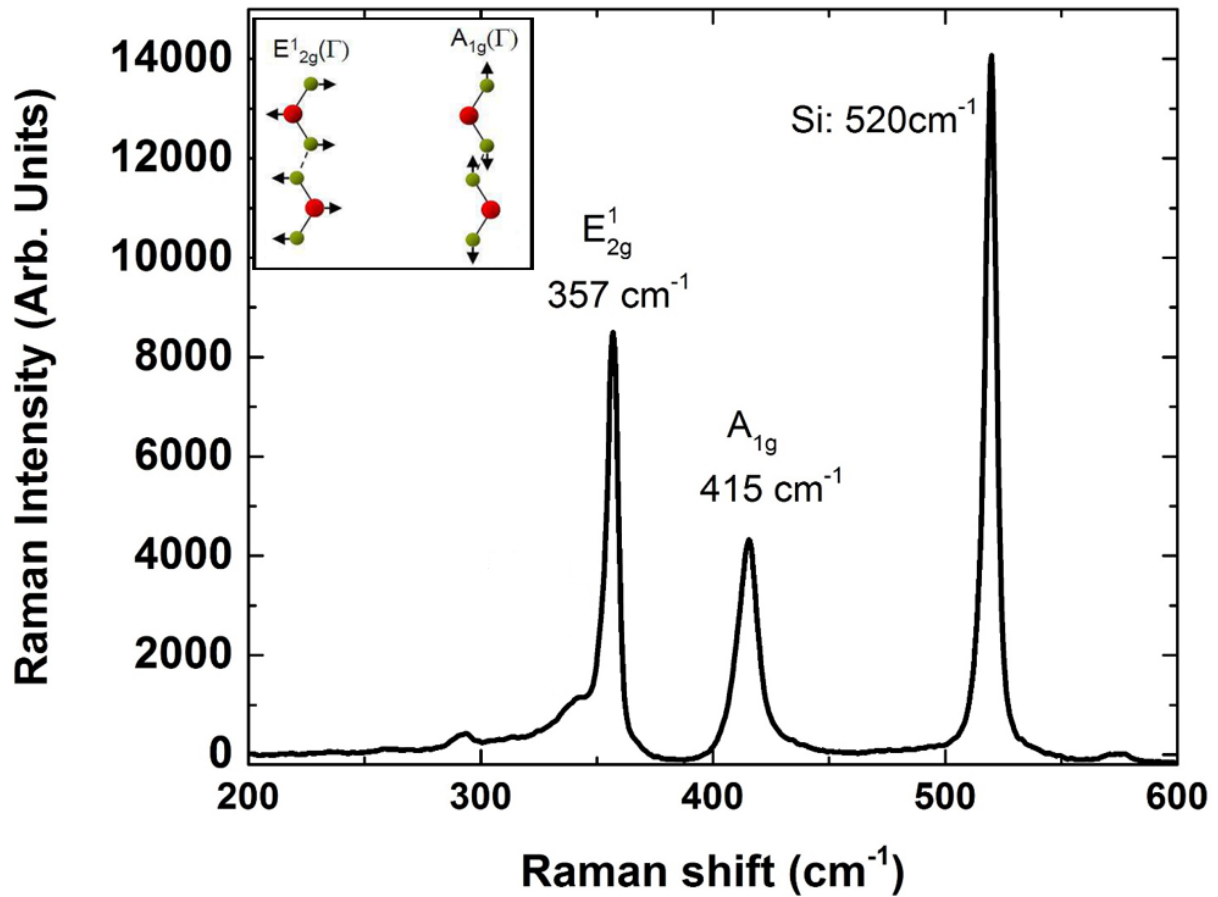


Figure 32: Raman spectra at 300K for monolayer WS₂. The energy separation between the in-plane E_{2g}¹ and out-of-plane A_{1g} is 58cm⁻¹, characteristic of single layer.

Figure 33 shows a typical micro-PL spectrum of monolayer WS₂. The three peaks are located at 2.033eV, 2.048eV and 2.092eV, which represent the biexciton, charged and neutral exciton. The charged exciton (trion) is a recombination state of two electrons and one hole. The trion is denoted by X[±], depended on the sign of the net charges on the quasiparticle.

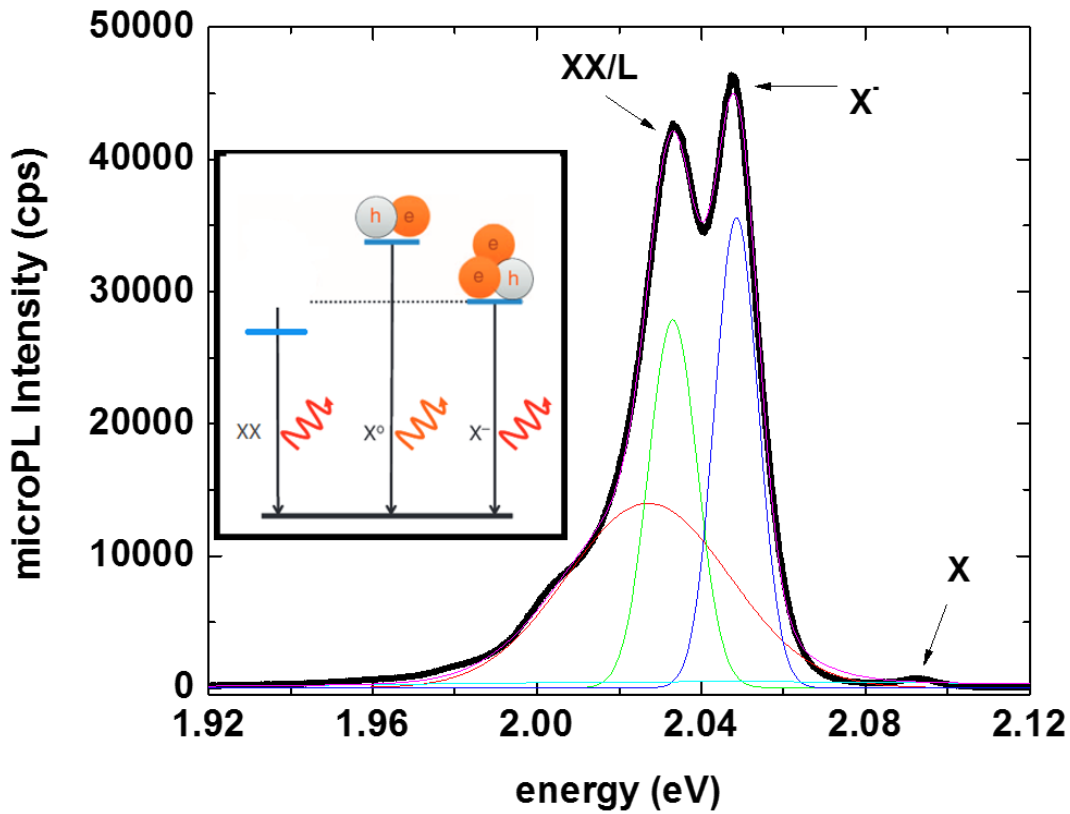


Figure 33: A typical micro-PL spectrum of monolayer WS_2 . The black line is experimental data. The red, green, blue and light blue curves are three fitted Gaussian function profiles and the purple curve is the simulation of the fitted functions.

II.2 Photochemical doping of mechanically exfoliated monolayer WS_2 with Cl_2 and NH_3

As shown in Fig. 29 the laser beam is first reflected by a mirror and then passes through an attenuator, which controls the laser energy. Subsequently, the laser beam hits a second mirror and passes through an iris until it reaches a lens with focal length 20cm , which focuses the laser beam onto the sample. The sample is located in a quartz cell. We change the shape of the beam in addition to become square and approximately 7cm^2 . So, after micro-Raman and micro-PL measurements, we start the radiation with a KrF excimer laser at 46mJ energy and 60 pulses, to achieve a fluence of $6.5\text{mJ}/\text{cm}^2$. The damage threshold of WS_2 is estimated to be about $10\text{mJ}/\text{cm}^2$. The laser has a repetition rate of 10Hz and the irradiation lasts 6 seconds.

Because chlorine is a highly reactive and toxic gas, a trap with liquid nitrogen is necessary. The aim of the operation is to trap the chlorine atoms so they will never reach the

vacuum pump. We always clean the chamber carefully with helium and draw the gas to achieve low-pressure conditions before adding chlorine atoms. The irradiation takes place in a 150mbar chlorine environment. The procedure is the same for the irradiation in rich nitrogen environment.

II.3 Results before and after photochemical doping with Cl_2

In this section we will discuss the results of the chlorine doping of single-layer WS_2 . Raman and micro-PL spectroscopy, was utilized to evaluate the photochemical doping of the single-layer WS_2 with chlorine atoms. Chlorine is considered to be an excellent candidate as a dopant for two dimensional materials. Seven valence electrons are available to form strong valence bonds with sulfur atoms. Our initial and final Raman and micro-PL measurements, shown in charts below.

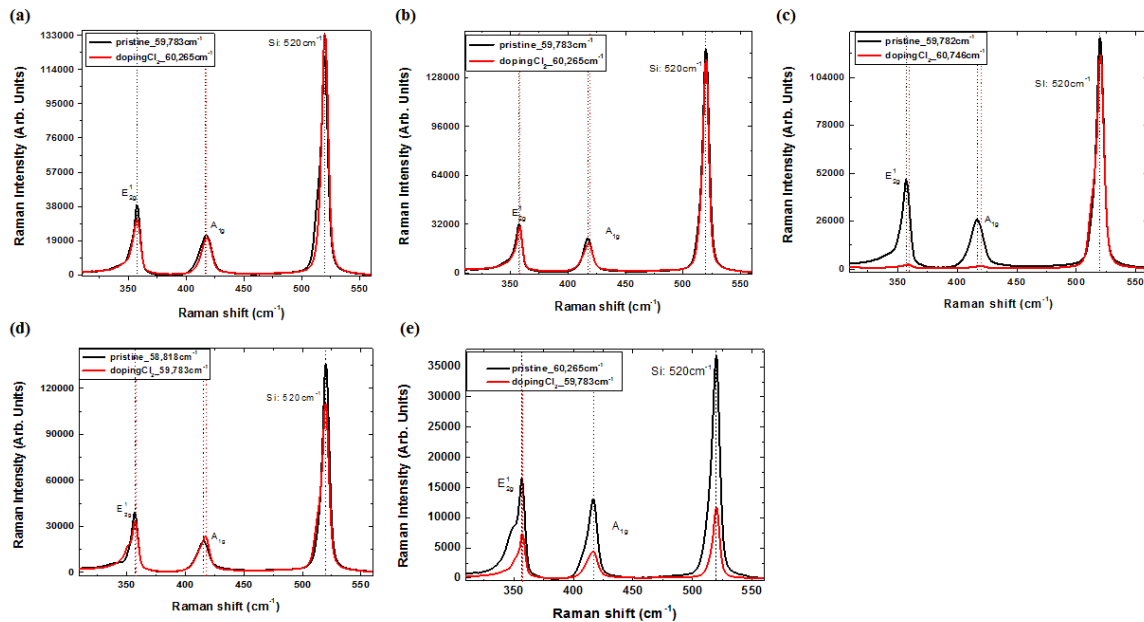


Figure 34: Micro-Raman spectra at $T=300K$ for WS_2 on SiO_2/Si before and after photochemical doping with Cl_2 . Black line for the pristine and red for the irradiated sample. Dot lines show the shift of the peaks. (a) sample 1, (b) sample 2, (c) sample 3, (d) sample 4, (e) sample 5.

Table 1: The following table, the characteristics of Raman peaks E_{2g}^1 , A_{1g} before and after photochemical doping with Cl_2 , are summarized for all the samples. Data refer to peak position, intensity and FWHM.

Samples	E_{2g}^1 (cm^{-1})	Intensity E_{2g}^1 (counts)	FWHM E_{2g}^1 (cm^{-1})	A_{1g} (cm^{-1})	Intensity A_{1g} (counts)	FWHM A_{1g} (cm^{-1})
Before radiation (1)	357.52	29282	5.74	417.30	19820	8.88
After radiation (1)	357.52	25627	7.50	417.79	19345	11.6
Before radiation (2)	357.52	25120	6.20	417.30	20918	10.37
After radiation (2)	358.00	23358	5.91	418.27	17017	11.43
Before radiation (3)	357.04	40228	7.76	416.82	24795	14.24
After radiation (3)	358.97	1470	8.56	419.71	1509	7.06
Before radiation (4)	357.04	33024	6.98	415.86	18452	13.83
After radiation (4)	357.52	22335	5.64	417.30	20975	12.51
Before radiation (5)	356.56	111711	5.20	416.82	117860	9.42
After radiation (5)	357.04	54847	5.94	416.82	42106	12.48

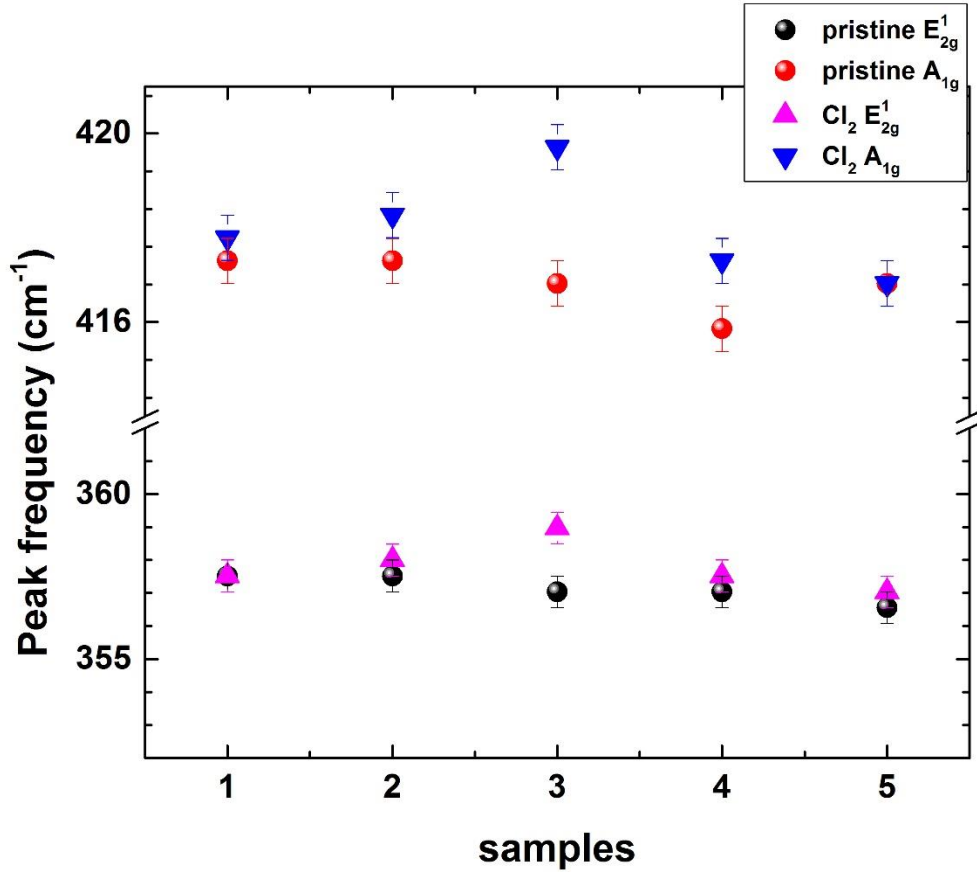


Figure 35: Peak frequencies of the E_{2g}^1 and A_{1g} mode before and after photochemical doping with Cl_2 , for samples 1-5.

Raman spectroscopy has been utilized to evaluate the doping treatment of the WS_2 monolayer, since vibrational energy is renormalized due to electron-phonon interactions [59]. From Fig. 34-35 and after data analysis, it is found that A_{1g} modes blue shift after photochemical doping in chlorine environment. Compared to A_{1g} , the E_{2g}^1 Raman band position is much less affected by the doping, due to stronger electron-phonon coupling of the A_{1g} mode. The strain effect in the chlorine doped monolayer WS_2 is negligible. The adsorption of chlorine molecules reduces the electron concentration in monolayer WS_2 . All the Raman bands show weaker intensities after radiation treatment because of defect introduction to the monolayer WS_2 structure.

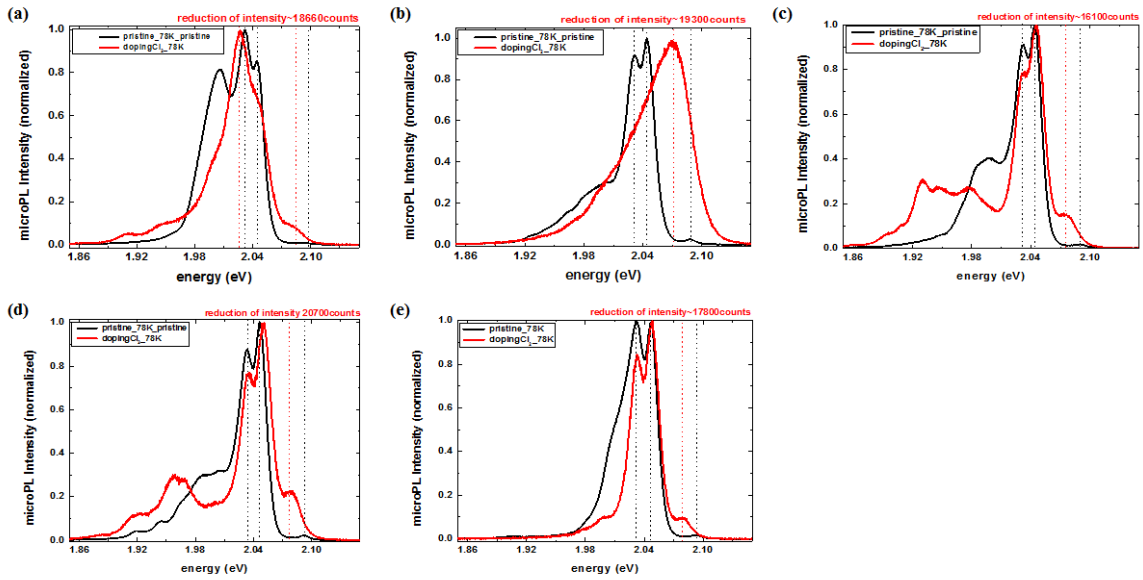


Figure 36: Normalized to intensity micro-PL spectra. Comparison before and after photochemical doping with Cl_2 . The excitation laser wavelength here is 532nm. Measurements were performed at temperature $T=78\text{Kelvin}$. The laser power is 21microWatts, approximately. Black line represents the pristine and red the irradiated sample. Dot lines show the shift of the peaks. Spectrum scope of (a) sample 1, (b) sample 2, (c) sample 3, (d) sample 4, (e) sample 5.

Table 2: In this table, the characteristics of micro-PL peaks XX, X⁻ and X before and after photochemical doping with Cl₂, are summarized for all the samples. Information relate to non-normalized charts and give the values for peak position, intensity and FWHM.

Samples	XX (eV)	Intensity of XX (cps)	FWHM of XX (meV)	X ⁻ (eV)	Intensity of X ⁻ (cps)	FWHM of X ⁻ (meV)	X (eV)	Intensity of X (cps)	FWHM of X ⁻ (meV)
Before radiation (1)	2.031	17500	13	2.045	20700	15	2.091	267	6
After radiation (1)	2.026	2280	19	2.046	2040	23	2.076	287	27
Before radiation (2)	2.031	19400	18	2.044	11502	9	2.087	695	6
After radiation (2)	2.017	65	50	2.046	105	38	2.074	233	37
Before radiation (3)	2.031	19300	18	2.046	20480	13	2.090	480	4
After radiation (3)	2.031	3469	19	2.047	4345	15	2.070	804	33
Before radiation (4)	2.032	18800	17	2.048	22930	12	2.091	660	17
After radiation (4)	2.034	1700	20	2.051	2219	15	2.078	539	27
Before radiation (5)	2.032	11820	13	2.048	19700	12	2.092	416	10
After radiation (5)	2.031	1433	15	2.048	1837	15	2.079	90	17

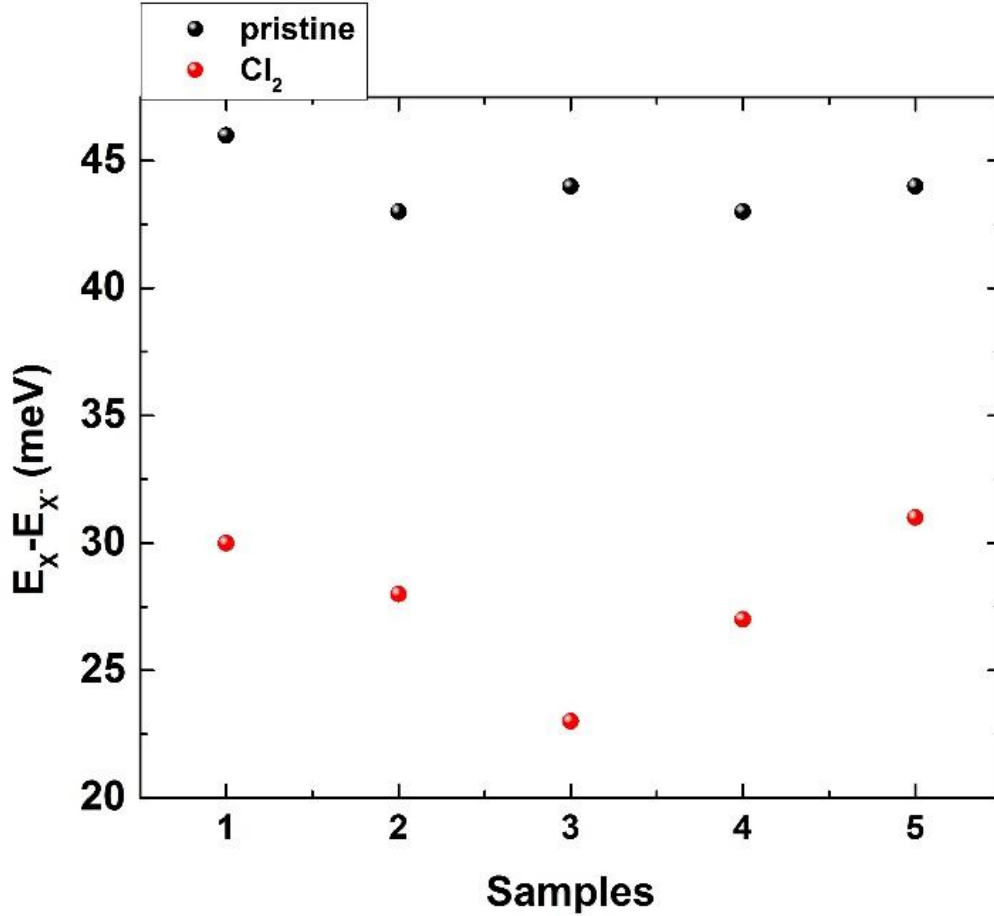


Figure 37: The trion dissociation energy, $\Delta E = E_X - E_{X^-}$, before (black bullets) and after radiation (red bullets) in chlorine environment.

The dependence of trion (X^-) and exciton (X) before and after photochemical doping with Cl_2 is investigated in monolayer WS_2 with micro-PL measurements. Fig. 36 shows the micro-PL spectra and the table 2 sums up the results. The PL spectra in Fig. 36 indicate that the X^- and X emission behave differently with chlorination doping. Specifically, the peak position X^- red shifts after radiation, while that of X^- remain almost unchanged with doping. Clear quenching and red shift of the X exciton peak from the micro-PL spectra is observed. The typical trion dissociation energy, ΔE , defined as the energy difference between X and X^- , is found to be larger before radiation (Fig. 37). The PL intensity is reduced when monolayer WS_2 is covered with dopants. The experimental results can be explained by a Fermi level shift after photochemical doping with Cl_2 . It should be noted that FWHM increases after the radiation.

II.4 Results before and after photochemical doping with NH_3

In this section, we follow the same procedure with section II.3, but here our target is nitrogen enrichment in single-layer WS_2 . Changes of Raman and micro-PL spectra, after radiation in nitrogen environment, would indicate possible nitrogen doping of single-layer WS_2 . Nitrogen is considered to be an excellent candidate for the photochemical doping of two dimensional materials. Five valence electrons are available to form strong valence bonds with sulfur atoms. Micro-Raman and micro-PL spectra are shown below.

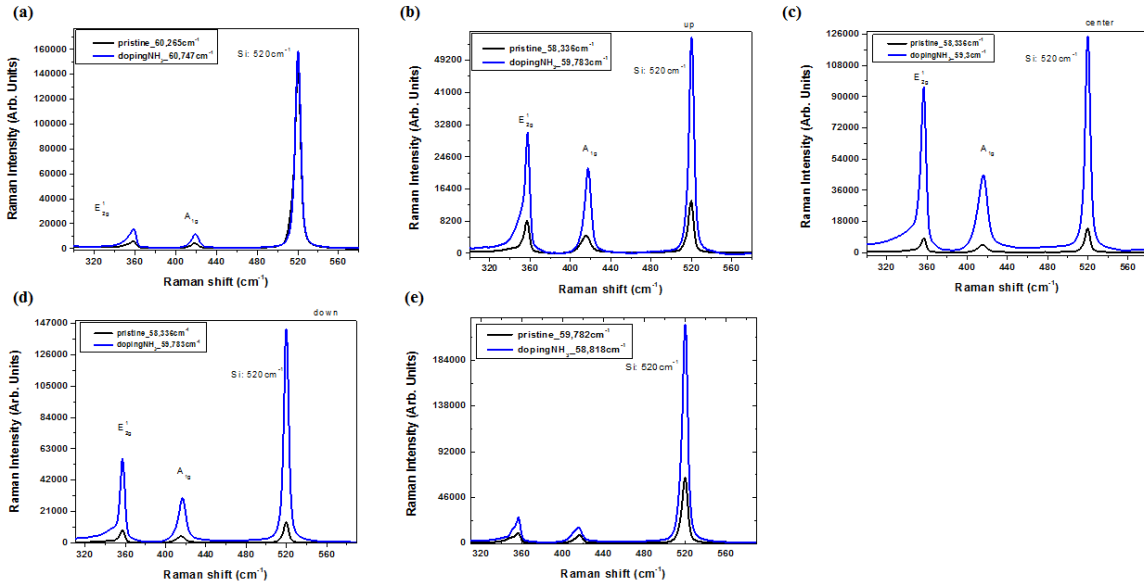


Figure 38: Micro-Raman spectra at $T=300K$ for WS_2 on SiO_2/Si before and after photochemical doping with NH_3 . Black line for the pristine and blue for the irradiated sample. Dot lines show the shift of the peaks. (a) sample 6, (b) sample 7 up, (c) sample 7 center, (d) sample 7 down, (e) sample 8

Table 3: The characteristics Raman peaks E_{2g}^1 , A_{1g} before and after photochemical doping with NH_3 , are summarized for all the samples. Data refer to peak position, intensity and FWHM.

Samples	E_{2g}^1 (cm^{-1})	Intensity E_{2g}^1 (counts)	FWHM E_{2g}^1 (cm^{-1})	A_{1g} (cm^{-1})	Intensity A_{1g} (counts)	FWHM A_{1g} (cm^{-1})
Before radiation (6)	358.00	4453	10.53	418.26	3702	7.76
After radiation (6)	358.49	11210	6.91	419.23	10365	10.14
Before radiation (7) up	357.04	6913	6.15	415.38	4139	12.51
After radiation (7) up	357.52	23210	4.82	417.30	19272	7.86
Before radiation (7) center	357.04	6907	5.83	415.38	4084	12.02
After radiation (7) center	357.04	85175	7.80	416.34	40062	13.34
Before radiation (7) down	357.04	7471	5.87	415.38	4032	12.30
After radiation (7) down	357.04	48470	5.46	416.82	26824	10.59
Before radiation (8)	356.56	6627	4.63	416.34	7420	8.87
After radiation (8)	356.56	19480	8.98	415.38	13984	12.62

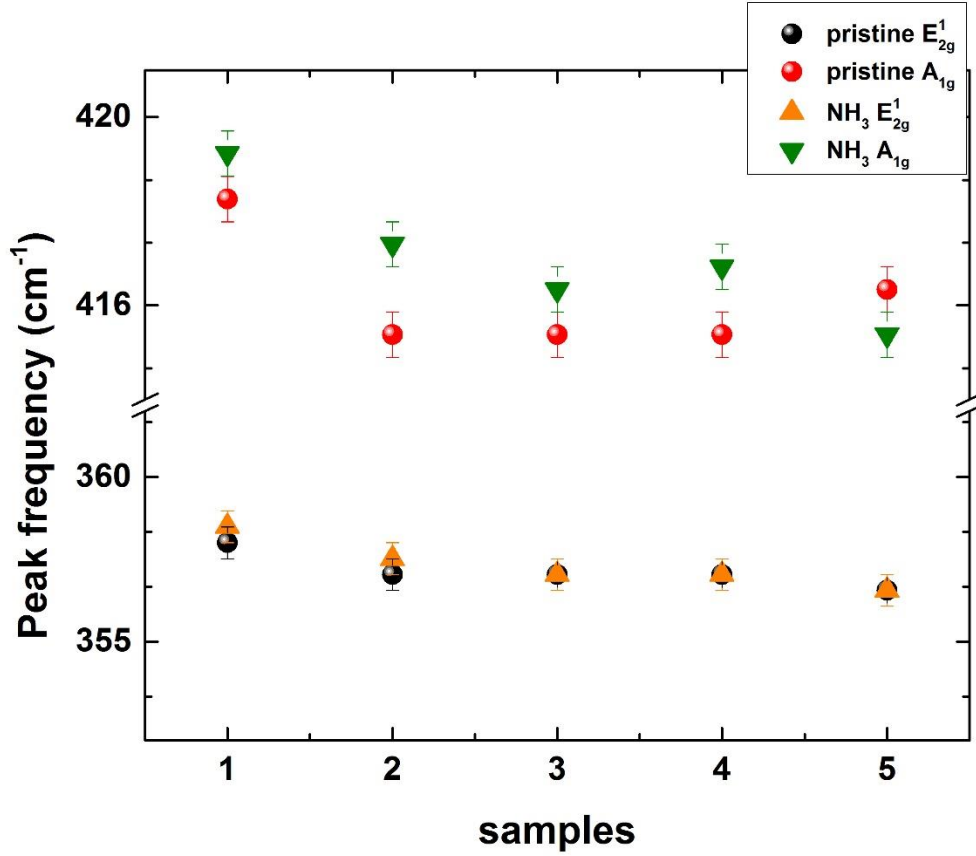


Figure 39: Peak frequencies of the E_{2g}^1 and A_{1g} mode before and after photochemical doping with NH_3 , for samples 6-8.

For the sample 7, we took micro-Raman measurements from three different areas (Fig.31). Graph 39 illustrates the peak frequency as a function of sample number, we rename the sample 7 for the region up, center and down as 7, 8, 9 and the sample 8 as sample 10.

From Fig. 38 and 39 and after data analysis, it is found that the A_{1g} mode slightly blue shifts by $\sim 1.5 \text{ cm}^{-1}$ after photochemical doping with NH_3 . A blue shift of $\sim 0.5 \text{ cm}^{-1}$ for the in plane mode E_{2g}^1 is observed. This value is within our experimental error. The strain effect in nitrogen doped monolayer WS_2 is negligible. The adsorption of nitrogen molecules reduces the electron concentration in monolayer WS_2 . All the results were measured in the exact same area of the monolayer for each sample. All Raman bands showed stronger intensities after photochemical doping. A possible reason that we can observe a strong intensity is the structural healing which is achieved after photochemical doping with NH_3 . The FWHM of out of plane mode remarks increasing after radiation in nitrogen environment.

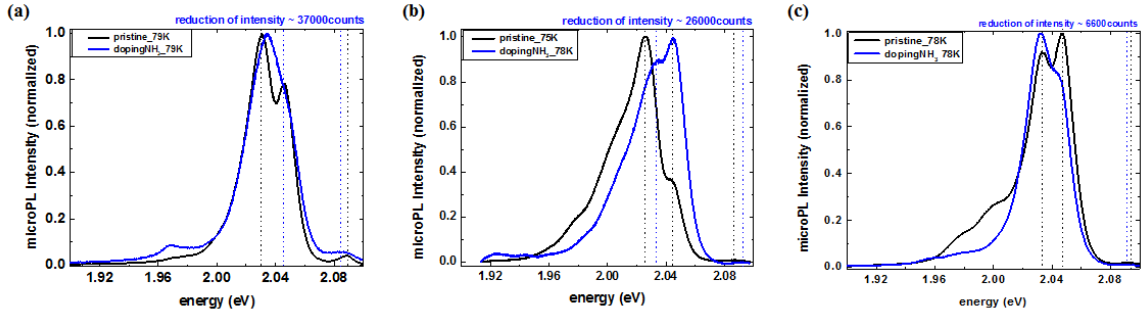


Figure 40: Normalized to intensity micro-PL spectra. Comparison before and after photochemical doping with NH_3 . The excitation laser wavelength here is 532nm. Measurements were performed at temperature $T=78\text{Kelvin}$. The laser power is 21microWatts, approximately. Black line for the pristine and blue for the irradiated sample. Dot lines show the shift of the peaks. (a) sample 6, (b) sample 7, (c)sample 8.

Table 4: In this table, the characteristics micro-PL peaks XX , X^- and X before and after photochemical doping with NH_3 , are summarized for all the samples. The data relate to non-normalized charts and give the values for peak position, intensity and FWHM.

Samples	XX (eV)	Intensity of XX (cps)	FWHM of XX (meV)	X^- (eV)	Intensity of X^- (cps)	FWHM of X^- (meV)	X (eV)	Intensity of X (cps)	FWHM of X^- (meV)
Before radiation (6)	2.031	46600	33	2.049	15520	9	2.087	1800	13
After radiation (6)	2.034	8943	31	2.052	1167	10	2.086	589	18
Before radiation (7)	2.027	58975	13	2.046	12136	11	2.080	354	5
After radiation (7)	2.039	32601	57	2.046	11623	12	2.093	98	36
Before radiation (8)	2.034	46530	20	2.047	28801	9	2.093	974	13
After radiation (8)	2.032	39890	24	2.048	15070	15	2.092	334	6

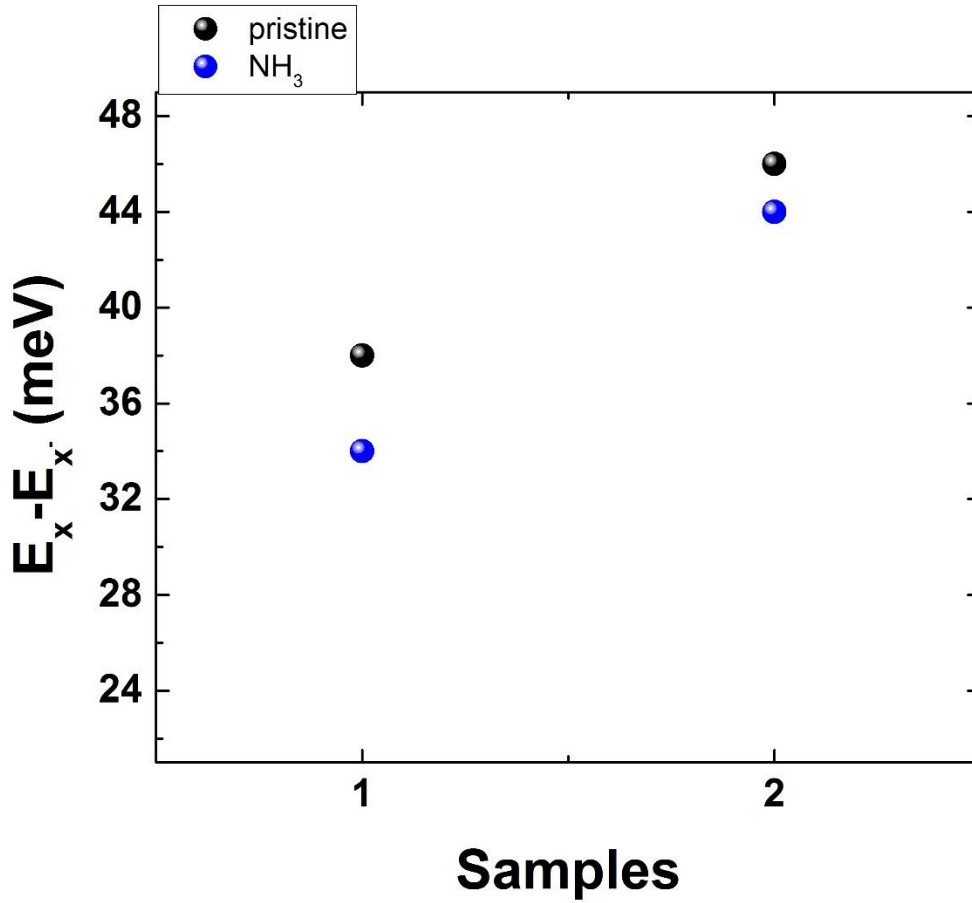


Figure 41: The trion dissociation energy, $\Delta E = E_x - E_{x^-}$, before (black bullets) and after radiation (blue bullets) photochemical doping with NH_3 .

The dependence of trion (X^-) and exciton (X) on photochemical doping with nitrogen is also investigated. Fig. 40 illustrates the micro-PL spectra and the table 4 sums up the results. The PL spectra in Fig. 40 shows that the peak position X slightly red shifts after radiation, while that of X^- remain almost unchanged with doping. The PL intensity is reduced when monolayer WS_2 is covered with dopants and FWHM of the peaks shows a systematic increase after the radiation.

The typical trion dissociation energy, ΔE , is found to be larger before radiation (Fig. 41). The PL intensity is reduced when monolayer WS_2 is covered with dopants.

The samples after radiation in chlorine and nitrogen environment seem to have similar results. It is obvious that the samples after chlorine radiation have greater changes than the ones with nitrogen.

II.5 Micro-PL temperature dependence before and after photochemical doping with Cl_2 and NH_3

To further understand the properties of excitonic peaks appearing in a spectrum measured at $T=78K$, we performed temperature dependent micro-PL measurements.

Figures 42 and 43 show micro-PL spectra of single layer WS_2 for various temperatures, before and after laser irradiation in chlorine environment (black and red lines respectively). In these measurements the laser excitation power is kept at $20\mu W$. The laser excitation wavelength is $532nm$. The red labels on the graph display the intensity decrease after irradiation. In addition to compare the graphs due to the great difference in magnitude of intensity we had to normalize them.

The PL emission lines between $1.9 - 2.0 eV$, are attributed to localized excitons, which do not survive in temperatures higher than $100K$. This feature is usually considered as an evidence of disorder-related effects [60]. Also, at low temperatures, the spectra consist of one peak at $2.03eV$, which is assigned as a molecule of two excitons called “biexciton” (XX). This peak is clear and sharper after radiation.

Peaks, which we attribute to the trion (X^-) and exciton (X) are presented for all temperatures. Even at room temperature, these peaks, can be separated due to their small linewidth. As the temperature rises, both micro-PL peaks experience a red shift (Fig. 44), in accordance with Varshni equation (eq. 11), which describes the change of the bandgap with temperature in a large variety of semiconductors. We assume that the trion and exciton binding energies are temperature independent. After this, we use equation 11, from chapter I.2.5, to fit the PL peak positions extracted for each temperature, as depicted in Fig. 44. The phenomenological peak parameters a and b are displayed on the graph. The fit matches with $E_g(0) = 2.06eV$ for X^- and $E_g(0) = 2.1eV$ for X . After radiation in chlorine environment, both peaks experience a red shift for all temperatures.

By tuning the Fermi level in our samples, we can assign the $2.045eV$ peak to trion emission and the $2.08eV$ PL peak to exciton emission at $T=78K$. At low temperatures, we observe the emergence of a lower energy peak (biexciton), which will be further discussed in the next chapter.

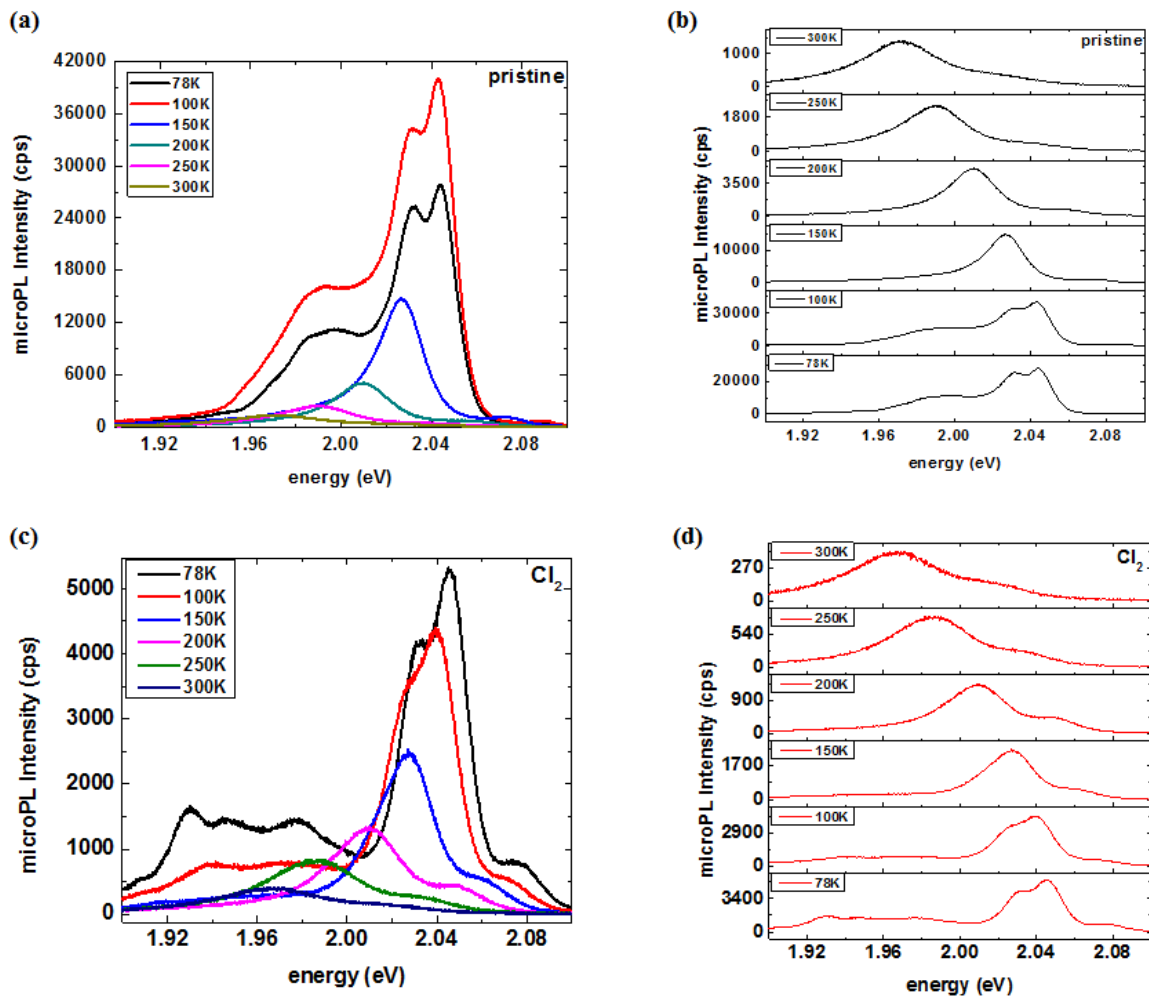


Figure 42: PL spectra of a single layer WS_2 (a), (b) pristine (c), (d) after photochemical doping with Cl_2 . Measured at different temperature intervals between 78K and 300K.

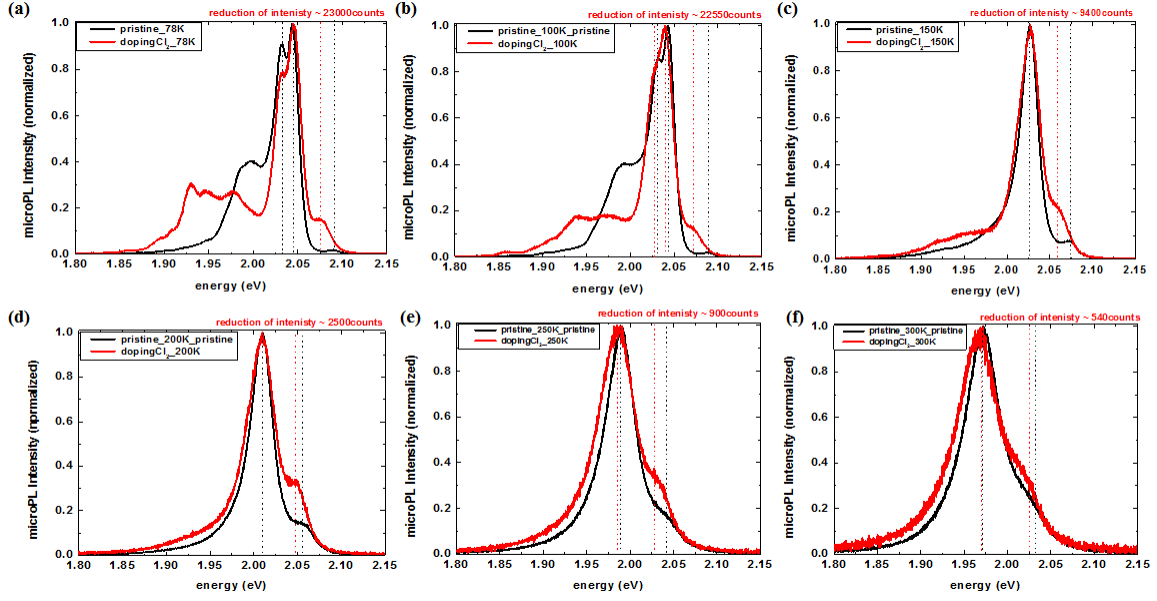


Figure 43: Temperature-dependent micro-PL spectra of WS_2 normalized to intensity. Black line represents the pristine and red line represents the irradiated sample in chlorine environment. Dot lines show the shift of the peaks. Laser excitation wavelength is 532nm. On the charts displays the loss of intensity after irradiation. The laser power is 21microWatts, approximately. (a) 78Kelvin, (b) 100Kelvin, (c) 150Kelvin, (d) 200Kelvin, (e) 250Kelvin, (f) 300Kelvin.

Table 5: In this table, the characteristics of micro-PL peaks XX , X^- and X before and after photochemical doping with Cl_2 , are summarized for all the samples. Data relating to the study on temperature dependence. Also, data correspond to non-normalized charts and give the values for peak position, intensity and FWHM.

Temperature (K)	XX (eV)	Intensity of XX (cps)	FWHM of XX (meV)	X^- (eV)	Intensity of X^- (cps)	FWHM of X^- (meV)	X (eV)	Intensity of X (cps)	FWHM of X (meV)
78 (before radiation)	2.032	25200	13	2.044	27700	9	2.090	516	7
78 (after radiation)	2.031	3573	20	2.047	4160	15	2.078	842	35
100 (before radiation)	2.032	16570	20	2.043	25660	10	2.088	670	8
100 (after radiation)	2.026	2395	19	2.041	3110	17	2.071	437	34
150 (before radiation)	-	-	-	2.026	11550	22	2.074	605	15
150 (after radiation)	-	-	-	2.026	2122	30	2.062	358	19
200 (before radiation)	-	-	-	2.009	3544	25	2.058	337	24
200 (after radiation)	-	-	-	2.009	1048	36	2.050	258	22
250 (before radiation)	-	-	-	1.989	1530	32	2.042	144	32
250 (after radiation)	-	-	-	1.985	585	43	2.034	130	26
300 (before radiation)	-	-	-	1.971	785	36	2.023	92	39
300 (after radiation)	-	-	-	1.966	242	45	2.018	60	33

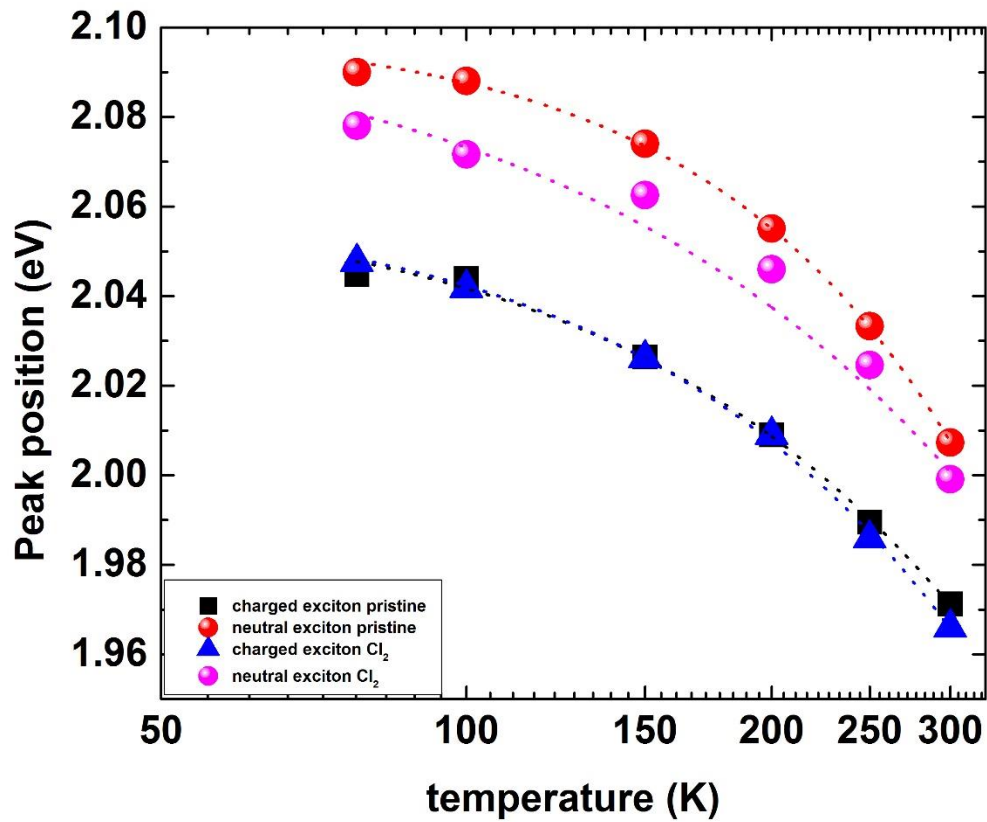


Figure 44: Exciton (X) and trion (X^-) micro-PL peak energies as a function of temperature. the dot lines represent the fits to experimental data following the Varshni equation. Black squares and blue triangles represent the trion peak energies before and after radiation in chlorine environment, respectively. Red and pink bullets represent the exciton peak energies before and after photochemical doping with Cl_2 , respectively.

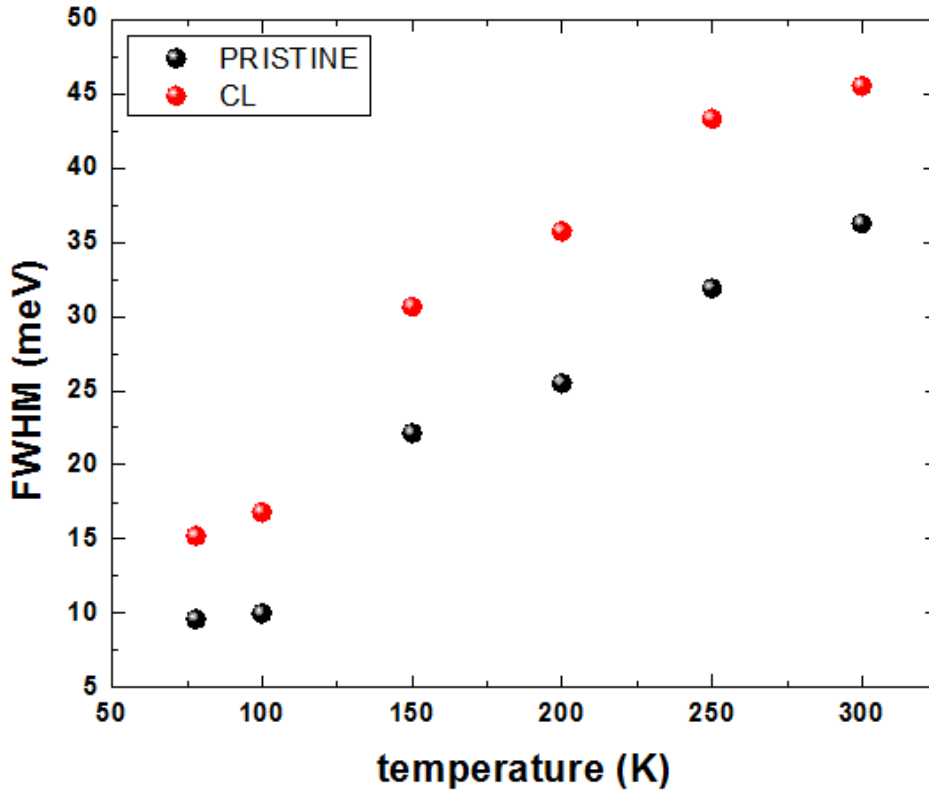


Figure 45: The trion X^- spectral width as a function of temperature is collected from micro-PL measurements. Black bullets for pristine and red bullets after radiation in chlorine environment.

Figures 46 and 47 show the micro-PL spectra of single layer WS_2 for various temperatures, before and after radiation in nitrogen environment (black and blue lines respectively). The results seem to be the same with results of temperature dependence before and after chlorination treatment. We observe a decrease in intensity with chemical doping, in both cases. The red shift for peak X is smaller in the case of nitrogen (Fig. 48 green bullets).

Full width half maximum (FWHM) as a function of temperature is plotted in Figure 45 and 49 before and after radiation in chlorine (Fig. 45) and nitrogen (Fig. 49) environment. The rapid increase of the linewidth in $T=100-150K$ (Fig. 45) and $T=78-100K$ (Fig. 49) indicates a crossover from non-thermalized to thermalized energy distribution of localized excitons. In Fig. 45, we observe a linear increase with temperature from $T=150-300K$. A quick increase of the linewidth (Fig.49) at temperature $T=100-150K$ can be explained due to the carriers become progressively mobile above temperatures $T=100K$.

Therefore, the carrier distribution narrows and the linewidth decreases. After $T=150\text{K}$, the role of the regular thermalization of carriers starts to become more and more important, which results in the linewidth increase at a lower rate up to the full-delocalized temperature of $T_{max} = 100\text{K}$. Finally, the linewidth increases markedly until 300K in thermalization of the carriers. Additionally, it is obvious that after laser irradiation in chlorine and nitrogen environment the linewidth of charged exciton (trion) is increased. The curves broaden with increasing temperature. This is due to higher population of carriers (monolayer is more charged) and interactions between them.

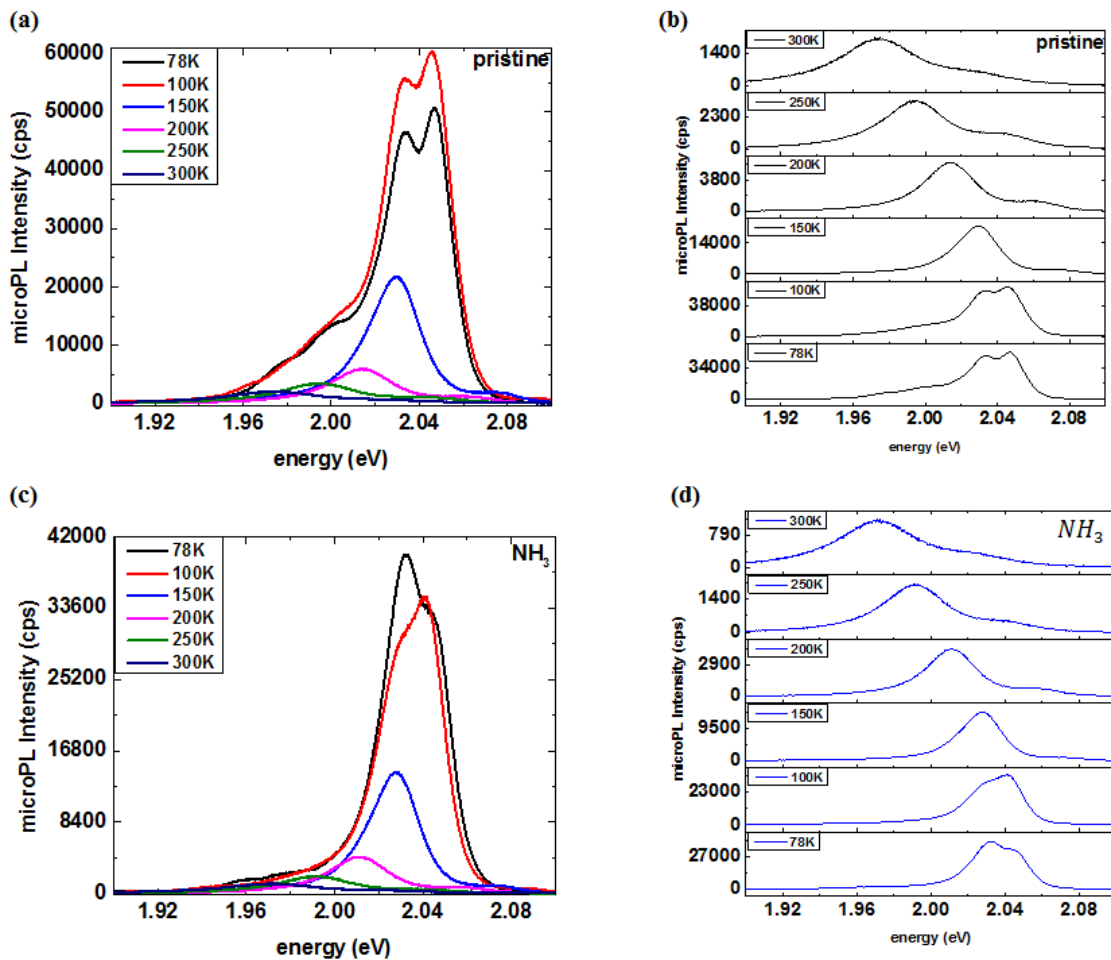


Figure 46: PL spectra of a single layer WS_2 (a), (b) pristine (c), (d) after photochemical doping with NH_3 . Measured at different temperature intervals between 78K and 300K .

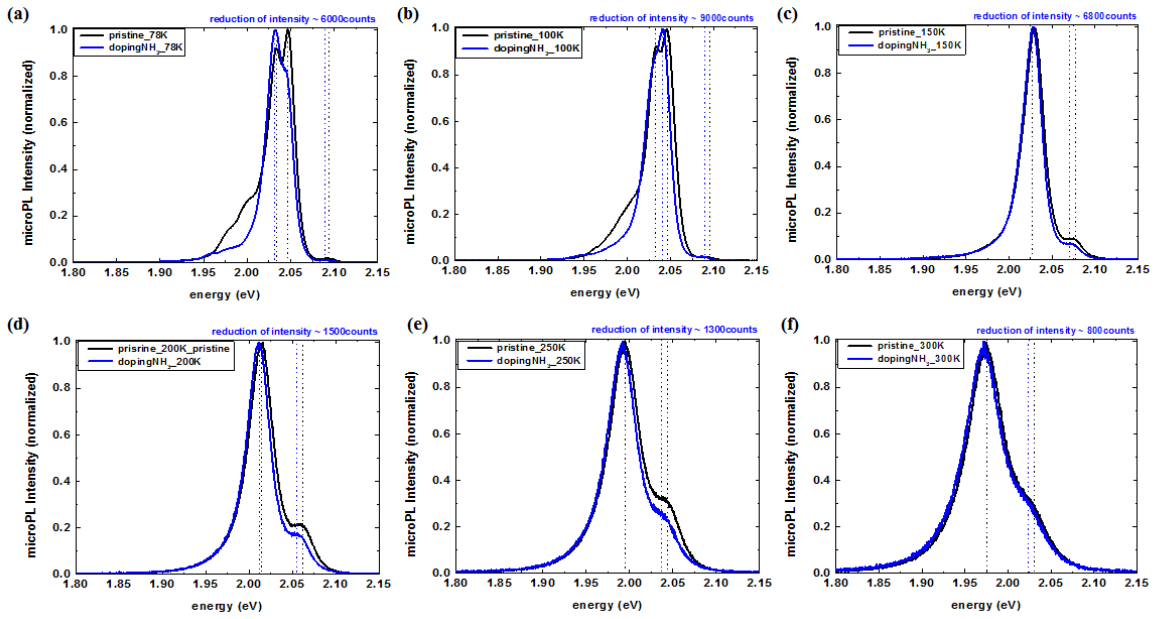


Figure 47: Temperature-dependent micro-PL spectra of WS_2 normalized to intensity. Black line represents the pristine and blue line represents the irradiated sample in nitrogen environment. Dot lines show the shift of the peaks. Laser excitation wavelength is 532nm. On the charts displays the loss of intensity after irradiation. The laser power is 21microWatts, approximately. (a) 78Kelvin, (b) 100Kelvin, (c) 150Kelvin, (d) 200Kelvin, (e) 250Kelvin, (f) 300Kelvin.

Table 6: In this table, the characteristics of micro-PL peaks XX, X⁻ and X before and after photochemical doping with NH₃, are summarized for all the samples. Data relating to the study on temperature dependence. Also, data correspond to non-normalized charts and give the values for peak position, intensity and FWHM.

Temperature (K)	XX (eV)	Intensity of XX (counts)	FWHM of XX (meV)	X ⁻ (eV)	Intensity of X ⁻ (counts)	FWHM of X ⁻ (meV)	X (eV)	Intensity of X (counts)	FWHM of X ⁻ (meV)
78 (before radiation)	2.034	34280	19	2.047	19868	10	2.093	916	6
78 (after radiation)	2.032	34175	24	2.047	13615	12	2.091	974	5
100 (before radiation)	2.031	40601	16	2.047	24340	17	2.091	903	6
100 (after radiation)	2.029	31890	20	2.044	15800	28	2.085	578	16
150 (before radiation)	-	-	-	2.029	20106	24	2.075	1809	26
150 (after radiation)	-	-	-	2.027	13270	30	2.072	888	21
200 (before radiation)	-	-	-	2.013	5480	27	2.063	1835	26
200 (after radiation)	-	-	-	2.011	3965	36	2.060	660	26
250 (before radiation)	-	-	-	1.994	3120	32	2.044	850	31
250 (after radiation)	-	-	-	1.991	1834	47	2.042	383	30
300 (before radiation)	-	-	-	1.973	1860	38	2.026	407	43
300 (after radiation)	-	-	-	1.971	1038	60	2.023	220	37

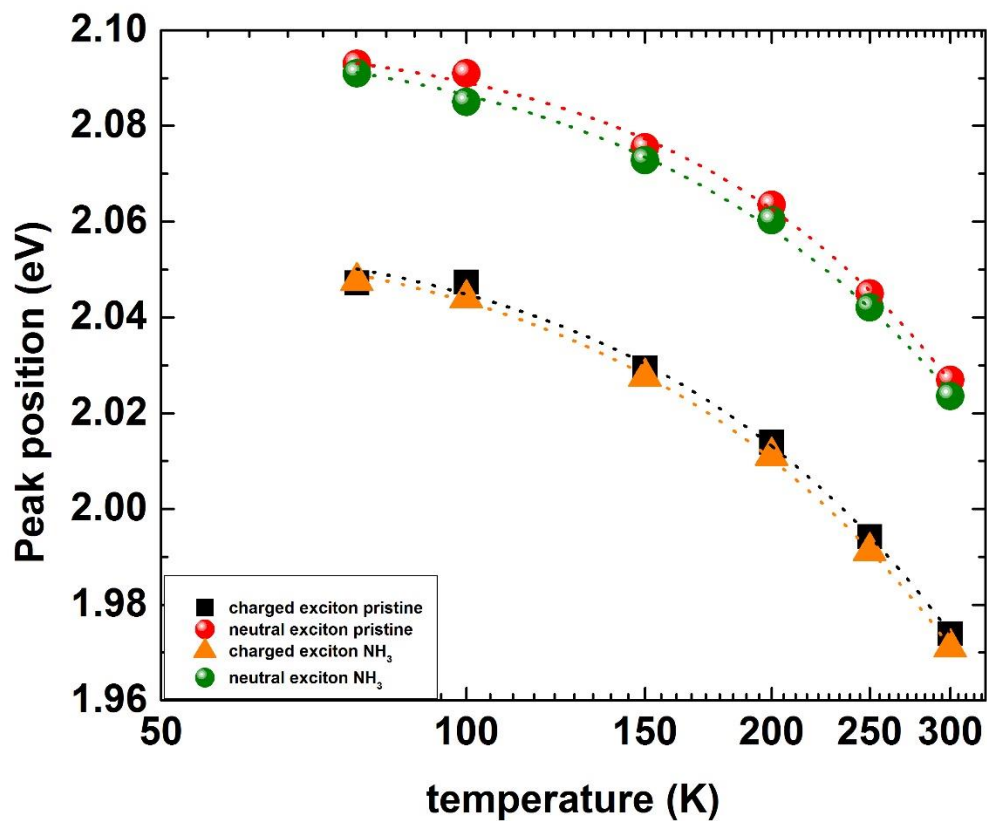


Figure 48: Exciton (X) and trion (X^-) micro-PL peak energies as a function of temperature. the dot lines represent the fits to experimental data following the Varshni equation. Black squares and yellow triangles represent the trion peak energies before and after radiation in nitrogen environment, respectively. Red and green bullets represent the exciton peak energies before and after photochemical doping with NH_3 , respectively.

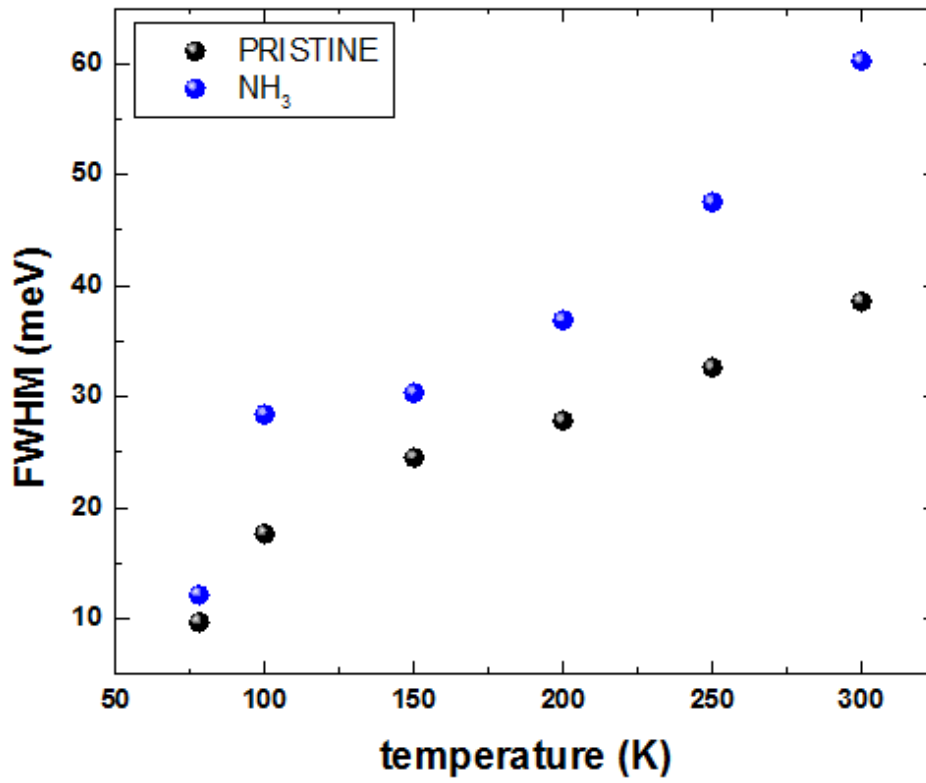


Figure 49: The trion X^- spectral width as a function of temperature is collected from micro-PL measurements. Black bullets for pristine and blue bullets after radiation in nitrogen environment.

II.6 Identification of biexcitons in monolayer WS_2 after photochemical doping with Cl_2

Samples in this section, are prepared by mechanical exfoliation of bulk crystal WS_2 on SiO_2/Si substrates. Single layer regions are identified with an optical microscope as shown in Fig. 50. Single layers are characterized with Raman spectroscopy. The monolayer size is $19.1\mu m$ on y-axis and $5.8\mu m$ on x-axis. Raman spectra are shown in Fig. 34 (e). The following procedure took place after laser irradiation in chlorine environment. The purpose is the identification of biexciton emission at 78K [46].

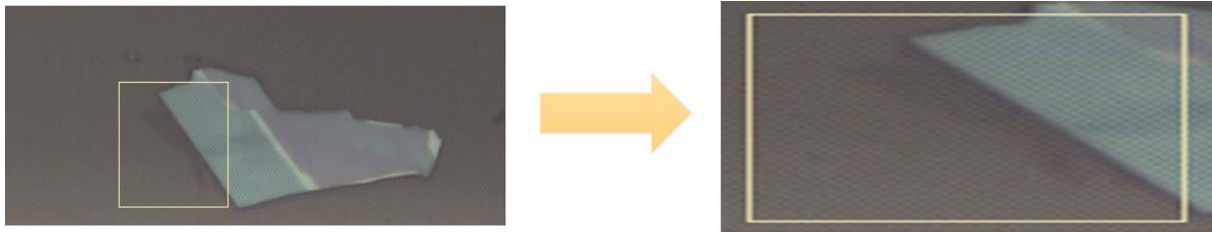


Figure 50: Confocal microscope image of a representative exfoliated WS_2 sample. The yellow square indicates monolayer region. This is sample 5, the figure and the following measurements taken after photochemical doping with Cl_2 with fluence = $6.5 \text{ mJ}/\text{cm}^2$.

At low ($T=78\text{K}$) and high ($T=200\text{K}$) temperature, we observe the emergence of a low-energy peak, which we identify as a superposition of defect bound exciton and biexciton emission by the power dependence of its emission intensity.

For low temperature measurements ($T=78\text{K}$) the sample is mounted in a cryostat. The setup is the same setup of micro-PL which have described in section I.4.3. The cw laser used for excitation are focused with a 40x microscope objective onto the sample. Laser excitation wavelength is 532nm (2.033eV). Here we demonstrate the existence of biexciton states in monolayer WS_2 . The biexciton is identified as a sharply defined state in photoluminescence for big range of power values at $T=78\text{K}$. To identify biexciton states, we have studied the photoluminescence spectra at different power exciton densities. The higher power density was $229.29 \text{ kW}/\text{cm}^2$ ($1800\mu\text{Watts}$) and the lowest $0.076 \text{ kW}/\text{cm}^2$ ($0.6\mu\text{Watts}$). Figure 51 shows the PL spectra at $T=78\text{K}$ for different excitation powers. Fig. 52 shows six characteristic graphs selected from PL spectra from Fig. 51. It is obvious from Fig. 51 that the peak of biexciton redshifts by about 10meV . The odd characteristic in Fig. 52 is that at low excitation power the peak of charged exciton (X^-) is higher than the peak of biexciton (XX) (Fig 51 (a), (b)). We observe that the two peaks have the same intensity at $36\mu\text{Watts}$ (Fig 52 (c)). If we

further increase the power, the biexciton peak is dominant (Fig 52 (d), (e)). Additionally, a second low-energy peak around 2eV, may stem from defect-bound excitons. Its intensity decreases compared to other peaks with increasing excitation power.

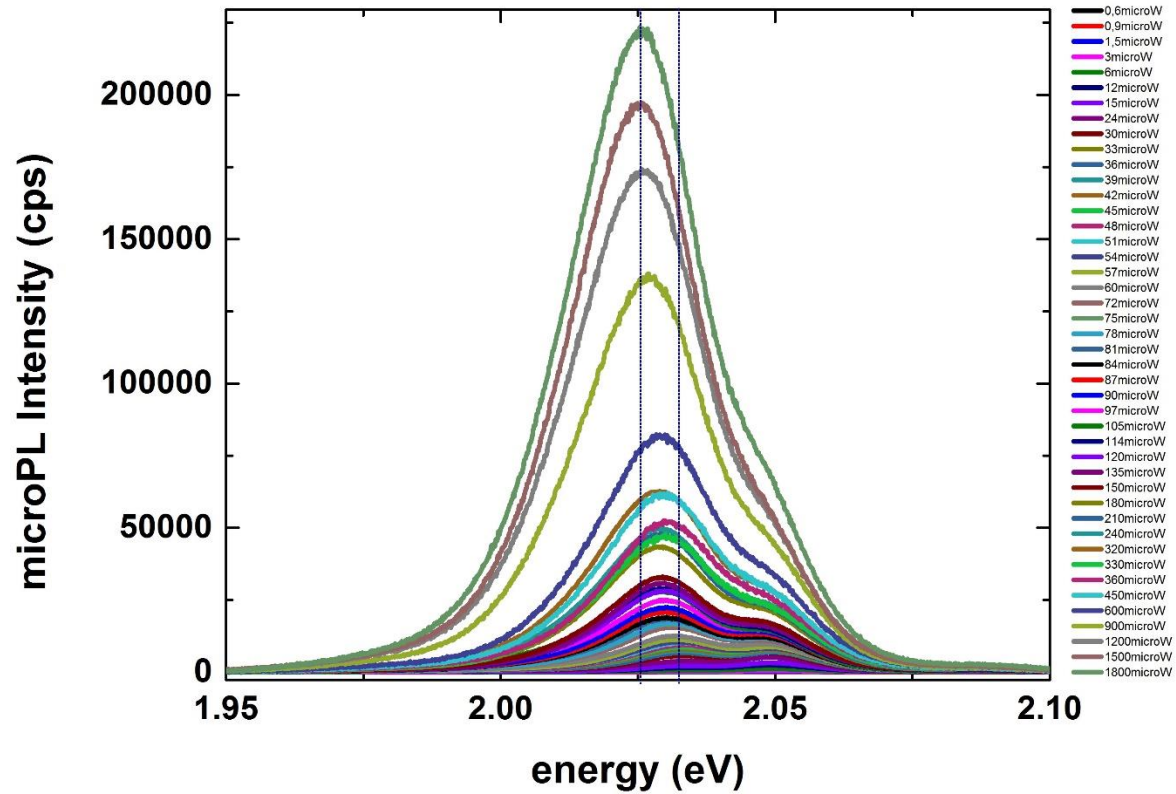


Figure 51: Micro-PL spectra of single layer WS_2 at $T=78$ Kelvin for various excitation densities. The experiment was performed after irradiation of sample in chlorine environment. The excitation laser wavelength is 532nm. Dot lines illustrates the red shift of biexciton peak.

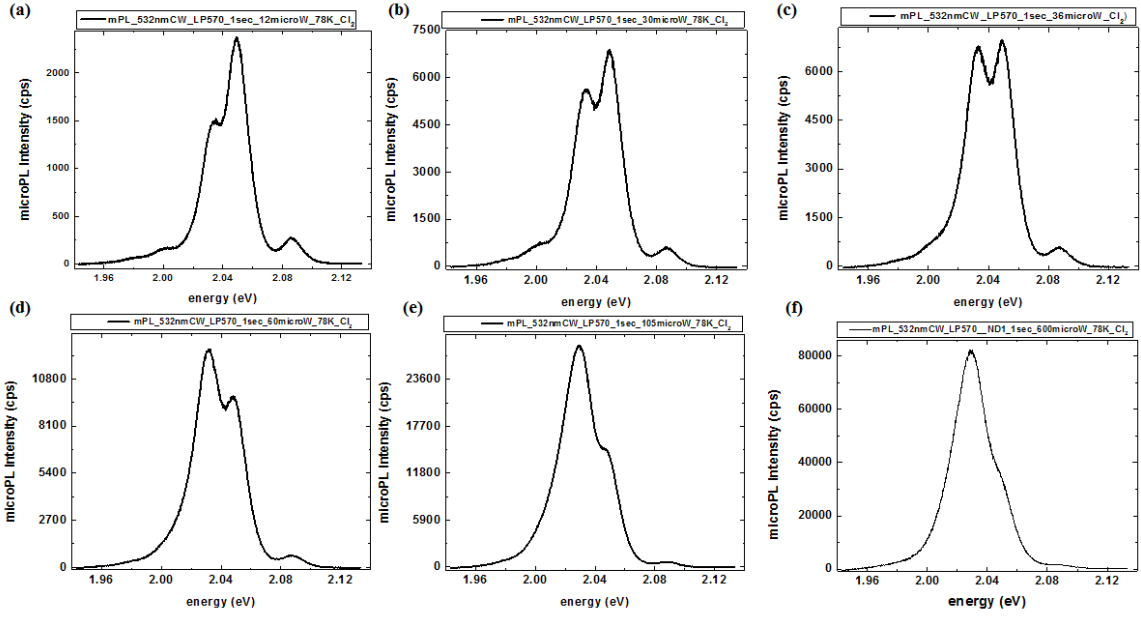


Figure 52: Six characteristics micro-PL spectra of single layer WS_2 at $T=78$ Kelvin for various excitation densities. The experiment was performed after irradiation of sample in chlorine environment. The excitation laser wavelength is 532nm. It is obvious that at low values of power density, the peak of charged exciton (X^-) is dominant. At 60microW both peaks (XX, X^-) have equal intensity, while at high values of power density the peak of biexciton (XX) is dominant. The six power densities are (a) 12microW, (b) 30microW, (c) 36microW, (d) 60microW, (e) 105microW, (f) 600microW.

To have a better understanding about the biexciton nature we created the plots in Fig. 53. We extract the micro-PL intensity for XX, X^- and X for different excitation densities. These values are same with these of graph in Fig. 51. The double logarithmic graph is displayed in Fig. 53 (a). The dot lines represent the fits to the experimental data following the equation:

$$y = a * x^b \quad (17)$$

For biexciton (black squares) and trion (red bullets), we have double fitting. First, we have the fitting for low excitation power and after for high excitation power. The XX intensity exhibits a linear dependence for low excitation power densities, while for higher values a superlinear dependence of PL intensity to the power density occurs. X^- and X present linear behavior indicated by the red and blue dot lines, but we have a drop in deviation for trion (X^-) at high excitation powers. Fig. 53 (b) shows a double logarithmic plot of neutral exciton's (X) intensity as a function of biexciton's intensity (XX) (black squares) and the intensity of neutral exciton as a function of charged exciton intensity (X^-) (red bullets). In this graph, one can see the different behavior of biexciton in compared to charged exciton. The black squares follow a

linear dependence at low excitation densities, while for excitation densities larger than 4.96 kW/cm^2 , data are well-described by a quadratic fit, with a parameter $b=1.19$. The following diagram (Fig. 53 (c)) illustrate the intensity of charged exciton as a function of biexciton intensity. Here the quadratic nature of biexciton is more clear. For higher values of power density the constant b is 1,65. Constant b indicates the slope in our graphs.

Such a quadratic increase in micro-PL emission intensity is expected for biexcitons (Fig. 22 (b)). Nevertheless, smaller slopes are often observed (Fig. 53 (a)) due to the kinetics of biexciton formation and exciton recombination. With increasing excitation density the XX emission begins to dominate. As shown in Fig. 53 (d) the XX peak redshifts by about 10 meV in the excitation density range. The X^- and X do not shift with increasing laser power.

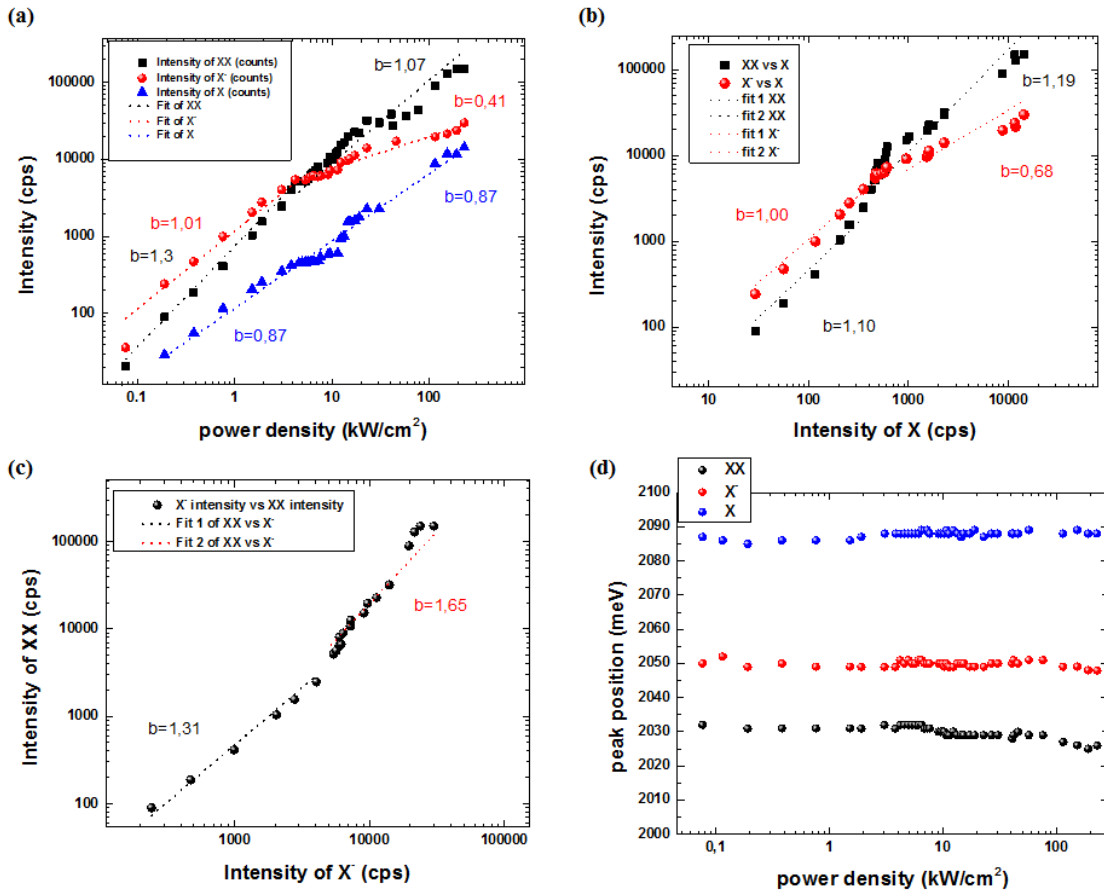


Figure 53: Experimental results of micro-PL measurements at $T=78K$, with excitation laser wavelength 532nm (a) Double-logarithmic plot of micro-PL Intensity of XX (black squares), X^- (red bullets), and X (blue triangles) as a function of excitation density. A linear behavior indicated by the dot lines, after Gaussian fit. (b) Double-logarithmic plot of micro-PL Intensity of X as a function of micro-PL Intensity of XX (black squares) and X^- (red bullets). A linear behavior indicated by the dot lines, after Gaussian fit. (c) Double-logarithmic plot of micro-PL Intensity of X^- as a function of micro-PL Intensity of XX. A linear behavior indicated by the dot lines, after Gaussian fit. (d) Micro-PL position for XX, X^- and X peaks as a function of excitation density.

Next step in our consideration, is the identification of biexciton emission by the power dependence of its emission intensity, but now at higher temperature. The conditions of the experiment remain the same with the only change in temperature value. The measurements shown in Fig.54 proceeded at $T=200K$. The micro-PL spectra has now two dominant peaks, due to increased temperature. Our aim here is to establish the identity of peak at 2.01eV. Specifically, we want to determine whether the peak until now called as peak of charged exciton, constitutes an overlap of biexciton and charged exciton. In other words, if this peak displays a biexciton nature, which can't be distinguished by temperature rise. By following the previous process to identify biexciton states, we have studied the photoluminescence spectra at

different power exciton densities (Fig. 54). The higher power density was $152 \text{ kW}/\text{cm}^2$ ($900 \mu\text{Watts}$) and the lowest $0.019 \text{ kW}/\text{cm}^2$ ($0.15 \mu\text{Watts}$). It is obvious from Fig. 54 that the peak of biexciton redshifts by about 28 meV . The peak from 2.01 eV shifts to 1.98 eV . Dot lines display this shift.

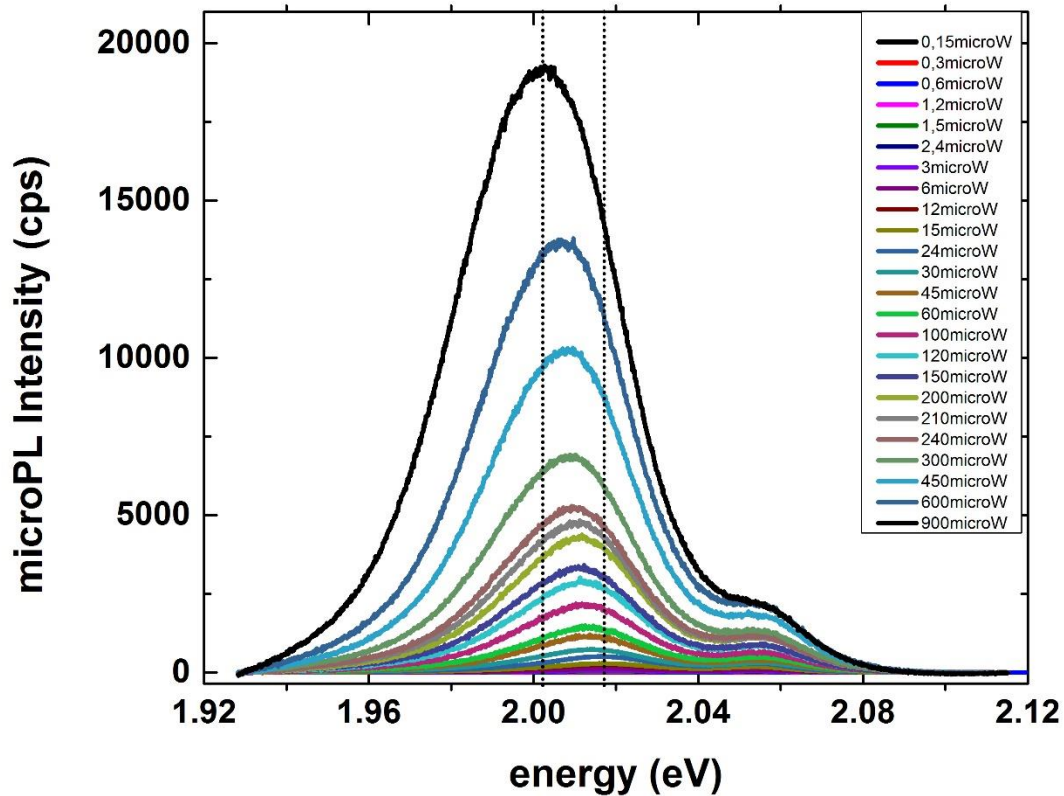


Figure 54: Micro-PL spectra of single layer WS_2 at $T=200 \text{ Kelvin}$ for various excitation densities. The experiment was performed after irradiation of sample in chlorine environment. The excitation laser wavelength is 532 nm . Dot lines illustrates the red shift of biexciton peak.

Fig. 55 shows six graphs of relative values of power density. It is obvious that at low values of power densities, the intensity difference between the peaks is small. As we increase the power density, the difference grows.

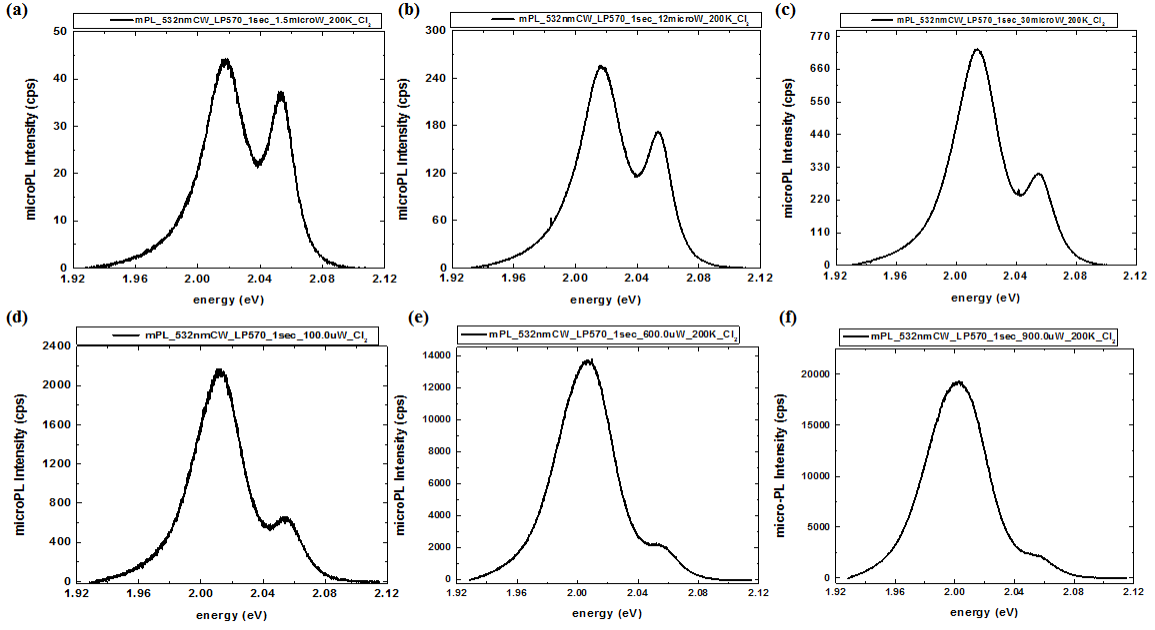


Figure 55: Six characteristics micro-PL spectra of single layer WS_2 at $T=200\text{Kelvin}$ for various excitation densities. The experiment was performed after irradiation of sample in chlorine environment. The excitation laser wavelength is 532nm . The six power densities are (a) 1.5microW , (b) 12microW , (c) 30microW , (d) 100microW , (e) 600microW , (f) 900microW .

In Fig. 56, the graphs referred to three different peaks, by considering that the peak of charged exciton partially overlaps with the peak of biexciton. From Fig. 56 (b) and (c), we can see the quadratic dependence in micro-PL emission intensity as it is expected for biexcitons. Fig. 56 (d) proves that the peak position at high power densities begin to differentiate. This difference performed from $30\mu W$ ($3.821\text{ kW}/\text{cm}^2$) and after. The XX peak, as allowed us to call it most, redshifts by about 28meV in the excitation density range. This indicates that the emission from defect-bound excitons at low excitation density is at a higher energy than the biexciton emission at high excitation density. The local heating, which induced by the laser, is a reason for the redshift of biexciton, since neither X^- and X peaks display a redshift. The neutral exciton peak shows a slight blueshift.

The energy separation of $\sim 60\text{meV}$ between the X and XX features is the exciton binding energy, $E_{b,XX}$. The value of the exciton binding energy is still under discussion.

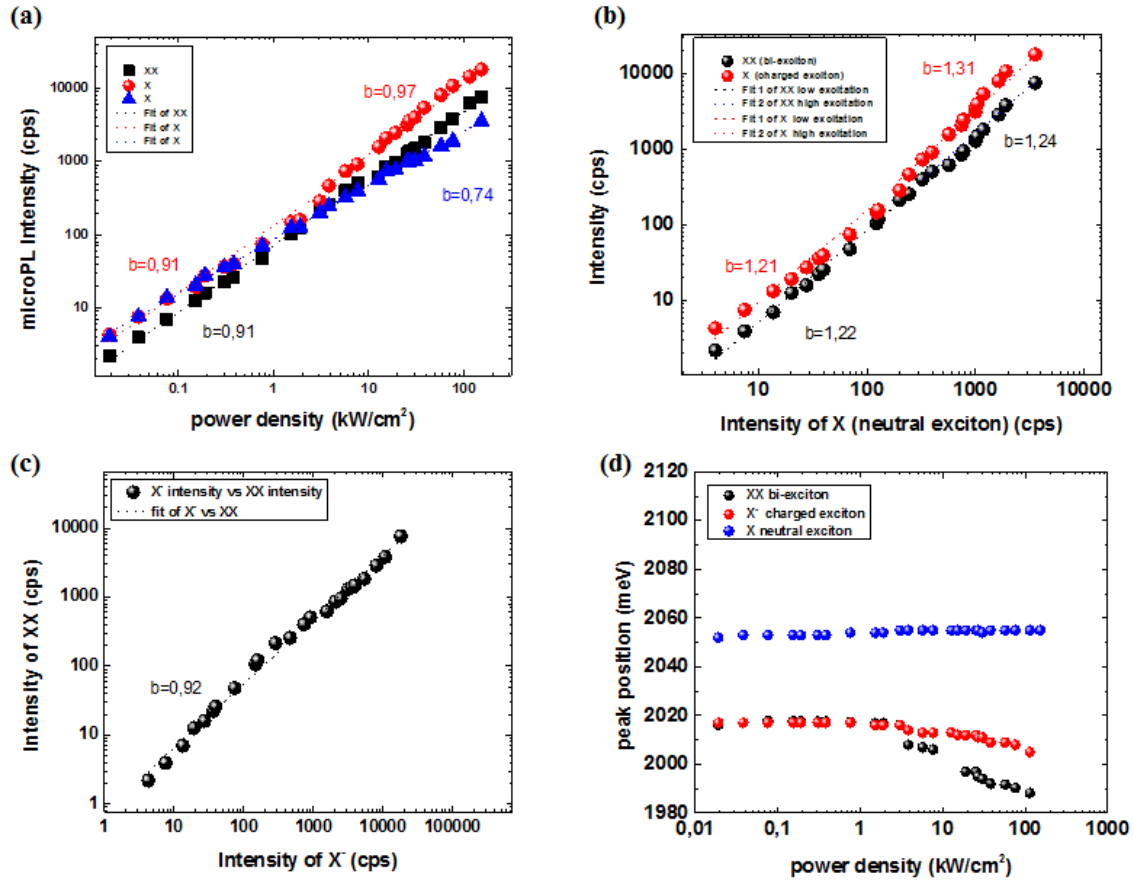


Figure 56: Experimental results of micro-PL measurements at $T=200\text{K}$, with excitation laser wavelength 532nm (a) Double-logarithmic plot of micro-PL Intensity of XX (black squares), X^- (red bullets), and X (blue triangles) as a function of excitation density. A linear behavior indicated by the dot lines, after Gaussian fit. (b) Double-logarithmic plot of micro-PL Intensity of X as a function of micro-PL Intensity of XX (black squares) and X^- (red bullets). A linear behavior indicated by the dot lines, after Gaussian fit. (c) Double-logarithmic plot of micro-PL Intensity of X^- as a function of micro-PL Intensity of XX . A linear behavior indicated by the dot lines, after Gaussian fit. (d) Micro-PL position for XX , X^- and X peaks as a function of excitation density.

Finally, we find that the exciton and trion peaks are well separated even at $T=200\text{K}$. Also, we observe the emergence of a lower energy peak, which we identify as biexciton emission. Fig. 56 shows that the low energy peaks approach the biexciton emission character

III. Conclusion and future plans

This thesis discussed about a new photochemical doping of monolayer WS_2 with chlorine and nitrogen gas. The use of pulsed UV laser is a fast and simple method for controlling the optical and electronic properties of a monolayer TMD material. The main topics covered here are the exfoliation and characterization of monolayer WS_2 before and after photochemical doping. We studied a new method, photochemical doping. This technique is based on radiating the monolayer crystal with the presence of gas carriers (dopants) by a pulsed laser.

Raman scattering in monolayer WS_2 shows that the separation of the two modes, E_{2g}^1 and A_{1g} , is an estimation of crystal thickness and a method which can help us investigate the effects of chemical doping. The photochemical doping technique leads to a systematic blue shift of A_{1g} mode after radiation in Cl_2 and NH_3 environment.

Micro-photoluminescence experiments on monolayer WS_2 show that spectrum is dominated by emission from a negative exciton (X^-), due to the n-type nature of the crystal. The trion/exciton intensity ratio can be tuned by photochemical radiation. This is a direct evidence that, we can control the density of carriers in a 2D system. Temperature dependent photoluminescence measurements on mechanically exfoliated sample, reveal the existence of neutral and charged excitons at low temperatures as well as at room temperature. Power dependent measurements at $T=78K$ and $T=200K$, prove that at high excitation density, an additional peak at energies below the trion, dominates the photoluminescence. We attribute this peak to biexciton emission. The main results after photochemical doping is a systematic red shift of neutral exciton ($15meV$) in the case of Cl_2 . We have the same results in the case of NH_3 , but the shift here is negligible ($3meV$).

After this effort there are many future plans related to chemical doping in 2D materials. It would be interesting to extend our research by testing the behavior of the already tested monolayer WS_2 , but now in vacuum conditions, without any exposure to the atmosphere. This parametrical experiment can help us to control the number of pulses and examine their influence on the monolayer region. Another future plan is the control of doping efficiency (exposure time, fluence, partial pressure). A power and temperature dependence of different excitonic peaks are necessary to study before and after photochemical doping. Furthermore, after appropriate treatment of the samples, an electrical characterization must be done, so as to decide on the type (n- or p- type) of doping achieved in our samples. Finally, another attractive project would be to experiment with other 2D crystals to research their behavior before and after chemical doping to figure out if this technique is universal.

References

- [1] A. Mitoglu, “Probing the electronic properties of bulk and monolayer crystals of tungsten dichalcogenides using magneto-spectroscopy,” 2015.
- [2] K. S. Novoselov, D. Jiang, F. Schedin, T. J. Booth, V. V Khotkevich, S. V Morozov, and a K. Geim, “Two-dimensional atomic crystals.,” *Proc. Natl. Acad. Sci. U. S. A.*, vol. 102, no. 30, pp. 10451–10453, 2005.
- [3] K. F. Mak, C. Lee, J. Hone, J. Shan, and T. F. Heinz, “Atomically thin MoS₂: A new direct-gap semiconductor,” *Phys. Rev. Lett.*, vol. 105, no. 13, 2010.
- [4] X. Liu, “Nanomechanical Systems from 2D Materials by,” 2014.
- [5] L. Ma, “Synthesis and Characterization of Large Area Few-layer MoS₂ and WS₂ Films,” p. 106, 2014.
- [6] Q. H. Wang, K. Kalantar-Zadeh, A. Kis, J. N. Coleman, and M. S. Strano, “Electronics and optoelectronics of two-dimensional transition metal dichalcogenides,” *Nat. Nanotechnol.*, vol. 7, no. 11, pp. 699–712, 2012.
- [7] D. J. Late, C. S. Rout, D. Chakravarty, and S. Ratha, “Emerging Energy Applications of Two-Dimensional Layered Materials,” *Can. Chem. Trans.*, vol. 3, no. 2, pp. 118–157, 2015.
- [8] M. Chhowalla, H. S. Shin, G. Eda, L.-J. Li, K. P. Loh, and H. Zhang, “The chemistry of two-dimensional layered transition metal dichalcogenide nanosheets,” *Nat. Chem.*, vol. 5, no. 4, pp. 263–275, 2013.
- [9] a. Kumar and P. K. Ahluwalia, “Electronic structure of transition metal dichalcogenides monolayers 1H-MX₂ (M = Mo, W; X = S, Se, Te) from ab-initio theory: new direct band gap semiconductors,” *Eur. Phys. J. B*, vol. 85, no. 6, pp. 18–22, 2012.
- [10] H. Terrones, F. López-Urías, and M. Terrones, “Novel hetero-layered materials with tunable direct band gaps by sandwiching different metal disulfides and diselenides.,” *Sci. Rep.*, vol. 3, p. 1549, 2013.
- [11] G. Liu, D. Xiao, Y. Yao, X. X. De, W. Yao, and D. Xiao, “Electronic structures and theoretical modelling of two-dimensional group-VIB transition metal dichalcogenides,” *Chem. Soc. Rev.*, vol. 44, no. 9, pp. 2643–2663, 2014.
- [12] L. Code, “Photoluminescence in MoS₂ Multilayers with Functional Polyelectrolyte Nanospacing Department of Physics.”
- [13] Y. Lin, “Optical properties of two-dimensional transition metal dichalcogenides,” 2014.
- [14] C. Lee, H. Yan, L. E. Brus, T. F. Heinz, J. Hone, and S. Ryu, “Anomalous lattice vibrations of single- and few-layer MoS₂,” *ACS Nano*, vol. 4, no. 5, pp. 2695–2700, 2010.
- [15] a. Molina-Sánchez and L. Wirtz, “Phonons in single-layer and few-layer MoS₂ and WS₂,” *Phys. Rev. B*, vol. 84, no. 15, p. 155413, 2011.

- [16] H. R. Gutiérrez, N. Perea-lópez, A. L. Elías, A. Berkdemir, B. Wang, R. Lv, F. López-urías, V. H. Crespi, and H. Terrones, “Extraordinary room-temperature photoluminescence in WS₂ monolayers.”
- [17] W. Zhao, Z. Ghorannevis, L. Chu, M. Toh, C. Kloc, P. H. Tan, and G. Eda, “Evolution of electronic structure in atomically thin sheets of ws₂ and wse₂,” *ACS Nano*, vol. 7, no. 1, pp. 791–797, 2013.
- [18] X. Xu, “Spin and pseudospins in transition metal dichalcogenides,” *Proc. - 2014 Summer Top. Meet. Ser. SUM 2014*, vol. 10, no. May, pp. 1–2, 2014.
- [19] B. Zhu, H. Zeng, J. Dai, and X. Cui, “The Study of Spin-Valley Coupling in Atomically Thin Group VI Transition Metal Dichalcogenides,” *Adv. Mater.*, vol. 26, no. 31, pp. 5504–5507, 2014.
- [20] A. Chernikov, T. C. Berkelbach, H. M. Hill, A. Rigosi, Y. Li, O. B. Aslan, D. R. Reichman, M. S. Hybertsen, and T. F. Heinz, “Exciton Binding Energy and Nonhydrogenic Rydberg Series in Monolayer WS₂,” *Phys. Rev. Lett.*, vol. 113, no. 7, p. 076802, 2014.
- [21] a. R. Beal and W. Y. Liang, “Excitons in 2H-WS₂ and 3R-WS₂,” *J. Phys. C Solid State Phys.*, vol. 9, pp. 2459–2466, 1976.
- [22] A. a M. Jones, H. Yu, N. J. Ghimire, S. Wu, G. Aivazian, J. S. Ross, and B. Zhao, “Title : Optical Generation of Excitonic Valley Coherence in Monolayer WSe₂.”
- [23] T. C. Berkelbach, M. S. Hybertsen, and D. R. Reichman, “Theory of Neutral and Charged Excitons in Monolayer Transition Metal Dichalcogenides,” vol. 2, no. c, pp. 1–6, 2013.
- [24] F. Albrechtsen, “Reflection, refraction, diffraction, and scattering,” pp. 1–82, 2008.
- [25] “OPTICAL PROPERTIES OF DIRECT BANDGAP SEMICONDUCTORS :FROM BULK TO LOW,” 2015.
- [26] A. Lecture and J. C. Maxwell, “General Properties of Light.”
- [27] Δ. Μεταπτυχιακό, Π. Σπουδών, Ε. Και, and Τ. Πολυμερών, “« Μελέτη της αλληλεπίδρασης Γραφενίου / Πολυμερικού Υποστρώματος μέσω Φασματοσκοπίας Raman »,» 2013.
- [28] “ΜΗΧΑΝΙΚΗ ΚΑΙ ΦΑΣΜΟΤΟΣΚΟΠΙΚΗ ΜΕΛΕΤΗ ΕΝΙΣΧΥΤΙΚΩΝ ΜΕΣΩΝ ΜΕ ΒΑΣΗ ΤΟ ΓΡΑΦΕΝΙΟ ΚΑΙ ΠΡΟΤΥΠΩΝ ΠΟΛΥΜΕΡΙΚΩΝ ΣΥΝΘΕΤΩΝ ΥΛΙΚΩΝ,” 2013.
- [29] A. Berkdemir, H. R. Gutiérrez, A. R. Botello-Méndez, N. Perea-López, A. L. Elías, C.-I. Chia, B. Wang, V. H. Crespi, F. López-Urías, J.-C. Charlier, H. Terrones, and M. Terrones, “Identification of individual and few layers of WS₂ using Raman Spectroscopy,” *Sci. Rep.*, vol. 3, pp. 1–8, 2013.
- [30] X. Zhang, X.-F. Qiao, W. Shi, J.-B. Wu, D.-S. Jiang, and P.-H. Tan, “Phonon and Raman scattering of two-dimensional transition metal dichalcogenides from monolayer, multilayer to bulk material,” *Chem. Soc. Rev.*, vol. 44, no. 9, pp. 2757–2785, 2015.
- [31] A. P. Nayak, D. Voiry, J. Liu, S. Thomas, A. Sharma, C. Tan, C. Chen, L. Lee, M. Chhowalla, J. Lin, A. K. Singh, and D. Akinwande, “Pressure-Dependent Optical and Vibrational Properties of Monolayer Molybdenum Disulfide,” 2014.

- [32] K. Kaasbjerg, K. S. Thygesen, and K. W. Jacobsen, "First-principles study of the phonon-limited mobility in n-type single-layer MoS₂," 2012.
- [33] N. R. Bandaru, "Structure and Optical properties of Transition Metal Dichalcogenides (TMDs) – MX₂ (M = Mo , W & X = S , Se) under High Pressure and High Temperature conditions," vol. 2, no. August, 2015.
- [34] M. Currie, a. T. Hanbicki, G. Kioseoglou, and B. T. Jonker, "Optical control of charged exciton states in tungsten disulfide," *Appl. Phys. Lett.*, vol. 106, no. May, p. 201907, 2015.
- [35] a. T. Hanbicki, M. Currie, G. Kioseoglou, a. L. Friedman, and B. T. Jonker, "Measurement of high exciton binding energy in the monolayer transition-metal dichalcogenides WS₂ and WSe₂," *Solid State Commun.*, vol. 203, pp. 16–20, 2015.
- [36] A. Thin, "Evolution of Electronic Structure in," no. Xx, 2012.
- [37] M. Staiger, R. Gillen, N. Scheuschner, O. Ochedowski, M. Schleberger, C. Thomsen, and J. Maultzsch, "Splitting of the monolayer out-of-plane A₁ Raman mode in few-layer WS₂," pp. 1–9, 2015.
- [38] M. S. Dresselhaus, "SOLID STATE PHYSICS PART II Optical Properties of Solids," p. 253, 2001.
- [39] A. Li, "Interaction of Nanoparticles with Radiation - A. Li," vol. 309, no. 1935, 2004.
- [40] Z. Ye, T. Cao, K. O'Brien, H. Zhu, X. Yin, Y. Wang, S. G. Louie, and X. Zhang, "Probing Excitonic Dark States in Single-layer Tungsten Disulfide," *arXiv Prepr. arXiv ...*, vol. 513, no. 7517, pp. 214–218, 2014.
- [41] H. Zeng, G.-B. Liu, J. Dai, Y. Yan, B. Zhu, R. He, L. Xie, S. Xu, X. Chen, W. Yao, and X. Cui, "Optical signature of symmetry variations and spin-valley coupling in atomically thin tungsten dichalcogenides," *Sci. Rep.*, vol. 3, p. 1608, 2013.
- [42] A. Ramasubramaniam, "Large Excitonic Effects in Molybdenum and Tungsten Dichalcogenide Monolayers," pp. 1–15, 2012.
- [43] M. S. Dresselhaus, "Solid State Physics Part II: Optical Properties of Solids," *Proceedings Int. Sch. Phys.*, p. 198, 1966.
- [44] a. a. Mitoglu, P. Plochocka, J. N. Jadczyk, W. Escoffier, G. L. J. a. Rikken, L. Kulyuk, and D. K. Maude, "Optical manipulation of the exciton charge state in single-layer tungsten disulfide," *Phys. Rev. B*, vol. 88, no. 24, pp. 1–5, 2013.
- [45] K. P. O'Donnell and X. Chen, "Temperature dependence of semiconductor band gaps," *Appl. Phys. Lett.*, vol. 58, no. 25, pp. 2924–2926, 1991.
- [46] G. Plechinger, P. Nagler, J. Kraus, N. Paradiso, C. Strunk, C. Schüller, and T. Korn, "Identification of excitons, trions and biexcitons in single-layer WS₂," *ArXiv*, vol. 1, no. X, pp. 1–6, 2015.
- [47] J. S. Ross, S. Wu, H. Yu, N. J. Ghimire, A. M. Jones, G. Aivazian, J. Yan, D. G. Mandrus, D. Xiao, W. Yao, and X. Xu, "Electrical control of neutral and charged excitons in a monolayer semiconductor," *Nat. Commun.*, vol. 4, p. 1474, 2013.

- [48] J. S. Ross, S. Wu, H. Yu, N. J. Ghimire, A. M. Jones, G. Aivazian, J. Yan, D. G. Mandrus, D. Xiao, W. Yao, and X. Xu, “Electrical Control of Neutral and Charged Excitons in a Monolayer Semiconductor,” pp. 1–23.
- [49] X. H. Wang, J. Q. Ning, C. C. Zheng, B. R. Zhu, L. Xie, H. S. Wu, and S. J. Xu, “Photoluminescence and Raman mapping characterization of WS₂ monolayers prepared using top-down and bottom-up methods,” *J. Mater. Chem. C*, vol. 3, no. 11, pp. 2589–2592, 2015.
- [50] Y. You, X.-X. Zhang, T. C. Berkelbach, M. S. Hybertsen, D. R. Reichman, and T. F. Heinz, “Observation of biexcitons in monolayer WSe₂,” *Nat. Phys.*, vol. 11, no. 6, pp. 477–481, 2015.
- [51] H. P. Komsa, J. Kotakoski, S. Kurasch, O. Lehtinen, U. Kaiser, and A. V. Krasheninnikov, “Two-dimensional transition metal dichalcogenides under electron irradiation: Defect production and doping,” *Phys. Rev. Lett.*, vol. 109, no. 3, pp. 1–5, 2012.
- [52] N. Peimyoo, W. Yang, J. Shang, X. Shen, Y. Wang, and T. Yu, “Chemically Driven Tunable Light Emission of Charged and Neutral excitons in monolayer WS₂,” *ACS Nano*, vol. 8, no. 11, pp. 11320–11329, 2014.
- [53] B. Soediono, “<https://graphene-supermarket.com/>,” *J. Chem. Inf. Model.*, vol. 53, p. 160, 1989.
- [54] a T. Hanbicki, G. Kioseoglou, M. Currie, C. S. Hellberg, K. M. Mccreary, a L. Friedman, and B. T. Jonker, “Anomalous temperature-dependent spin-valley polarization in monolayer WS₂,” *Nat. Publ. Gr.*, no. October 2015, pp. 1–9, 2016.
- [55] X. Li and H. Zhu, “Two-dimensional MoS₂: Properties, preparation, and applications,” *J. Mater.*, vol. 1, no. 1, pp. 33–44, 2015.
- [56] R. F. Peters and R. F. Peters, “University of Alberta Fabrication and testing of surface-enhanced Raman spectroscopy substrates for the detection of biomolecules by Master of Science Department of Electrical and Computer Engineering To: Erica Thank you for all your love , encouragement,” 2014.
- [57] I. M. Paradisanos, “University of Crete Department of Physics Master thesis Intense femtosecond photoexcitation of bulk and,” no. September, 2014.
- [58] C. D. Weber, C. Bradley, and M. C. Lonergan, “Solution phase n-doping of C₆₀ and PCBM using tetrabutylammonium fluoride,” *J. Mater. Chem.*, vol. 2, no. 2, p. 303, 2014.
- [59] K. P. Dhakal, D. L. Duong, J. Lee, H. Nam, M. Kim, M. Kan, Y. H. Lee, and J. Kim, “Confocal absorption spectral imaging of MoS₂: optical transitions depending on the atomic thickness of intrinsic and chemically doped MoS₂,” *Nanoscale*, vol. 6, no. 21, pp. 13028–35, 2014.
- [60] I. a. Buyanova, W. M. Chen, G. Pozina, J. P. Bergman, B. Monemar, H. P. Xin, and C. W. Tu, “Mechanism for low-temperature photoluminescence in GaNAs/GaAs structures grown by molecular-beam epitaxy,” *Appl. Phys. Lett.*, vol. 75, no. 4, p. 501, 1999.